STUDY OF THE EFFECTS OF SURFACE MORPHOLOGY AND DROPLET GROWTH DYNAMICS ON CONDENSATION HEAT TRANSFER

A Dissertation

by

CHUN-WEI YAO

Submitted to the Office of Graduate and Professional Studies of
Texas A&M University
in partial fulfillment of the requirements for the degree of

DOCTOR OF PHILOSOPHY

Chair of Committee,	Jorge Alvarado
Committee Members,	Sai Chuen Lau
	Yassin A. Hassan
	Karen Vierow
Head of Department,	Andreas A. Polycarpou

May 2014

Major Subject: Mechanical Engineering

ABSTRACT

Condensation heat transfer has recently received a lot of renewed attention due to the development and use of surfaces with micro- and nano-scale features. Most of the new surfaces tend to promote dropwise condensation, which leads to higher rates of heat transfer when compared with filmwise condensation. In the current study, the effects of surface morphology and surface chemistry on the condensation mechanisms have been investigated using engineered surfaces. Firstly, hybrid surfaces consisting of an array of micropillars with hydrophobic and hydrophilic sites have been designed to exhibit a distinct Cassie-Baxter wetting behavior at different temperatures. Characterization experiments have revealed that hybrid surfaces depict a unique wetting behavior. Furthermore, more types of engineered surfaces were fabricated including nanoparticle-based hydrophobic surface, polytetrafluoroethylene (PTFE) surface, and self-assembled monolayers (SAMs) surface. Experiments have been conducted to determine the heat transfer performance of all engineered surfaces under a constant humidity level, surface-to-ambient temperature difference, and laminar flow conditions. Experimental results reveal that droplet sliding can have an important effect on heat transfer performance. Also, empirical heat transfer correlations have been postulated and fitted using experimental data using condensing and air temperature difference and Reynolds number as independent variables. Results indicate that the postulated correlations are in excellent agreement with experimental data. In addition, surface temperature data obtained using an advanced IR imaging system have been analyzed to determine the effects of the surface features on droplet growth dynamics. The non-invasive IR

measurement technique has been helpful in understanding the droplet growth dynamics such as droplet coalescence. Results to date show that the static contact angles and sliding angles have marked effects on droplet growth and coalescence on the surfaces in the early stages of condensation. Furthermore, results also reveal that droplet sliding angles can have an important effect on droplet sliding motion and condensed droplet dynamics play an important role during the overall condensation process. In summary, the effect of surface morphology and droplet growth dynamics on heat transfer during condensation were investigated and elucidated.

ACKNOWLEDGEMENTS

I would like express sincere gratitude to my advisor, Dr. Jorge Alvarado, for his unwavering support of me over the years. I am particularly grateful for the considerable freedom he provided me in my research as well as his guidance. I also extend my heartfelt appreciation to my committee members, Dr. Sai Chuen Lau, Dr. Karen Vierow, and Dr.Yassin A. Hassan, for serving on my committee and their guidance throughout this research.

I want to express my gratitude to Dr. Charles P. Marsh for his support and participating in the study. I also want to thank the Engineer Research Development Center (ERDC) in Champaign for their support and providing the instrument.

Thanks also go to the talented members of Prof. Alvarado's group. Especially thanks to T.L. Zhang, C.-H. Hsu C.-L. Lai and Albert Fan for having a good time with me in the lab.

I am thankful to my best friend C.Y. Chen for the laughter, smile, and, encouragement over these years. This friendship has been one of the best parts of my life.

Finally, I would like to dedicate this work to my wonderful family: my brother C.-H. Yao, my parents C.-S. Yau and L.-C. Chien. I love them so much. Thanks for their love and support throughout this tough journey.

NOMENCLATURE

A	heat transfer area
a	micropillar width
b	gap size
f_1	area fraction of the solid-liquid interface
f_2	area fraction of the liquid-air interface
h	heat transfer coefficient
h	micropillar height
k	thermal conductivity
k_l	water thermal conductivity
k_{coat}	hydrophobic coating conductivity
$\dot{m}_{cond}$	condensate mass flow
$\dot{m}$	mass flow
P	atmospheric pressure
P_{VE}	water vapor partial pressure of humid air
P_{VW}	water vapor partial pressure of the plate surface
q”	heat flux
Re_x	Reynolds number based on X
R_f	roughness factor
R’	specific gas constant
R	drop radius
r	drop radius
r_{min}	critical radius
ΔT_t	surface subcooling
ΔT	temperature drop
T_{sat}	saturation temperature

$T_{cond,exit}$	condensate temperature,
T_{st}	temperature of the steam,
T_s	sample surface temperature.
T_{surf}	surface temperature
T_{vap}	condensing vapor temperature
T_d	dew point temperature
T_{amb}	ambient temperature
V	droplet volume
x	the area fraction
Δy	thickness
σ	surface tension
$\widehat{\sigma}$	specific heat ratio
ρ	liquid density
ρ_v	vapor density
ρ_w	liquid water density
h_{lv}	heat of vaporization
h_{fg}	latent heat of vaporization
h_i	interfacial heat transfer coefficient
γ_{SV1}	surface tension at the solid-vapor interfaces for hydrophilic surfaces
γ_{SV2}	surface tension at the solid-vapor interfaces for hydrophobic surfaces
γ_{LV}	surface tension at the liquid-vapor interface
δ_{coat}	hydrophobic coating thickness
θ	contact angle
θ_{CB}	apparent Cassie-Baxter contact angle

θ_0	intrinsic contact angle of material
θ_w	apparent Wenzel contact angle
θ_1	contact angle of the liquid droplet on a flat hydrophilic surface
θ_2	contact angle of a liquid droplet on a flat hydrophobic surface
θ_h	contact angle on the hybrid surface
ϕ_T	non-dimensional temperature difference
ϕ	relative humidity

TABLE OF CONTENTS

Page

LIST OF FIGURES

Page

LIST OF TABLES

Page

CHAPTER I

INTRODUCTION

The use of engineered surfaces in condensation has received renewed attention due to the development and use of micro- and nanoscale features on heat transfer surfaces. Recently, researchers around the world have been looking at ways to improve dropwise condensation since it has been proven to be the most effective mode of heat transfer during vapor-liquid phase change. Dropwise condensation was discovered in 1930 by Schmidt et al. [1] and has attracted significant attention due to its higher heat transfer rate by an order of magnitude when compared to filmwise condensation [2, 3]. This phase change phenomenon is used in a number of systems, including power generation, water desalination, bioreactors, and heat pipes. Moreover, as micro or nano scale electronic devices such as CPU chips grow more complex, thermal management in micro systems that involve condensation must be able to cope with stringent heat transfer demands. Therefore, a new efficient condensation cooling technology is in great demand. Since micro condensers are required in cooling systems such as micro heat pipes, surface-enhanced dropwise condensation has the potential to increase the dissipation of high heat flux from electronic components due to its high heat transfer ability.

1.1. Motivation

It has been reported that dropwise condensation exhibits higher heat transfer by an order of magnitude when compared to filmwise condensation [2, 3]. In order to understand the phenomenon associated with dropwise condensation, most recent

researchers have attempted to design and use hydrophobic or super hydrophobic surfaces with nano/micro scale features [4-14]. However, there are relatively few investigations that have been able to explain the effect on dropwise condensation heat transfer on micro- and nanoscale engineered surfaces. Furthermore, few studies have been able to elucidate the different condensation mechanisms which included droplet growth, droplet coalescence, as well as droplet shedding. Therefore, a good understanding of the key condensation mechanisms when using novel condensing surfaces is needed. Moreover, the effects of surface morphology, surface wetting behavior, and droplet growth dynamics on engineered surfaces that exhibit dropwise condensation need to be understand to develop the next generation of micro scale condensers.

1.2. Objective

The purpose of this study was to determine and characterize the growth dynamics of and heat transfer behavior of condensate droplets responsible for enhanced heat and mass transfer on engineered surfaces during condensation. To satisfy this objective, engineered surfaces, such as hybrid surfaces, were designed, fabricated, and characterized using a variety of newly developed coating schemes. In addition, a surface-energy-based model has been developed to predict the wettability of droplets on hybrid surfaces. A high resolution digital microscopy system was employed to observe condensation processes at right scale. Finally, a thermal data collection system consisting of thermocouples and an infrared camera system were employed to acquire condensation surface temperature data. This work has revealed details about growth, coalescence, and shedding mechanisms of droplets on engineered surfaces during

condensation. Generally, this study should increase the overall understanding of the dropwise condensation on engineered surfaces and serve as a basis for future studies. It is also hoped that this research will eventually contribute to the design and use of more effective engineered condensing surface, which could be lead to enhanced dropwise condensation strategies.

1.3. Overview

This dissertation is divided into seven chapters. Chapter II presents an overview of surface wettability and condensation literature. Chapter III describes the apparatus and operating conditions for the experimental portion of the research work. Chapter IV describes the design parameters and fabrication process of engineered surfaces. Chapter V outlines and presents wettability of engineered surfaces and results of condensation dynamics. Chapter VI presents the results and discussion of the heat transfer experiments. Chapter VII presents conclusions and recommendations for future work.

CHAPTER II

LITERATURE REVIEW

The study of dropwise condensation has been investigated from the early 1900's and models and experimental data have been generated. However, most of the studies in this area have focused on characterizing the overall condensation heat transfer of pure vapor. In addition, dropwise condensation happens on those surfaces in the early condensation stages only before transitioning to a filmwise condensation mode. As micro/ nanotechnology has developed recently, a condensing surface can be fabricated using strong hydrophobic coating to promote dropwise condensation. However, there are still few studies focused on condensation heat transfer of air-steam mixtures. Moreover, most of the studies have not been concerned with the effect of droplet condensation dynamics on heat transfer. In this chapter, a review of the studies related to engineered surfaces and dropwise condensation is presented.

2.1. Literature Review of the Engineered Surface Design and Wettability

2.1.1. Engineered Hydrophobic Surfaces

In the past few years, engineered hydrophobic surfaces have been designed and characterized to promote dropwise condensation by making use of nano/micro scale features [4-11, 13-15]. In general, artificial hydrophobic surfaces require a suitable type of morphology or roughness [16, 17] exhibiting low surface free energy when the right materials are used [18, 19]. Such surfaces interact with liquids in a way that results in high contact angles and low contact angle hysteresis, which sheds liquids such as water

easily [20, 21]. These characteristics are highly desirable in condensation heat transfer. Nature has developed objects such as plants, aquatic insects, and animals with hydrophobic properties. Figure 1 shows natural examples with a variety of surface structures imaged using scanning electron microscope. *Nelumbo nucifera* (Lotus) has attracted many researches due to its hierarchical roughness (Figure 1a) starting in the 1990s. The leaf exhibits hydrophobic properties and a self-cleaning function [22]. There are many micro scale papillose epidermal cells as shown in Figure 1a. Also, it can be observed that nanoscale structures grow on the top of the papilloses. The leaf shows high static contact angle with water droplets about 164° [23]. Termites have specialized hydrophobic structures on their wings as shown in Figure 1b. The star shaped structures and long hairs with fine structured troughs aid the ability of the wings to resist water penetration. Water striders have many thousands of hairs (setae) on each leg as shown in Figure 1c. These hairs are around 50 μm in length and tilt 20° from the surface of a leg. Many nanoscale grooves are on each microhairs, and form unique super hydrophobic hierarchical structures. The wings of cicada have a well-aligned nanostructure array (Figure 1d), which makes them superhydrophobic. Figure 1e shows hexagonally nanonipples cover a mosquito eye and maintain the eye dry. The structure of the pigeon feather provides feathers' water repellency (Figure 1e). These examples suggest that most natural superhydrophobic surfaces have roughness at micro scale or nanoscale level. It is possible to mimic these natural surfaces by creating nano or micro scale structure patterns with hydrophobic material.

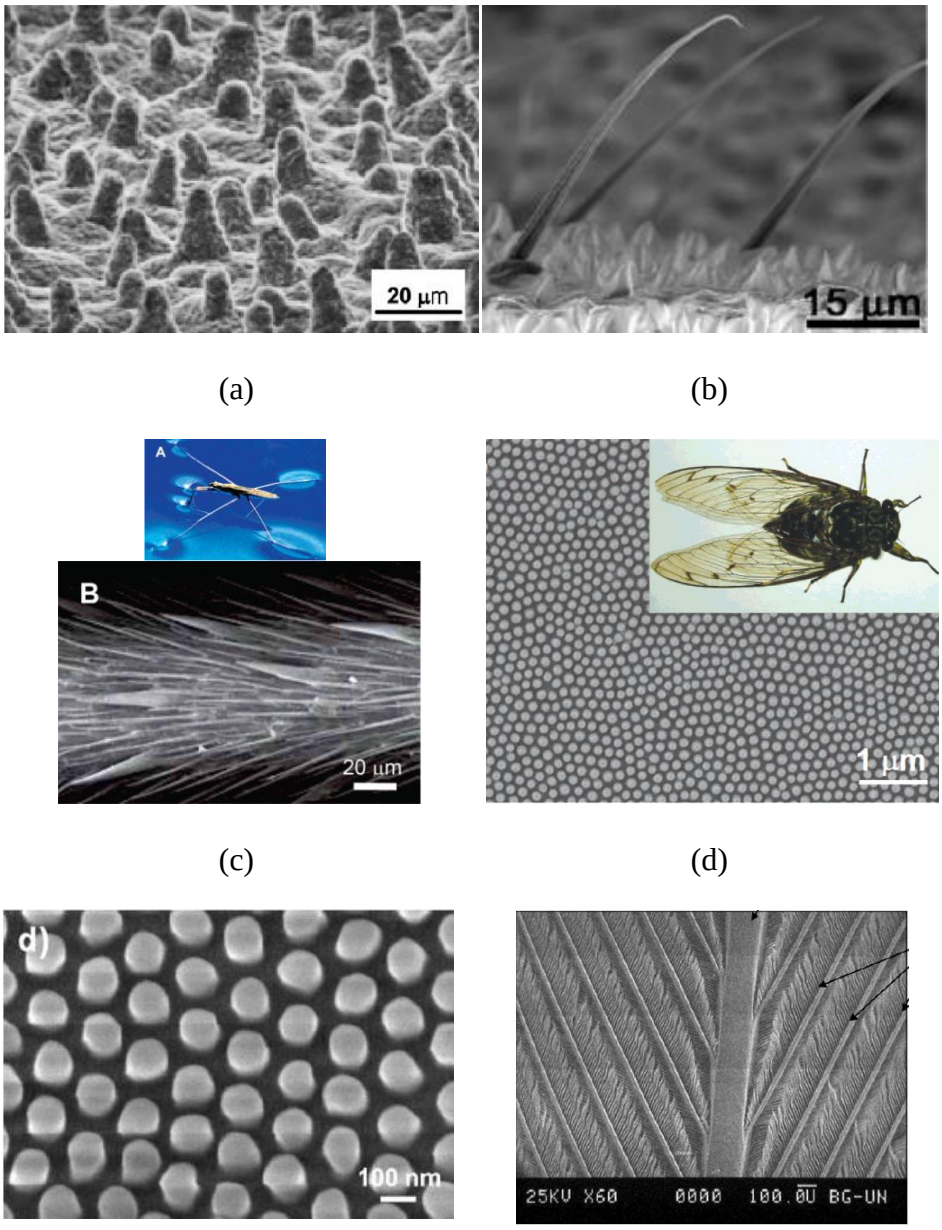

Figure 1. Scanning electron micrographs of natural and biomimetic superhydrophobic surfaces. (a) *Nelumbo nucifera* (Lotus) leaf [24] (b) termite wing membrane [25] (c) water strider leg microstructure, scale bars 20 μm [26] (upper) water strider [27] (d) artificial nanostructure surfaces which is similar with the wings of cicada (inset) [28] (e) nanostructure surface on mosquito eye [29] (f) multi-scale structures on pigeon feather [30]

In the past few years, surfaces that promote dropwise condensation have been designed and made, because in general they lead to higher heat transfer coefficients [31-33]. Most recent studies about dropwise condensation have focused on superhydrophobic surfaces with micro scale features. In those cases, it has been found that condensate droplets may partially penetrate the texture of the surfaces [4, 13, 15]. Under those conditions, droplets do not fully exhibit a hydrophobic behavior and could inhibit proper droplet shedding behavior needed for enhanced dropwise condensation. Condensate droplets under those conditions tend to grow to a large size (~2 mm) until they roll off the surface via gravity [34, 35].

Droplet size should also be reduced while increasing the droplet departure rate so that more surfaces are available for droplet renucleation. This should enable greater heat transfer per contact area [36]. Recent studies have focused on nanostructured surfaces from which suspended condensate droplets can spontaneously eject or jump when they reach a relative small diameter size (less than 100 μm) [6, 7, 11, 14].

A hybrid surface consisting of hydrophobic and hydrophilic sites was reported to be to be the most efficient for water condensation [37]. The surface was inspired by the Stenocara beetle's back which was covered with an array of bumps. The peaks of these bumps are hydrophilic, and reaming parts of these bumps are hydrophobic [38]. Therefore, condensate droplets are captured by hydrophilic peaks and efficiently collected along the hydrophobic path.

2.1.2. **Contact Angle Modeling of Wetted Engineered Surfaces**

The hydrophobicity of surfaces can be adjusted by manipulating the surface energy and roughness. Surface free energy of the surface system determines whether droplets are able to fully wet the surface or sit on top of a composite interface which includes solid structures and air. The hydrophobicity of a surface can be described by finding its "contact angle," which describes the shape of a droplet as it sits on a surface. The contact angle is also the direct result of surface free energy minimization of the interfacial system. It has been suggested by using the Cassie-Baxter model [39] and Wenzel model [40] that we could know how nano/micro-roughness and hydrophobic material aid in the ability of homogeneous surfaces to resist water penetration. The Cassie-Baxter model describes the wetting behavior of surfaces through the following equation:

$$\cos\theta_{CB} = f_1 \cos\theta_0 - f_2 \tag{1}$$

where θ_{CB} is the apparent Cassie-Baxter contact angle, θ_0 is the intrinsic contact angle of material, f_1 is the area fraction of the solid-liquid interface,.

For a water droplet on a rough surface, the Wenzel model describes the wetting behavior of surfaces as follows:

$$\cos\theta_w = R_f \cos\theta_0 \tag{2}$$

where θ_w is the apparent Wenzel contact angle, θ_0 is the intrinsic contact angle of material, and a roughness factor R_f described as the actual amount of surface area over the superficial or "geometric" surface.

Recently, Patankar [41] proposed a methodology to determine the transition from Cassie contact angle to Wenzel contact angle based on energy balance. He revealed that a droplet may not always exist in the lower energy state. Depending on how the droplet is formed, droplets can exist in multiple equilibrium states on rough surface. Tuteja et al. [42] developed two robustness parameters for micro structured surfaces. Based on the parameters, superhydrophobic textured surfaces could be designed and fabricated with desired high contact angles. Jeong et al. [43] developed a thermodynamic model to estimate static contact angle, contact angle hysteresis, and wetting transition on micro and nanoscale combined hierarchical surfaces. Kwon et al. [44] derived the criteria to show when the Wenzel state is unfavorable on hierarchical surfaces. Therefore, a Cassie-type surface that offers extreme hydrophobicity and a small contact angle hysteresis could be fabricated by creating a roughness hierarchy with a small scale roughness features on a larger scale one. Liu et al. [45] calculated the interface free energy of a local condensate droplet and derived equations for hierarchical surfaces. The results showed that a condensed droplet on a micro-nano hierarchical roughness surface can spontaneously be in a Cassie state.

2.2. Literature Review of the Dropwise Condensation Heat Transfer on Engineered Surfaces

Dropwise condensation is a complex heat transfer phenomenon that has attracted significant attention due to its superior heat transfer rate [1]. Unlike filmwise condensation where the liquid film covers the entire surface, dropwise condensation can be described as dynamic processes including droplet formation, droplet growth, and departure of droplet. In order to understand the phenomenon associated with this special condensation form, numerous researchers have attempted to do condensation experiments with modified surfaces to establish mathematical models. In the past, experimental studies have reported that very large heat transfer coefficients could be obtained from modified metallic surfaces [46-48]. Also, one of the earliest dropwise condensation models was proposed by Rose [49] who combined the theoretical result for the heat transfer through an individual droplet using drop size distribution for calculation purposes.

Since filmwise condensation occurs on metal surfaces, researchers have focused their attention on ion implantation to promote dropwise condensation [31, 32, 46, 50]. Rausch et al. [32] studied heat transfer phenomena on a Titanium surface that was modified with N^+ ions. The study showed an increase of heat flux by a factor of up to 5.5 with an ion implanted Titanium surface. It has been suggested that the ion implantation dose not significantly affect condensation heat transfer if dropwise condensation is observed. In that particular study, the mean heat transfer coefficient was determined by Equation (3).

$$h_c = \frac{\dot{m}_{cond}[\Delta h + \bar{c}_{p,cond}(T_{st} - T_{cond,exit})]}{A(T_{st} - T_s)} \quad (3)$$

where $\dot{m}_{cond}$ represents the condensate mass flow, A represents the heat transfer area, $\bar{c}_{p,cond}$ represents the specific heat capacity of condensate, $T_{cond,exit}$ represents the condensate temperature, T_{st} represents the temperature of the steam, and T_s represents the sample surface temperature.

Daniel et al. [51] was the first group to investigate the interaction between the random movements of droplets and over all condensation heat transfer. In their study, condensation experimental studies were conducted in a steam chamber. They recognized the potential of heat transfer enhancement by applying surface tension gradients to promote and induce a droplet removal mechanism. They concluded that their gradient surface exhibited a higher heat transfer coefficient than a hydrophobic silane based surface.

More recently, environmental scanning electron microscopy (ESEM) was used to study smaller droplets during condensation. The ESEM can be used to examine and record images of condensate droplets on the nano/micro scale patterned surfaces. C. Dietz et al. [10] performed an investigation trying to relate heat transfer phenomena to the distribution of condensate droplet sizes with a range of 0-120 μm. Equation (4) from Rose [3] was used to estimate the heat transfer rate. The results suggest that

superhydrophobic surfaces lead to an increase in the heat transfer coefficient by a factor of 2 during dropwise condensation.

$$q = \frac{1}{3\hat{r}^{1/3}} \int_{r_{\min}}^{r_{\max}} \frac{(\Delta T_t - 2\sigma T_{sat}/r\rho h_{lv})}{\left(\frac{K_1 r}{k} + \frac{K_2 T_{sat}}{\rho_v h_{lv}^2} \left(\frac{\hat{\sigma}+1}{\hat{\sigma}-1} \right) \sqrt{\frac{R' T_{sat}}{2\pi}} \right)} r^{n-1} dr \tag{4}$$

where ΔT_t, T_{sat}, σ, ρ, ρ_v, h_{lv}, k, $\hat{\sigma}$, R', and r are the surface subcooling, saturation temperature, surface tension, liquid density, vapor density, heat of vaporization, liquid thermal conductivity, specific heat ratio, specific gas constant, and drop radius respectively. The equation parameters K_1, K_2, and n are set at 0.667, 0.5, and 0.333 respectively.

Miljkovic et al. [14] studied the effect of droplet state, heat, and mass transfer on superhydrophobic nanostructured surfaces by conducting condensation in ESEM. The study reported that nanostructured surfaces had a 56% higher heat flux for partially wetting droplet morphologies than flat hydrophobic surfaces. Condensation dynamics such as droplet growth rate, coalescence length, and droplet wetting morphology were identified. Heat transfer rate was found to be a function of droplet growth rate and contact angle as indicated in Equation (5)

$$q = \dot{m} h_{fg} = \rho_w h_{fg} \frac{dV}{dt} = \frac{\pi}{3} \rho_w h_{fg} \frac{d}{dt} \left\{ (1-\cos\theta)^2 (2+\cos\theta) R^3 \right\} \tag{5}$$

Rykaczewski [52] studied the microdroplet growth mechanism on superhydrophic surfaces. They observed the microscopic stepwise motion during the growth of droplets. A constant base area mode was developed to estimate droplet growth. Based on ESEM observations and Equation (6), they presented the ratio of heat transfer rate through a droplet as a function of the radius r and contact angle θ.

$$q(r,\theta) = \frac{\Delta T \pi r^2 (1 - \frac{r_{\min}}{r})}{\left(\frac{1}{2h_i(1-\cos\theta)} + \frac{r\theta}{4k_i \sin\theta} + \frac{\delta_{coat}}{k_{coat}\sin^2\theta} \right)} \tag{6}$$

Cheng et al. [53] performed condensation experimental studies using a two-tier superhydrophobic surface in an ESEM and in a steam vapor chamber. They observed continuous dropwise condensation in an ESEM. However, filmwise condensation was observed on their superhydrophobic surface in the steam vapor chamber. They measured heat transfer coefficient by using Equation (7):

$$h = q/(T_{vap} - T_{surf}) \tag{7}$$

where q is the heat flux through the device surface and was determined by a series of thermocouples which were integrated into the cold base under the superhydrophobic surface. T_{surf} is the surface temperature of the device, and T_{vap} is the condensing vapor temperature. The results showed that the heat transfer coefficient on the super

hydrophobic surface was 1.5 kW/m^{2}k which was worse than the coefficient of a smooth hydrophobic surface and a bare silicon surface.

2.3. Literature Review of Condensed Droplet Dynamics on Engineered Surfaces

It is known that droplet dynamics associated with the dropwise condensation include nucleation, coalescence, sliding or roll off, and re-nucleation, resulting in heat transfer enhancement [54]. At the first stage, droplets grow by direct transfer and accommodation of water molecules onto the cool surface. Once each droplets reaches a certain size, coalescence becomes the primary mechanism of droplet growth due to the presence of neighboring droplets. At a later stage, when the droplet size is larger enough, gravity comes into play counteracting the effects of surface tension, which leads to the sliding motion of droplets. As a result, portions of the surface get exposed to moist air where re-nucleation takes place [55].

The various dynamics of condensed droplets on engineered surfaces have been studied by several researchers. Daniel et al. [51] revealed fast droplet movements when a gradient surface was used. The surface had a radially outward gradient of hydrophobicity. The central part of the surface was characterized by highly hydrophobic coating. They showed that the random movement of condensed droplets were biased toward the more hydrophilic part of the surface. The speeds of the moving condensed droplets were hundreds of times faster than the speeds of Marangoni flows.

Narhe and Beysens [56] studied the growth dynamics of condensed droplets on a superhydrophobic grooved patterned surface. They identified four stages of growth including initial stage, intermediate stage, drying stage, and large drop formation stage

on the surface. They first revealed that droplet growth rate was proportional to time. They also showed that the coalescence accelerated droplet growth greatly. Furthermore, they conducted similar studies for a super- hydrophobic spike surface [15] and a hydrophobic surface consisting micro pillars [5].

Chen et al. [6] reported continuous dropwise condensation on a two-tier structured surface. Their superhydrophobic surface consisted of micropillars, and carbon nanotubes were used to provide nano scale roughness on the micropillars. It was first demonstrated that droplets spontaneously jumped from the surface during condensation. This self-propelled phenomena were attributed to the surface energy released upon droplet coalescence [7]. Droplet removal by this jumping motion is highly desirable, and the detailed mechanisms are still being investigated. Feng et al [57] observed the coalescence-induced motion of condensate droplets on superhydrophobic copper surfaces. X. Chen et al. [11] reported more efficient eject motion via nanograssed micropyramidal architectures.

Rykaczewski et al. [58] described a novel droplet coalescence mechanism during dropwise condensation. They revealed that nano to micro scale satellite droplets could rapidly form from the same site and coalesced with a high contact angle droplets during condensation. This work described the benefits of the continuous self-propelled dropwise condensation on a nanostructured superhydrophobic surface.

2.4. Literature Review of the Dropwise Condensation Heat Transfer from Air-steam Mixtures

Condensation of a vapor with non-condensable gas often appears in industry. For example, in cooling systems of power plants, in air conditioning systems, bioreactors, and desalination systems [59-62]. The effects of non-condensable gas on the condensation of saturated steam have been studied by numerous investigators [63-66]. It is well known that small concentrations of non-condensable gas significantly hinders the heat transfer process, and the condensation heat transfer coefficients for vapor with non-condensable gas are much lower than pure vapor. This reduction could be attributed to small non-condensable gases tend to accumulate near the gas-liquid interface and create a thermal resistance. In contrast, the behavior of dropwise condensation of air-steam mixtures is much different to cases where the vapor quality is high. The non-condensable gases are dominant in the volume of air-steam mixtures. Therefore, non-condensable gases block vapor contact with the condensation surface and significantly reduce the condensation heat transfer coefficient. To date, a mechanistic understanding of condensation from humid air under atmospheric is still insufficient and necessary to develop effective condensation surfaces.

Lebedev et al. [67] conducted experiments of condensation of vapor from humid air on a flat plate. They found that the condensation heat transfer increases with air velocity and relative humidity.

Yaghoubi et al. [68] proposed a Nusselt number correlation for heat and mass transfer for laminar flow of humid air over a cooled plate with relative humilities over 50% as follows:

$$Nu = 0.902(\mathrm{Re}_x)^{0.5}(\frac{P_{VE}}{P})^{-0.337}(\frac{P_{VE} - P_{VW}}{P})^{0.524}(\phi)^{0.177} \quad (8)$$

The correlation showed an increase in Nusselt number with increasing relative humidity.

Nagai et al. [69] studied heat transfer characteristics for different orientations of condensation surface in humid air. A linear relationship between heat transfer rate and ambient-surface temperature difference was obtained. Also a constant heat transfer coefficient for relative humidity values between 40 to 90% was reported.

Che et al. [70] introduced the Colburn-Hougen method to evaluate the heat and mass transfer processes with high moisture gases. They proposed the Nusselt number correlation as follows:

$$Nu = 0.1823(\mathrm{Re})^{0.7707}(P_r)^{1/3}(Ch)^{0.2615} \quad (9)$$

where $Ch = (\frac{T_{sat} - T_w}{T_g - T_w})$, T_{sat} is the saturation temperature, T_w is the wall temperature, T_g is the gas temperature. The Prandtl number was assumed to be constant. The convection-condensation heat transfer process was found to be up to 2 times higher than that of forced convection without condensation.

Garrod et al. [37] performed condensation experimental studies via dewing. The effects of wettability of the condensation substrate on condensation efficiency were

quantified. The hydrophilic-hydrophobic patterned surface performed best comparing to hydrophilic surfaces and superhydrophobic surfaces during water collection from condensation.

Liang et al. [71] studied the effects of water vapor condensation on forced convection heat transfer. They showed that the combined convection–condensation heat transfer coefficient increases with Reynolds number. They also concluded that the condensation of vapor enhances the overall heat transfer.

Nabovati et al. [72] investigated condensation on an inclined cylinder in natural convection with controlled ambient relative humidity and temperature differences between ambient air and cold surface. They showed that increasing cylinder inclination decreases the heat flux and condensation rates. They also concluded that condensation rate increases with increasing relative humidity or decreasing surface temperature.

Thomas et al. [73] performed condensation experimental studies with a vertical copper surface and developed a correlation to relate heat transfer coefficient, relative humidity, and temperature differences between ambient air and surfaces. They observed that the heat transfer coefficient is higher for filmwise condensation than for dropwise condensation. The correlation of heat transfer coefficient was proposed as follows:

$$h = 110.96 + 203.11(RH)^{2.17}(\Delta T)^{0.1} \tag{10}$$

where h is heat transfer coefficient, RH is the relative humidity, ΔT is the temperature difference between ambient and surface.

Götze et al. [74] investigated dropwise condensation heat transfer in a humid air environment. Heat transfer measurements were conducted using the vertical surface, which contained a polymer layer with 20% of carbon nanotubes. They showed that a linear increase in heat transfer with increasing relative humidity and increasing Re number led to an increase of heat transfer at large humidity.

2.5. Conclusions and Knowledge Base Gaps

A number of conclusions can be drawn from the literature review:

1. Hydrophobic surfaces have been made to exhibit with high contact angles and low contact angle hysteresis in order to shed liquids easily and promote dropwise condensation.
2. Contact angle modeling has been modeled or modified and experimentally confirmed for many engineered surfaces including micro or nano structured hydrophobic or hydrophilic surfaces. No references were found for contact angle modeling of hydrophobic-hydrophilic surfaces.
3. Several studies have been done on the effectiveness of hydrophobic surfaces on the promotion of dropwise condensation. Some associated condensation heat transfer information for hydrophobic surfaces has been documented. No cross-references have been found for comparison of condensation heat transfer data for various hydrophobic surfaces.
4. The detailed mechanism of droplet growth and movement on various engineered surfaces are still being investigated, but is it clear that hydrophobic surfaces promote dropwise condensation and self-propelled jumping drops are observed

from a superhydrophobic surface with nanoscale surface roughness. The detailed droplet dynamics of hydrophobic-hydrophilic surfaces remains to be studied.

5. To date, very few data have been validated concerning heat transfer coefficients from humid air relevant to dropwise condensation. Most correlations used for humid-air condensation are not directly applicable since they do not take into account micro or nano structured features of hydrophobic surfaces.

CHAPTER III

DESIGN AND FABRICATION OF ENGINEERED SURFACES

3.1. Design of Engineered Surfaces for Enhanced

In an effort to understand and enhance condensation dynamics on nano- and micro-textured surfaces, several engineered surfaces were designed, fabricated and characterized using a variety of newly developed coating schemes. Different surfaces were designed and fabricated including four hybrid surfaces, one nanoparticle-based surface, one PTFE surface, and self-assembled monolayers (SAMs), in addition to the control surface, a silicon wafer. Hybrid surfaces were designed, fabricated and characterized first to understand the effect of spatially controlled hydrophobicity on droplet nucleation, growth, coalescence and shedding as discussed in detail below. The other surfaces were also characterized as discussed below.

3.2. Motivation for Hybrid Surface Structure

It is well known that nucleation of condensate droplets on hydrophobic surfaces requires a higher degree of subcooling than is required for surfaces that are already wetted [75]. On the other hand, hydrophobic surfaces are desired because they can easily shed droplets. Furthermore hydrophilic sites are highly desirable since they can enhance droplet nucleation and adequate liquid wetting of the surface as predicted by Wenzel theory [40]. Fabrication and characterization of hybrid surfaces have already been carried out by Drelich et al. [76] and Morita et al. [77] who determined the effects of alternating hydrophobic and hydrophilic strips on droplet contact angle. Varanasi et al.

[8] investigated the effects of using hydrophobic-hydrophilic surfaces on heterogeneous nucleation. Saha and Mitra [78] theoretically analyzed a microchannel consisting of hydrophilic and hydrophobic layers. However, few studies have been able to demonstrate the relationship between hybrid surface morphology and contact angle from the context of the Cassie-Baxter and Wenzel theories. In the current work, hybrid surfaces have been designed, fabricated and tested under controlled laboratory conditions. The hybrid surface consists of hydrophilic tops and hydrophobic valleys or troughs to promote Cassie-Baxter type droplets to enhance dropwise condensation, specifically during the nucleation.

3.3. Design of Hybrid Surface

In order to design and develop hybrid surfaces which promote Cassie-Baxter type droplets, a surface-energy-based model has been developed to predict the equilibrium contact angle, accounting for surface material (i.e. hydrophobic or hydrophilic), micropillar width, micropillar height, and gap size. The model takes into account the unique topography of a designed hybrid surface as shown in Fig. 2a and 2b.

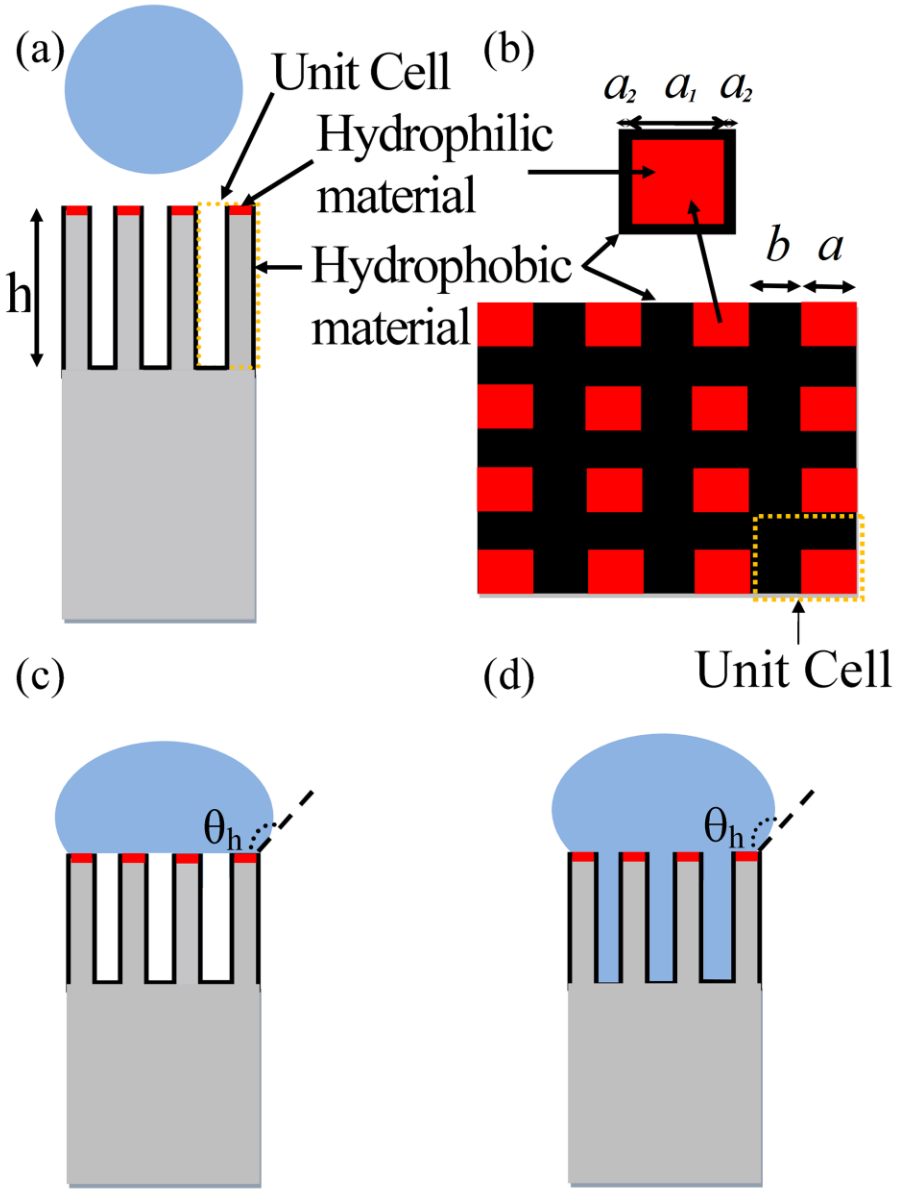

Figure 2. Schematic drawings of (a) side view of the hybrid surface, (b) top view of a hybrid surface, where a_1 is the width of hydrophilic material, a_2 is the width of hydrophobic material, (c) a droplet in the Cassie and Baxter state, and (d) a droplet in the Wenzel state

The model was developed by accounting for the surface energy of a unit cell before a droplet contacts the hybrid surfaces, as follows:

$$E = \gamma_{SV1} \times \frac{a^2}{(a+b)^2} \times (a+b)^2 + \gamma_{SV2} \times \left(1 - \frac{a^2}{(a+b)^2} \right) \times (a+b)^2 + 4ah) \quad (11)$$

where γ_{SV1} and γ_{SV2} correspond to surface tension at the solid-vapor interfaces for hydrophilic surface and hydrophobic surfaces, respectively. The micropillar width and gap size are denoted as *a* and *b*, respectively, and *h* denotes the micropillar height. After a droplet contacts the hybrid surface, it reaches the Cassie–Baxter state [39] as shown in Fig. 2c. The surface energy in the unit cell at that state is given by:

$$\begin{aligned} E = {} & \gamma_{SL1} \times \frac{a^2}{(a+b)^2} (a+b)^2 + \gamma_{SV2} \times (4ah + \left(1 - \frac{a^2}{(a+b)^2} \right) (a+b)^2) \\ & + \gamma_{LV} \times (\left(1 - \frac{a^2}{(a+b)^2} \right) (a+b)^2) + \gamma_{LV} \times \cos\theta_h (a+b)^2 \end{aligned} \quad (12)$$

where γ_{SL1} is the surface tension at the solid-liquid interface for the hydrophilic surface, and γ_{LV} is the surface tension at the liquid-vapor interface. The difference in surface energy between Equation (12) and Equation (11) is as follows:

$$\begin{aligned} dE = {} & (\gamma_{SL1} - \gamma_{SV1}) \left(\frac{a^2}{(a+b)^2} \right) (a+b)^2 \\ & + \gamma_{LV} \times \left(1 - \frac{a^2}{(a+b)^2} \right) (a+b)^2 + \gamma_{LV} \times (a+b)^2 \cos\theta_h \end{aligned} \quad (13)$$

Equation (13) can be simplified by grouping *a* and *b* as follows:

$$A = \frac{a^2}{(a+b)^2} \tag{14}$$

In order to take into account of the very thin hydrophobic edge (layer) on the top surface of each micropillar, Equation (15) is also used [79] as follows:

$$\cos\theta_{1e} = x \times \cos\theta_1 + (1-x) \times \cos\theta_2 \tag{15}$$

where θ_1 is the contact angle of the liquid droplet on a flat hydrophilic surface, θ_2 is the contact angle of a liquid droplet on a flat hydrophobic surface, and the area fraction *x* is the relative area of the hydrophilic material with respect to the total top surface area. The effective intrinsic contact angle (θ_{1e}) of the top surface was calculated using the area fraction *x*, and the respective contact angles of both surfaces. Using the area ratio *A*, the well-known Young's equation [80] and minimizing Equation (13) (setting Equation (13) to zero), the contact angle θ_h on the hybrid surface can be found as follows:

$$-1 + A(1 + \cos\theta_{1e}) = \cos\theta_h \tag{16}$$

Equation (16) was derived assuming that the liquid droplet sits on top of the micropillars exclusively (i.e. Cassie-Baxter droplet), without interacting or touching the

side or bottom surfaces. The model predicts that increasing effective contact angle (θ_{1e}) should result in higher equilibrium contact angles (θ_h) as a Cassie-Baxter type droplet. Higher contact angles can be achieved by using more hydrophobic materials or increasing gap size, *b*. Droplets can also reach the Wenzel state [40] even on a hybrid surface as shown in Fig. 2d, where surface energy in the unit cell is given by:

$$E = \gamma_{SL1} \times \frac{a^2}{(a+b)^2}(a+b)^2 + \gamma_{SL2} \times (4ah) + \gamma_{SL2} \times \left(\left(1 - \frac{a^2}{(a+b)^2}\right)(a+b)^2\right) + \gamma_{LV} \times \cos\theta_h (a+b)^2 \quad (17)$$

where γ_{SL2} is the surface tension at the solid-liquid interface for the hydrophobic surface. The difference in surface energy can be calculated by subtracting Equation (11) from Equation (17) as follows:

$$dE = (\gamma_{SL1} - \gamma_{SV1})\left(\frac{a^2}{(a+b)^2}\right)(a+b)^2) + (\gamma_{SL2} - \gamma_{SV2})(4ah + \left(1 - \frac{a^2}{(a+b)^2}\right)(a+b)^2) + \gamma_{LV} \times (a+b)^2 \cos\theta_h \quad (18)$$

Surface roughness which is defined as the total surface area to the projected surface area of the hybrid surface for unit cell is:

$$R = 1 + \frac{4h}{a\left(1 + \frac{b}{a}\right)^2} \quad (19)$$

By combining the area ratio *A*, surface roughness *R*, using the Young's equation, while minimizing Equation (18), the contact angle θ_h on the hybrid surface can be expressed as follows:

$$A(\cos\theta_{1e} - \cos\theta_2) + R\cos\theta_2 = \cos\theta_h \tag{20}$$

Equation (20) was derived assuming that the liquid droplet completely fills the gaps among the micropillars, which is the case for Wenzel type droplets. The equations presented above were used to make sure that the structural features of the hybrid surfaces were sized properly to ensure adequate wetting as discussed in greater detail in Chapter V.

3.4. Fabrication and Characterization of Hybrid Surfaces

The designed hybrid surfaces (Figure 2a) consisting of a micropillar array of 25 x 25 μm squares with hydrophobic and hydrophilic sites were fabricated through photolithography processes by the Engineer Research Development Center (ERDC) of the U.S. Army Corps of Engineers in Champaign, IL [81]. Silicon wafers were chosen as substrates for the hybrid surfaces. Four hybrid surfaces with edge-to-edge spacings of 12.5 μm, 25μm, 37.5 μm, 50 μm were fabricated.

Hybrid surfaces were fabricated through designed processes as depicted in Figure 3 and described as follows:

1. A single-side polished silicon wafer with 4-inch <100> size is rinsed with Acetone, Isopropyl Alcohol (IPA), DI Water, IPA, and dry by spraying nitrogen gas (N2).
2. Clean the Silicon wafer (polished side) by using Oxygen plasma (100 W Power for 1 minute) with the March Reactive Ion Etcher (RIE).
3. Grow 250nm of SiO_2 by loading the wafer in an oxidation tube furnace at 1100℃ for 4 hours, 4 minutes.
4. Clean the wafer by repeating steps 1-2
5. Wafer is annealed (pre-bake) on hotplate at 110℃ for 1 minute.
6. Spin 500 μL of AP8000 (Adhesion Promoter) onto the wafer at 3000 RPM for 30 seconds.
7. Spin 3000 μL of SPR-220 Photoresist onto the wafer at 3000 RPM for 30 seconds.
8. Wafer is annealed on a hot plate at 60℃ for 2 minutes and at 110℃ for 1 minute.
9. Cool down the wafer for 1 minute.
10. The wafer is aligned with the design mask (Figure 4), and the photoresist is exposed to 405 nm wavelength (H-Line) UV light, at a power of 21.2 mW/cm2 for 12 seconds.
11. Make the alignment marks, with the solution composed of DI

water and AZ 400K developer (4:1 ratio).

12. Place the wafer in the solution (4:1 DI water and AZ 400K) for 1 minute and submerge the wafer in a DI water bath for 2 minutes.
13. Hard bake the photoresist on a hotplate at 110℃ for 5 minutes.
14. Etch the wafer by placing it into the Buffered Oxide Etchant (BOE) solution for 2 minutes and 30 Seconds, and submerge the wafer in a DI water bath for 1 minute 30 seconds
15. Etch the wafer by using the Bosch Process with the Plasmatherm Inductively Coupled Plasma Deep Reactive Ion Etcher (ICP-DRIE).
16. Deposit 70 nm of Teflon-like material with C_4F_8 plasma.
17. Place the wafer into AZ 400T photoresist stripper for 24 hours at room temperature.

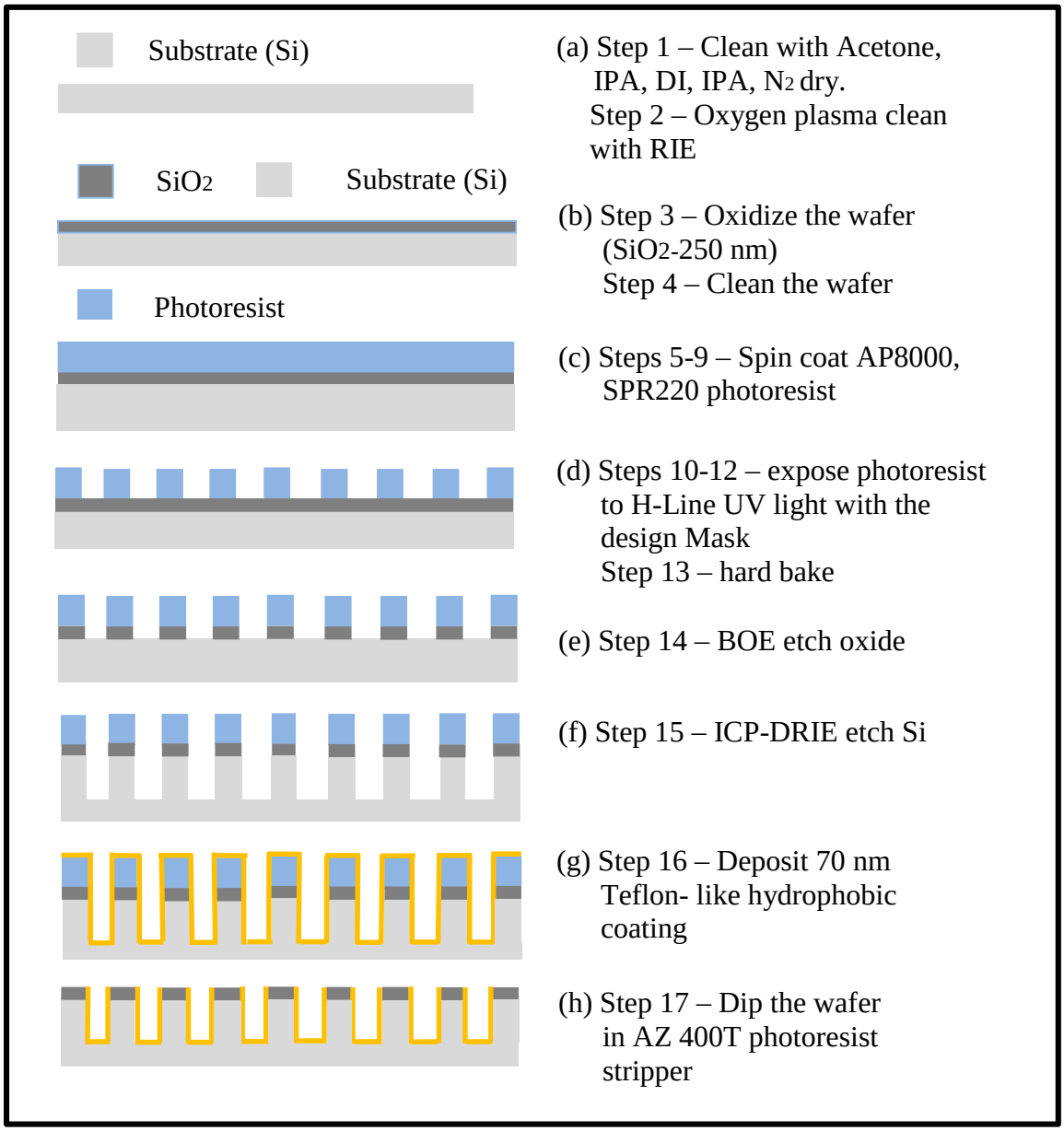

Figure 3. Schematic drawings of processes for hybrid surface fabrication

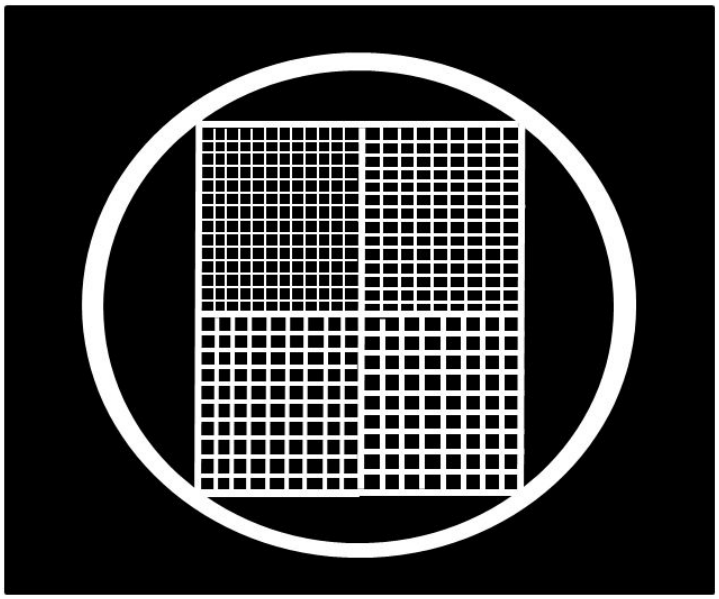

Figure 4. Schematic drawings of photomask design

All the hybrid surface samples consist of a micropillar array of 25 x 25 μm squares which were made as shown in Figure 5. The micropillar width of hybrid surface, *a*, was measured using SEM images. The width of hydrophobic surface, a_2, was estimated based on a constant deposition rate of the Plasmatherm ICP-DRIE which deposits a total of 70 nm of hydrophobic material per sample. The width of hydrophilic surface, a_1, was calculated by knowing *a* and a_2. All the dimensions of the surfaces are shown in Table 1.

Table 1. Physical dimension of micropillars

sample	a (μm)	a_1 (μm)	a_2 (μm)	b(μm)	h(μm)
1	24.11	23.96	0.07	14	78
2	22.83	22.68	0.07	24	78
3	23.23	23.08	0.07	38	78
4	24.63	24.48	0.07	49	78

a: micropillar width , a_1: the width of hydrophilic surface

a_2: the width of hydrophobic surface, b: gap size

h: micropillar height

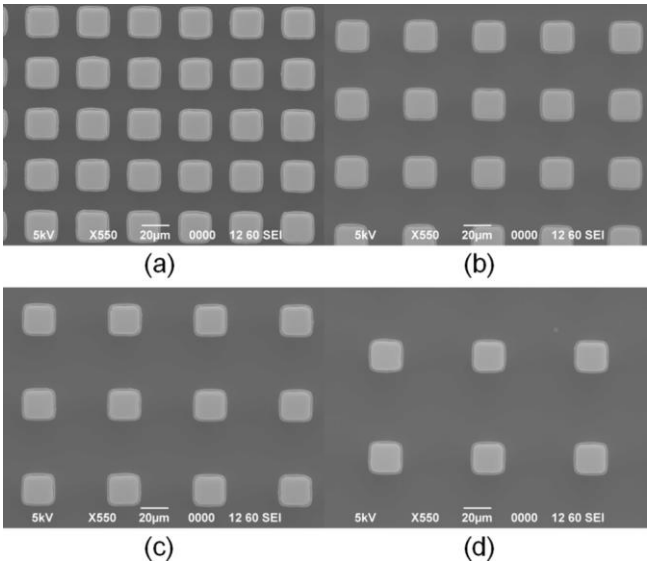

Figure 5. SEM images of a hybrid surfaces with a micropillar array with spacing values of (a) 12.5 μm, (b) 25 μm (c) 37.5 μm, and (d) 50 μm

In order to verify that each surface was made according to the design criteria, an Energy-Dispersive X-Ray Spectroscopy (EDX) instrument was used to verify the chemical composition on the tower sidewalls and the top of the towers. EDX data indicate that the tower tops only include Silicon and Oxygen (SiO_2) while tower sidewalls also include a Carbon and Fluorine signature, suggesting the deposition of teflon-like material ($(C_2F_4)_n$) on the surface as shown in Figure 6.

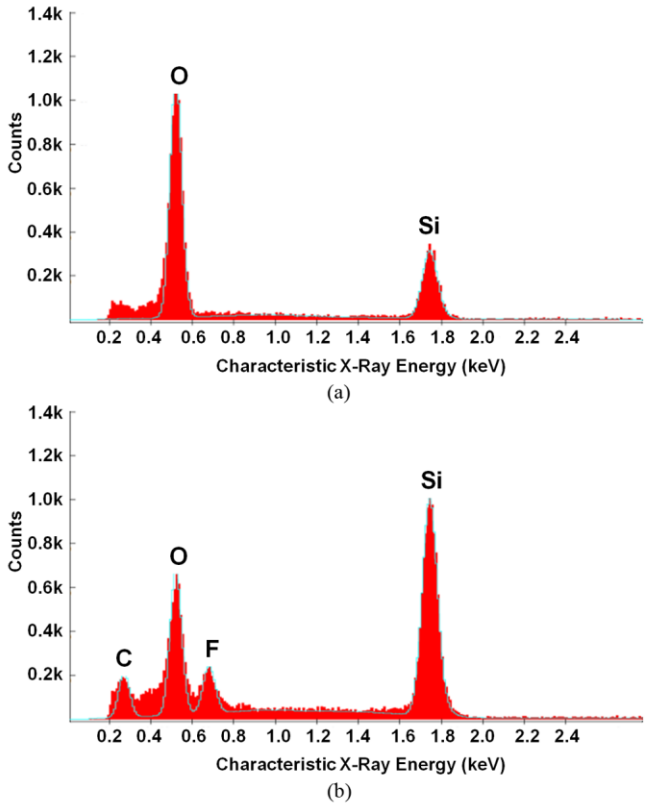

Figure 6. EDX spectrum analysis (a) tower tops and (b) tower sidewalls

Time-of-Flight Secondary Ion Mass Spectrometry (TOF-SIMS) was also performed to detect oxygen and fluorine signatures in SiO_2 and C_2F_4, respectively. An example of an array of towers under TOF-SIMS is shown in Figure 7. Figure 7a shows the total counts recorded by the instrument. Figure 7b shows fluorine signature in red color which indicates the presence of the hydrophobic $(C_2F_4)_n$. Figure 7c shows oxygen signature in green color which indicates the presence of the hydrophilic SiO_2. Figure 7d shows a combination overlay of fluorine and oxygen signatures.

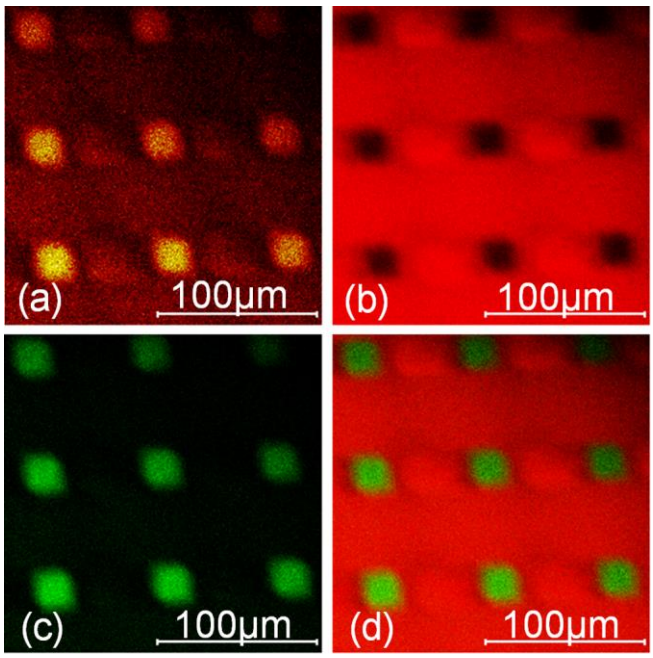

Figure 7. TOF-SIMS of hybrid surfaces (a) total counts, (b) fluorine location (red), (c) oxygen location (green), and (d) oxygen and fluorine overlay

3.5. Fabrication of Nanoparticle-based, Polytetrafluoroethylene, and Self-assembled Monolayers Engineered Surfaces

Other engineered surfaces were made and fabricated to understand the effect of wetting characteristics on dropwise condensation behavior. Silicon wafers were chosen as substrates for all the condensation surfaces because of their high thermal conductivity and surface quality. Highly polished p-type 3 cm x 3 cm silicon wafers with a thickness of 500 μm were used as substrates. More types of engineered surfaces were fabricated including nanoparticle-based hydrophobic surface, polytetrafluoroethylene (PTFE) surface, and self-assembled monolayers (SAMs) surface. For the superhydrophobic surface (Figure 8), 2 wt.% silicon oxide (SiO2) nanoparticles (colloidal from Alfa Aesar) with mean diameter of 20 nm were dispersed in a commercial hydrophobic solution (Hydrobead-T). The silicon substrate was coated with the mixture using a spin-coater at 500 rpm for 20 s, followed by baking at 100 ℃ for 30 mins.

The hydrophobic PTFE surface was prepared by spin-coating the 2 wt. % Teflon-AF 1600 solution on the silicon substrate at 800 rpm for 3mins [82]. The silicon substrate ended up with a 230 nm thick Teflon-AF film. The hydrophobic SAMs coating was done by dipping the silicon substrate into a solution of 2% HDFS (heptadecafluoro-1,1,2,2-tetra-hydrodecyl trimethoxysilane from Gelest Inc., Morrisville, PA, USA) in ethanol for 15 h. Then the coating was heated at 130 ℃ for 15 min.

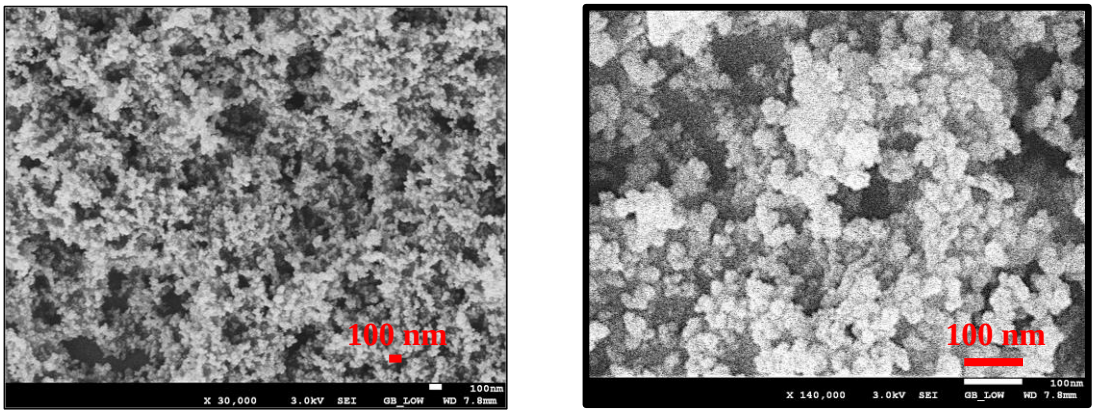

(a) (b)

Figure 8. (a) SEM images of the nanoparticle-based hydrophobic surface (b) high-magnification SEM image of nanoparticle coatings

In summary, several engineered surfaces have been designed, fabricated and tested in order to exhibit distinct wetting behaviors. These surfaces were also used to during dew condensation experiments to determine the effect of wettability on condensation heat transfer.

CHAPTER IV

DESCRIPTION OF EXPERIMENTAL FACILITY

The fabricated engineered surfaces were characterized for their surface morphology, composition, and wetting behavior by measuring droplet contact angle. Images of engineered surfaces were obtained using a Scanning Electron Microscope (SEM), Energy-Dispersive X-Ray Spectroscopy (EDX) was also used to identify the chemical composition of hydrophillic and hydrophobic features on the surfaces. Droplet contact angle was measured using a goniometer. To study the thermophysical phenomena responsible for dropwise condensation, other facilities were required and used as well. To carry out condensation experiments, factors that affect dew condensation on surfaces, such as air temperature, humidity, and air velocity needed to be measured and controlled. In this chapter, descriptions of all the experimental set-up and associated measurement systems used in the study are presented.

4.1. Scanning Electron Microscopy

The Scanning Electron Microscopy **(**SEM) is a high resolution field emission scanning electron microscope as shown in Figure 9. SEM with Energy-Dispersive X-Ray Spectroscopy (EDX) capabilities was used to observe specimen at magnifications up to 1,000,000X. SEM needs to operate under high vacuum conditions. High Vacuum typically requires that the sample be conductive or coated for conduction purposes. Coating reduces beam penetration and allows for sharper images. After fabricating engineered surfaces, the surfaces were visualized using an SEM with EDX capabilities. Images were obtained at 550X magnification and 5 kV electron energy. A top view of

each type of surface was obtained to characterize surface morphology and composition as shown in Figure 5 in Chapter III.

Figure 9. JEOL JSM-7500F field emission SEM system

4.2. Goniometry

Characterization of surface wettability was obtained using a goniometer as shown in Figure 10. A goniometer was used to measure droplet contact angles. Deionized water droplets were placed on a surface for measurements. Advancing and receding angle were also recorded and used to determine contact angle hysteresis. In order to measure advancing contact angles, an initial droplet of about 9 μL was deposited onto a surface.

Then the goniometer starts taking images when the pipet starts dispensing water at a rate of 0.5 μL/s. The goniometer records one image per second. The receding contact angles were obtained by sucking fluid back into the pipette. When the pipet starts to absorb water at 0.5 μL/s, the goniometer starts recording images. During measurements of the static contact angle, the pipet was lowered until the 9 μL droplet was deposited onto the surface. The values of static contact angle were in the range between the values of advancing and receding angle as defined in Chapter V.

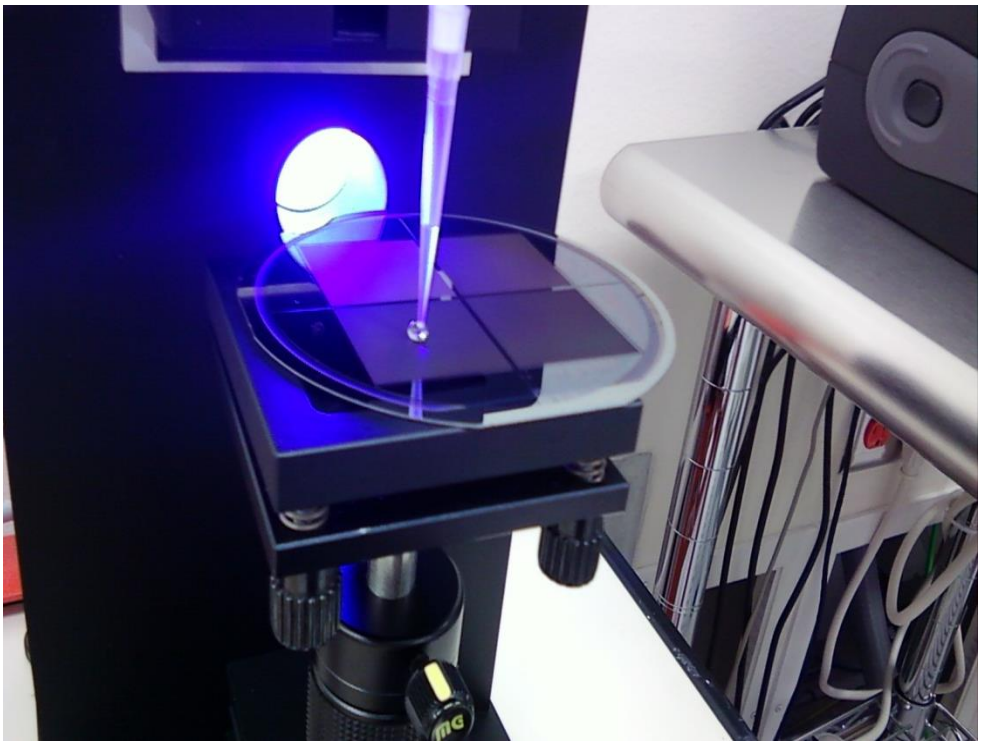

Figure 10. Contact angle measurement system (KSV Instruments CAM 200)

4.3. Environment Scanning Electron Microscopy

The environment scanning electron microscopy (ESEM) as shown in Figure 11 was used primarily to conduct in-situ condensation experiments at low pressure. It can be used to observe outgassing or highly charging materials without conductive coating. Before loading the samples, the samples were cleaned, and properly mounted. The sample were electrically grounded with conductive tape to minimize specimen charging. The wetting behavior of engineered surfaces during water condensation was visualized *in-situ*. An 1 x 1 cm sample was placed on a holder with a tilt angle of 63°~66°. The sample holder was placed on a peltier cooling stage mounted inside the ESEM. The electron beam voltage was set at 15 or 20 keV in order to ensure better quality for images while minimizing beam heating. The temperature of the peltier cooling stage was fixed at - 1℃. To start the condensation, the vapor pressure was slowly increased from 5 Torr to 8 Torr. Figure 12 depicts a sample of ESEM image during dropwise condensation on an engineered surface.

Figure 11. FEI ESEM Quanta 200 system

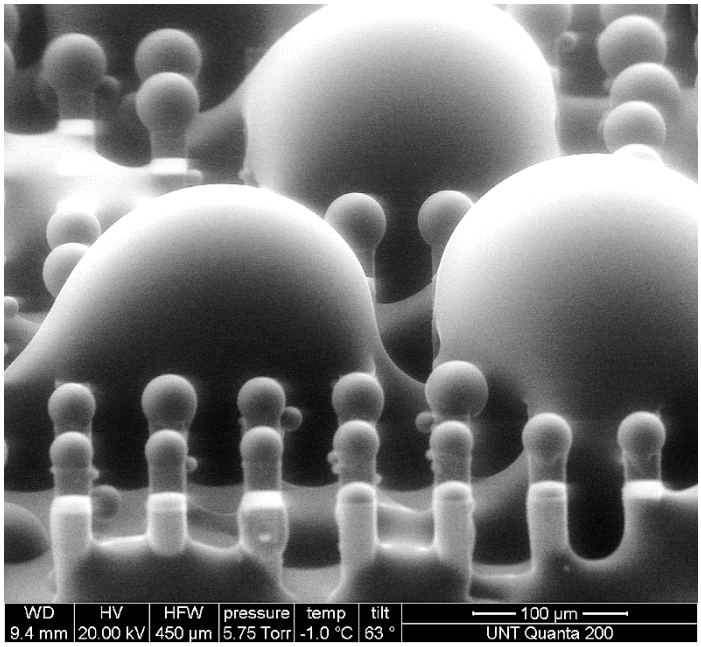

Figure 12. A sample of ESEM image during dropwise condensation on an engineered surface

4.4. Condensation Experiment Apparatus

The experimental setup used for condensation experiments consisted of an air conditioning module, a cooling system, and a data acquisition system for condensation experiments as shown in Figure 13. The test section was constructed out of acrylic glass panels. Ambient air basically enters the test section being propelled by an electrical fan. Depending on the humidity requirements of the test condition, saturated air from a small scale boiler or dry nitrogen gas were mixed with air. The relative humidity (RH) and flow velocity were measured using a hydrometer and an anemometer, respectively. The cooling cell consisted of a copper stage, thermocouples, and a thin-film heat flux sensor as shown in Figure 14. The cell was connected to a chiller to control the test surface temperature. The condensation experiments were conducted with the temperature and humidity inside the test section set at 21±1.0˚C and 80-85%, respectively. The temperature of the cooling cell was set between at 7 and 13˚C by the chiller. The speed of moist air was set in the range of 0.2-0.5 m/s.

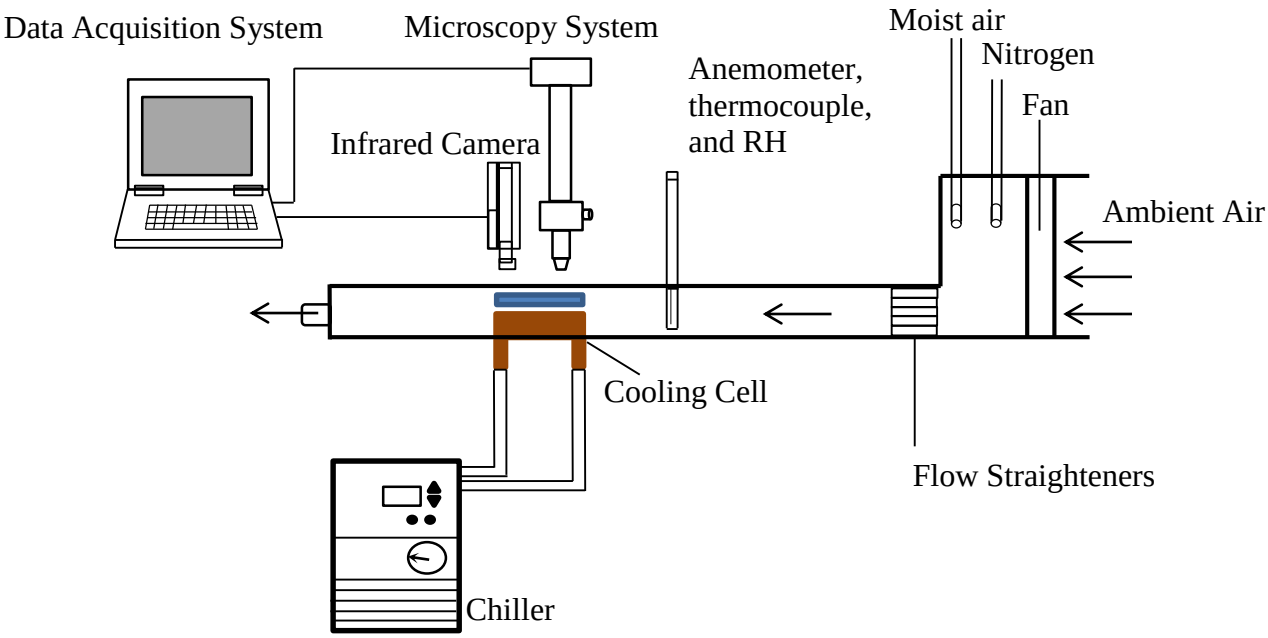

Figure 13. Schematic of experimental setup

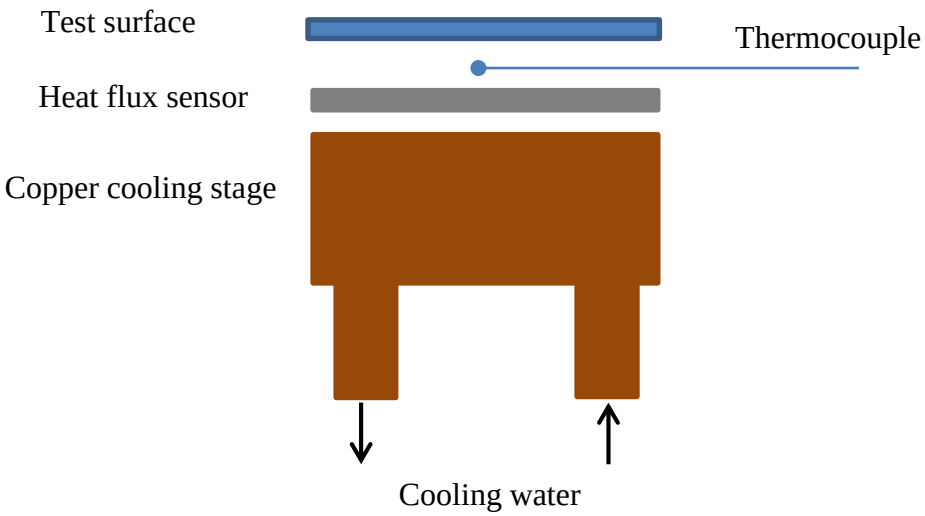

Figure 14. Custom cooling cell

4.5. Imaging System

A digital microscopy system provided in-situ visualization to image the size and time scales characteristics of dropwise condensation. The system consisted of a high resolution optical microscope and a digital camera system. A custom microscope was assembled to view the test surfaces through the viewing ports in the test section. A light emitting diode (LED) had been integrated into the microscope with a plate beam-splitter. Therefore, light could be delivered to the test surfaces on the vertical axis through an objective lens. The magnification of the objective lens was set to 5X or 50X as listed in Table 2 which were proven to be enough for observing individual micro scale droplets. In order to image droplets accurately within the test section, the objectives have a long working distance. The camera had a resolution of 1392 × 1040 pixels with an individual pixel size of 4.65 × 4.65 microns. A computer was used to control the camera and to record images sequentially. Images of the engineered surface were obtained with the microscopy system as shown in Figure 15. The Image analysis tool, ImageJ was used for droplet size measurement and surface coverage measurement.

Table 2. Objective lens specifications

Objective	Numerical Aperture	Working Distance (mm)	Camera Calibration (μm/pixel)
5X	0.14	37.5	0.9
50X	0.42	15	0.1

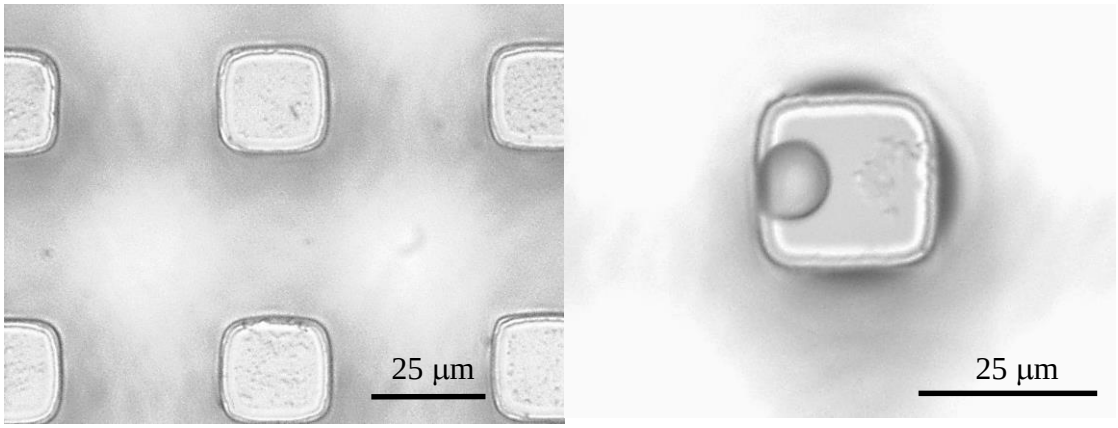

(a) (b)

Figure 15. Images of (a) a micropillar array with a micropillar width of 25μm, (b) a micro scale droplet sitting on top of a micropillar

4.6. Temperature Measurement System

Surface temperature was measured using an infrared camera (FLIR A325) located above each engineered surface. The camera consists of a close up lens, which has a spatial resolution of 25 μm, and the field of view of 8 mm by 6 mm. The working distance of the lens was set to 21 mm. The inherent temperature range of the camera was between 0 and 350 ℃. Figure 16 depicts a sample of an infrared image during dropwise condensation on an engineered surface.

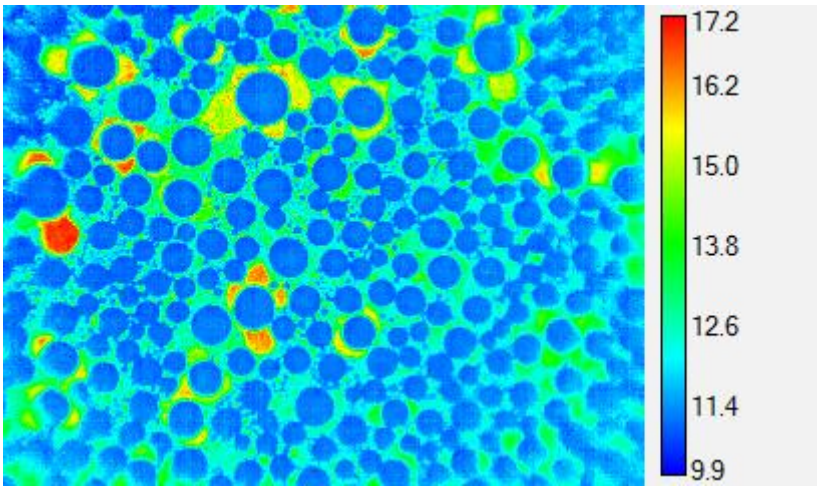

Figure 16. IR images during dropwise condensation on an engineered surface (cold water droplets are shown as blue dots)

A type-T thermocouple was also used to measure the underside temperature of each test surface. A thin film heat flux sensor was used to directly measure heat flux through each test surface. Therefore, the upper surface temperature of the test surface could also be calculated by using the conduction equation assuming one-dimensional heat conduction as follows:

$$T_{surface} = \frac{q'' \Delta y}{k} + T \tag{21}$$

4.7. Experimental Procedures

The following procedures were followed to set the desired experimental conditions when using the experimental apparatus.

1. The test section was initially purged with dry nitrogen for 15 minutes to remove all moisture in the section.
2. The chiller was set at the desired temperature to supply steady cooling water to the cooling cell.
3. After the desired surface temperature had been reached, the fan would be turn on at the desired speed.
4. The RH controller was set at the desired relative humidity to control the supply of steam coming from a small-scale boiler.
5. Temperatures throughout the system on both surface and moist air were recorded.
6. The image data were recorded when the moist air flowed into the test section.

For all tests, environmental parameters that could be varied with the apparatus included relative humidity of the air, air velocity, and surface cooling temperature as shown in Table 3.

Table 3. Air temperature, humidity, velocity, and cooling temperature ranges of experimental facility

Parameter	Lower Operating Value	Upper Operating Value
Relative Humidity, %	30	80
Air Velocity, m/s	0.2	0.5
Reynolds Number of flowing air	300	770
Cooling temperature,˚C	7	13

4.8. Calibration

All thermocouples were calibrated in a circulating water bath using resistance temperature detector (RTD) as a common reference. The TSI anemometer probe and hydrometer were calibrated at the factory and were shipped with calibration information. The thin-film heat flux sensor was brand new and came with factory calibration information at the onset of this study. The accuracy associated with each measurement type are reported in Table 4

Table 4. Experimental uncertainties for measurements

Measurement	Accuracy
Temperature	±0.1
Relative Humidity	±2.2% (RH)
Heat flux	±0.1 (W/m^2)
Air Velocity	±0.02 (m/s)

For calibration purposes, baseline experiments were conducted using a horizontal copper plate to validate the performance of the condensation heat transfer system. Figure 17 shows experimental and analytical heat transfer results for a plate under constant temperature and laminar flow conditions with no condensation taking place. The analytical results were obtained using the Nusselt number equation (22) [83]. As Figure 17 shows, the analytical and experimental results are in very good agreement with each other.

$$Nu = 0.664\,\mathrm{Re}^{0.5}\,\mathrm{Pr}^{1/3} \tag{22}$$

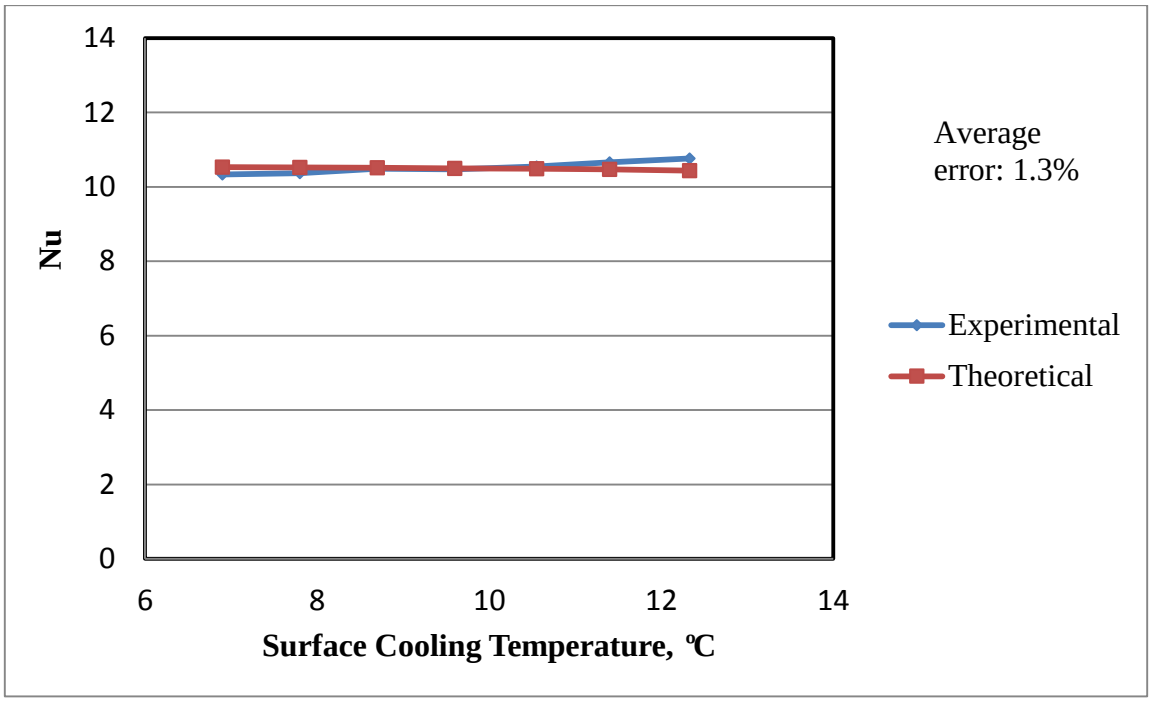

Figure 17. Comparison between experimental and analytical heat transfer data of flowing air without phase change at Re of 311

4.9. Emissivity Measurement

In order to obtain surface temperature by using an infrared camera, the emissivity of an engineered surface needed to be measured. The standard ASTM E1933 "Standard test methods for measuring and compensating for emissivity using infrared imaging radiometers" was used. Procedures are summarized as follows:

1. Measure the digital reading of the irradiance from surroundings where the temperature measurement was performed. A reflective foil over the surface was placed and measured by the IR camera in digital counts. The foil would suppress the irradiation from the object and make the camera receive the reflection from the surrounding only.
2. Apply a small coating of known emissivity on an engineered surface.

3. Heat the surface until the surface temperature is 30℃ above the temperature of the surroundings. This is done by placing the surface in the laboratory oven at three different temperatures. Measure irradiance counts from both the surface and coating.
4. Calculate the emissivity of the surface using the following equation:

$$\varepsilon_{obj} = \frac{D_{obj} - D_{surr}}{D_{ref} - D_{surr}} \varepsilon_{ref} \tag{23}$$

where D represents the digital reading of the IR camera in counts. The reference used for this measurement was an electrical vinyl tape Super 88 with a known emissivity value of $\varepsilon = 0.95 \pm 0.05$. The calculated emissivity values of a selected engineered surface (nanoparticle-based hydrophobic surface) at different temperatures are listed in Table 5:

Table 5 Emissivity values of the engineered surfaces at different temperatures

Nanoparticle-based surface	Temperature (℃)	55	61	70
	Emissivity	0.79	0.79	0.79
PTFE surface	Temperature (℃)	55	60	69
	Emissivity	0.34	0.34	0.33
Si surface	Temperature (℃)	54	60	75
	Emissivity	0.3	0.29	0.29

CHAPTER V

WETTABILITY AND CONDENSATION DYNAMICS ON ENGINEERED SURFACES

The fabricated engineered surfaces were studied to understand their wettability, and condensation dynamics behavior. Droplet contact angles were measured using the goniometer. Condensation droplet and film dynamics were observed using an environmental scanning electron microscopy (ESEM) and an optical microscope in conjunction with the condensation cell under ambient conditions.

5.1. Study of Droplet Wettability on Hybrid Surfaces

The wettability of a surface can be described by finding its "droplet contact angle," which describes the shape of a droplet as it sits on a surface. The contact angle is also the direct result of surface free energy minimization of the corresponding interfacial system. Contact angle measurements were performed using a goniometer for each spacing design. Advancing and receding angles were measured using droplet volumes in the range from 5 to 50 μl. Equilibrium contact angles were measured at droplet volumes around 9 +/- 0.62 μl. The evaporation dynamics behavior was recorded after placing a 9 μl droplet on each sample at room temperature. Roll-off angles were measured by tilting the samples slightly after placing a 9 μl droplet on each sample until the droplet rolled off the surface via gravity. Average roll-off angles were obtained by averaging ten measurements per sample.

For the flat Si wafer coated with Teflon (hydrophobic surface), the advancing, receding, and equilibrium (droplet) contact angles were 125.5°, 98.7°, and 119°, respectively. For the sidewalls of the micropillars, the intrinsic advancing angle on Teflon (flat) surface was found to be 125.5°. Due to scalloping on the sidewalls [14], the effective advancing angle for θ_2 on the sidewalls was 155.9° (Wenzel roughness r = 1.57).

When advancing contact angles were measured, it was observed that when water was added, the contact line of each Cassie–Baxter state droplet moved almost parallel to the surfaces before it reached the next micropillar, resulting in extremely high advancing contact angles (up to 172.5°). This observation reveals that the hydrophobic edge around each micropillar has a dominant effect on the high advancing contact angles. In order to take into account this physical behavior using Equation (15), it was assumed that x was equal to 0 resulting in θ_{1e} being equal to θ_2. As shown in Figure 18(a), the predicted advancing contact angles fit the experimental data well when x was set to 0. It is evident that the behavior of advancing water droplets on the hybrid surfaces can still be explained by the Cassie–Baxter model based exclusively on the hydrophobic material properties of the micropillar edge. Figure 18(a) also shows that as *b/a* of the micropillars increases, the experimental and predicted contact angles also increase.

When measuring the receding contact angle, liquid was gradually removed and the three phase contact line moved accordingly, coming in close contact with the hydrophobic edges of the micropillars. It was observed that when the volume of a droplet was decreased, the three phase contact line (TCL) appears to be pinned down at

the hydrophobic edge until the contact angle reached a minimal value which was recorded and designated as the receding contact angle. Once the minimum angle was reached, the TCL of the droplet moved to the adjacent micropillar where the contact angle reached a larger value. Li and Amirfazli [84] demonstrated similar behavior and attributed the variation in contact angle to the change in free energy barrier as three phase contact line transitioned from one metastable position to another. Figure 18(b) shows receding contact angle as a function of the geometric parameter *b/a* based on the proposed model and experimental data. Equation (16) over predicts contact angle since it does not take into account the dynamic interaction between the micropillar edges and droplet when the fluid is receding. It is also evident that the droplet dynamic behavior conforms better to the Cassie-Baxter state. In order to understand the receding droplet behavior better, a close up view of the receding TCL during evaporation at room temperature was observed using a high resolution optical microscope. It was observed that the TCL receded in a stepwise manner. Experimental observations reveal that as a droplet starts detaching from a micropillar, the TCL moves quickly to the next micropillar even if most of the top surface is hydrophilic. This observation indicates that the hydrophobic edge also has an effect on the receding TCL and the receding contact angle.

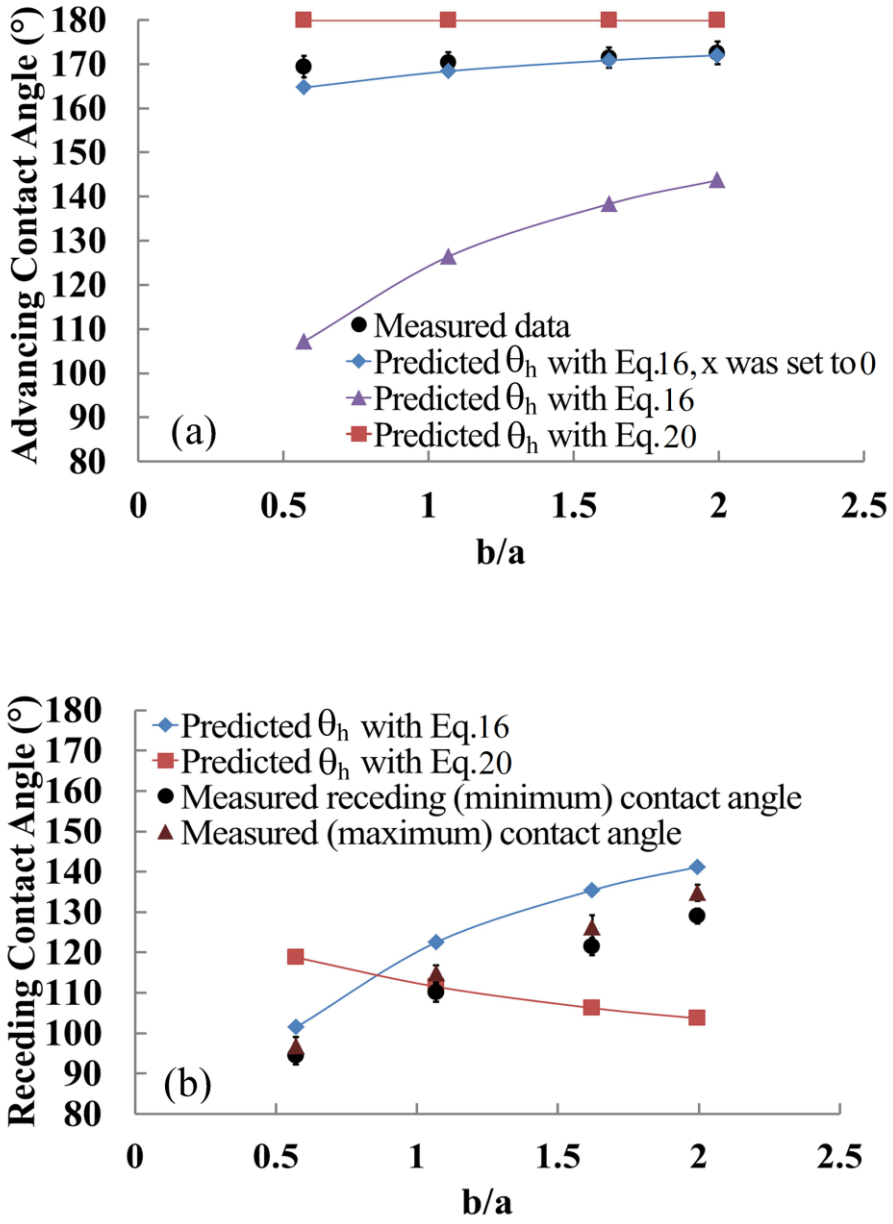

Figure 18. (a) Comparisons of the measured advancing contact angle (CA) on hybrid surfaces. (b) Comparisons of the measured receding contact angle (CA) on hybrid surfaces

Recent papers [16, 85, 86] show that the equilibrium contact angle on a surface containing square pillars is difficult to predict precisely. The deviations of the theoretical

values from the experimental equilibrium contact angles could be attributed to the strong pinning effect on the sharp hydrophobic edges of the pillars [86]. Furthermore, the contact angle is sensitive to natural and ambient vibrations [87]. In order to minimize the effect of ambient conditions on contact angle, the equilibrium contact angle can also be defined as follows [5, 15, 56, 87]:

$$\theta_{eq} = \frac{\left(\theta_{adv} + \theta_{rec}\right)}{2} \tag{24}$$

where θ_{adv} and θ_{rec} are the predicted advancing and receding angles, respectively. Both angles were determined using Equations (16) and (20) for Cassie-Baxter state and Wenzel state droplets, respectively. Droplets in Cassie-Baxter state sitting only on top of the micropillars at four different spacing values are shown in Figure 19. Figure 20(a) shows that the equilibrium contact angles increase with micropillar spacing. This effect is consistent with the proposed Cassie-Baxter state model. Cansoy et al. [86] data from superhydrophobic surfaces with square pillars also show that the deviation between the Cassie-Baxter model and experimental values increased as the *b/a* ratio increased, consistent with the behavior depicted in Figure 20(a). The deviation between experimental and predicted contact angle values as *b/a* increases could be attributed to the slight level of "sagginess" of the unsupported liquid suspended between adjacent micropillars.

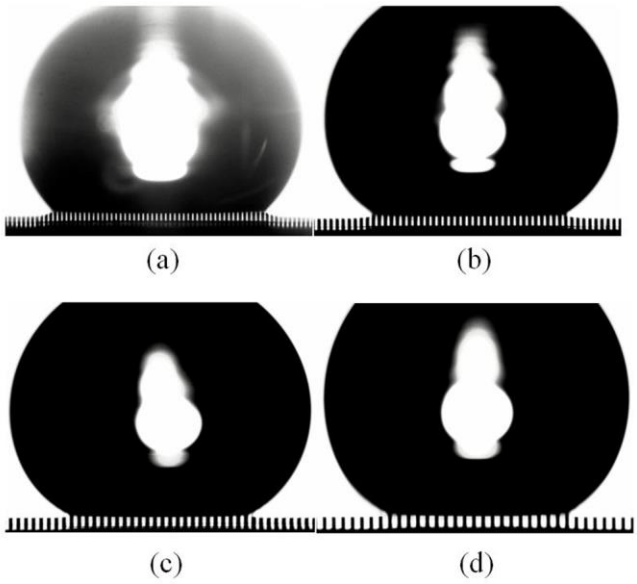

Figure 19. Water droplets in Cassie-Baxter state on hybrid surfaces with a micropillar array with spacing values of (a)12.5 μm, (b) 25 μm (c) 37.5 μm, and (d) 50 μm, respectively

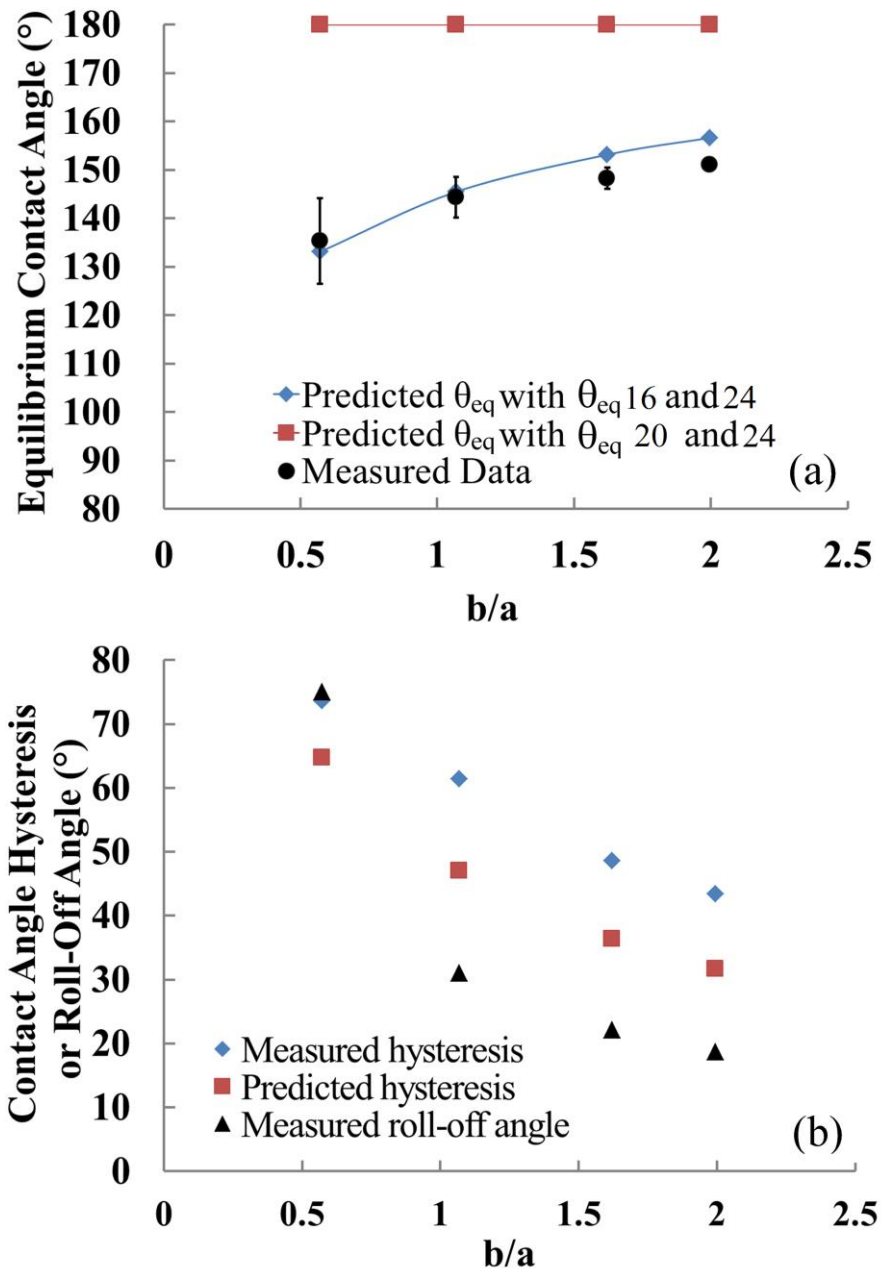

Figure 20. (a) Comparisons of the equilibrium contact angle (CA) on hybrid surfaces. (b) Contact angle hysteresis and roll-off angles of the hybrid surfaces

Contact angle hysteresis is another important criterion when designing a hybrid surface and is defined as the difference between the advancing and the receding contact angles of a liquid droplet. It is known that generally a surface with a low contact angle hysteresis results in a low roll-off angle [17, 88]. This is important when using a surface to remove moisture or to enhance dropwise condensation. A hybrid surface with this property can also exhibit a self-cleaning capability. From the results, the receding angle increases with *b/a*. However, the effect of *b/a* on advancing angle is less significant. The measured and predicted hysteresis and roll-off angles for different *b/a* values are shown in Figure 20(b). From Figure 20(b), contact angle hysteresis and roll-off angle decreases with *b/a*, because there is less surface area in contact with the liquid droplet as *b/a* increases. Moreover, predicted contact angle hysteresis is less than the measured value for *b/a* greater than 0.57. This behavior can be attributed to the fact that Equation (15), which was used to estimate contact angle only works well under ideal conditions and does not take into account the strong effect of the hydrophobic edge on the droplet while it is receding.

The observed hydrophobic edge effect on wetting behavior is similar to observations made by Extrand [89]. Extrand observed that when a droplet lies on a heterogeneous (hybrid) surface, the contact angle is dominated by the hydrophobic periphery even if most of the inner contact surface is hydrophilic in nature. Therefore, similar wetting behavior should be expected when a droplet is placed on different types of hybrid surfaces regardless of chemical composition of the hydrophilic material.

In summary, an energy-minimization-based model has been developed, and it is capable of predicting droplet contact angles on hybrid surfaces. For the advancing, receding, and equilibrium contact angle measurements, the model is in agreement with the experimental data. From the model and the experimental data, it is shown that increasing intrinsic hydrophobicity due to geometric effects and material composition yields higher contact angles on hybrid surfaces. It is concluded that the hydrophobic material on the edge of each micropillar results in a high advancing contact angle and high equilibrium contact angle while the hydrophilic material on the hybrid surface reduces the receding angle.

5.2. Effects of Condensation Dynamics on Wetting of Hybrid Surfaces

Condensation dynamics on hybrid surfaces was studied experimentally using the condensation system described in Chapter IV. To understand the relationship between droplet wetting and droplet dynamics, a closed look at droplet growth during condensation was undertaken by using an ESEM. ESEM images reveal that droplets impinging on hybrid surfaces exhibit a distinct wetting behavior that can be estimated using the surface energy-based model described above. However, condensed droplets display quite different wetting activities when they grow on hybrid surfaces as observed using the ESEM. The conditions that lead to specific wetting dynamics are the direct results of surface free energy minimization of the interfacial systems as described in Yao et al. [13, 15]. Figure 21(a) shows a droplet sitting on a hybrid surface in the Cassie–Baxter state. For such a condition, the surface energy of the interfacial system 1 (IS1) within a unit cell is given by Equation (12). Figure 21(b) shows a droplet sitting on a hybrid surface in the Wenzel state [40]. For such a condition, the surface energy of the interfacial system 2 (IS2) within a unit cell is given by Equation (17).

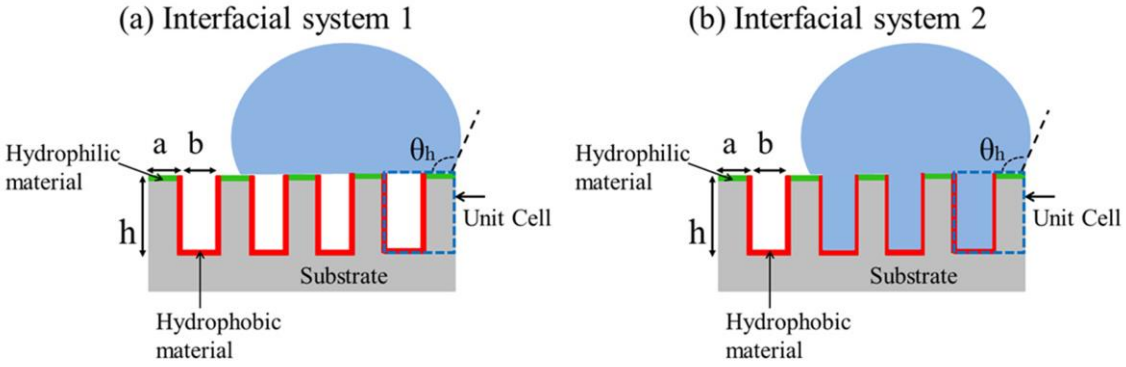

Figure 21. Schematic drawings of **(a)** the interfacial system1 (a droplet in the Cassie-Baxter state) and **(b)** the interfacial system 2 (a droplet in the Wenzel state)

To determine the critical condition corresponding to the transition between interfacial system 1 and interfacial system 2, the surface energies of both interfacial systems must be the same. Namely, Equations (12) and (17) were equal to each other as follows:

$$\gamma_{SV2}\times(4ah+(1-\frac{a^2}{(a+b)^2})(a+b)^2)+\gamma_{LV}\times((1-\frac{a^2}{(a+b)^2})(a+b)^2)= \gamma_{SL2}\times(4ah+(1-\frac{a^2}{(a+b)^2})(a+b)^2) \quad (25)$$

where γ_{SV2}, γ_{SL2}, and γ_{LV} is the surface tension at the solid-liquid interface of the hydrophilic surface, surface tension at the solid-vapor interfaces of the hydrophobic surface, and the surface tension at the liquid-vapor interface, respectively. The micropillar width and gap size are denoted as a and b, respectively, and h denotes the micropillar height.

As a result, a critical contact angle can be simplified as follows [90]

$$\theta_{critical} = \cos^{-1}\left(\frac{A-1}{R-A}\right) \tag{26}$$

When the effective equilibrium contact angle of a droplet on a flat hydrophobic surface θ_2 is smaller than the critical angle ($\theta_{critical}$), droplets would tend to wet the surface because of its lower surface energy. On the other hand, when θ_2 is larger than $\theta_{critical}$, droplets would rest on the top surfaces of the micropillars to minimize surface free energy. Therefore, the critical angle $\theta_{critical}$ could be used to estimate distinct condensation modes (i.e., dropwise mode versus filmwise mode) on a hybrid surface which is essential in understanding the relationship between wetting behavior and condensation dynamics. Equation (26) was derived exclusively for hybrid surfaces but it is similar to the wetting criterion used for hydrophobic surfaces [5, 13, 15, 31]. The difference in condensation behavior (i.e., dropwise versus dropwise-filmwise) resulting from changing micropillar spacing can be predicted by using Equation (26). For a hybrid surface consisting of a hydrophobic material such as a Teflon-like polymer ($(C_2F_4)_n$), the equilibrium contact angle (θ_2) is 112.1° with advancing and receding contact angles of 125.6° and 98.6°, respectively. All three hybrid surfaces exhibit hydrophobic properties as shown in Figure 22, which depicts droplet equilibrium contact angles for surfaces with different spacings. Table 6 shows that only Sample 3 has a calculated critical angle ($\theta_{critical}$) of 113°, which is larger than the measured equilibrium contact angle (θ_{eq}).

Therefore, when droplets nucleate and grow on Sample 3, the wetting state should resemble interfacial system 2 (IS2) more than interfacial system 1 (IS1). Namely, droplets should wet the entire surface. By using Equation (26), water droplets are expected to sit on top of the micropillars when using hybrid surfaces with spacing ratio below 2 (Samples 1 and 2), but the liquid should fill the gaps of the hybrid surface when the spacing ratio is equal to 2 (Sample 3).

However, when droplets gently impinge on Sample 3, the wetting behavior closely follows interfacial system 1 as shown in Figure 22 (c). Notice that for Sample 3, the measured equilibrium contact angle is close to the calculated critical angle (θ_{critical}), which suggests that impinged droplets could be in a metastable state [91]. In a metastable state, droplets could spontaneously fall into the substrate cavities to reach a lower energy state [91, 92]. To validate the notion that a metastable state droplet could spontaneously transition to a lower energy state, a droplet was deposited on Sample 3 at ambient conditions as shown in Figure 23. After few seconds, it was observed using a microscope that the droplet transitioned from IS1 to IS2. Figure 23 validates the applicability of Equation (26) in predicting the final wetting state of a droplet on a hybrid surface.

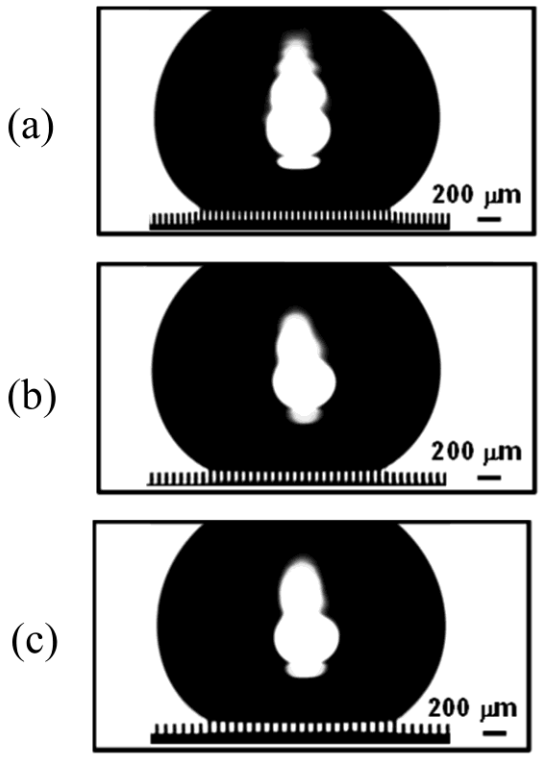

Figure 22. Contact angle measurements using a 9 μl water droplet on hybrid surfaces with equilibrium contact angles of (a) 146° (25 μm micropillar spacing), (b) 148° (37.5 μm micropillar spacing), and (c) 151° (50 μm micropillar spacing)

Table 6. Critical angles for various dimensions of hybrid surfaces

Sample	a (μm)	b (μm)	h (μm)	Critical Angles (˚) (Eq.(19))
1	22.8	24	75	101
2	23.2	38	75	108
3	24.6	49	75	113

a: micropillar width, b: gap size, h: micropillar height

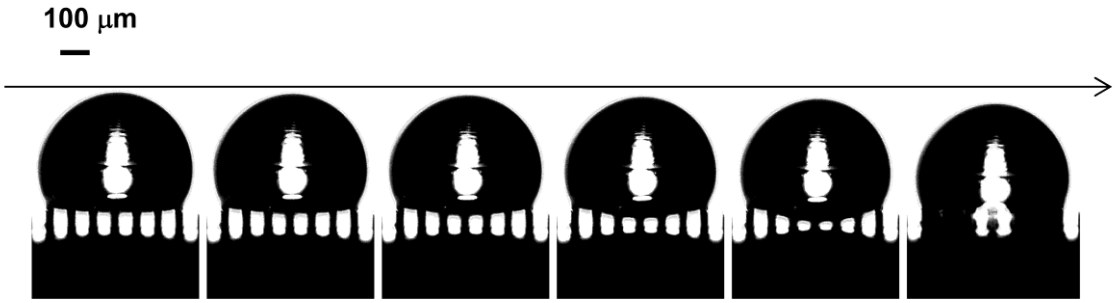

(a) t = 0 sec (b) t = 2 sec (c) t = 4 sec (d) t = 6 sec (e) t = 8 sec (f) t = 9 sec

Figure 23. Sequence images of the transition from interfacial system 1 to interfacial system 2 on Sample 3 (50 μm micropillar spacing hybrid surface)

When conducting condensation experiments using Samples 1 and 2, tiny droplets were observed to nucleate and form on the tops and sides of the micropillars, and on the bottom of each sample as shown in Figure 24a and 24e (nucleation stage). Droplets located at the top of the micropillars continued to grow in size and coalesced with neighboring droplets, resulting in the larger spherical droplets shown in Figure 24b and 24f (coalescence stage).

After coalescence, droplets popped up to the top surface, forming liquid bridges as shown in Figure 24c and 24g (pop-up stage). Subsequent droplet coalescence continued to take place, resulting in the formation of large droplets with diameter size exceeding 100 μm as seen in Figure 24d and 24h (large droplet stage). When condensation was observed in Sample 3, the initial droplet nucleation behavior (Figure 24i) was similar to the other hybrid surfaces. In contrast to the condensation behavior observed in Samples 1 and 2, Sample 3 depicted a different behavior after initial droplet coalescence took place (Figure 24j). As condensation proceeded, coalescence led to the formation of a thin liquid film as seen in Figure 24k (surface minimization stage). The thin liquid film pulled the droplets sitting on top of the micropillars into it to achieve a lower energy state. This process triggered a cleaning effect of the top surfaces of the micropillars, which led to a renucleation of droplets at the surface as seen in Figure 24l (dropwise and filmwise condensation stage).

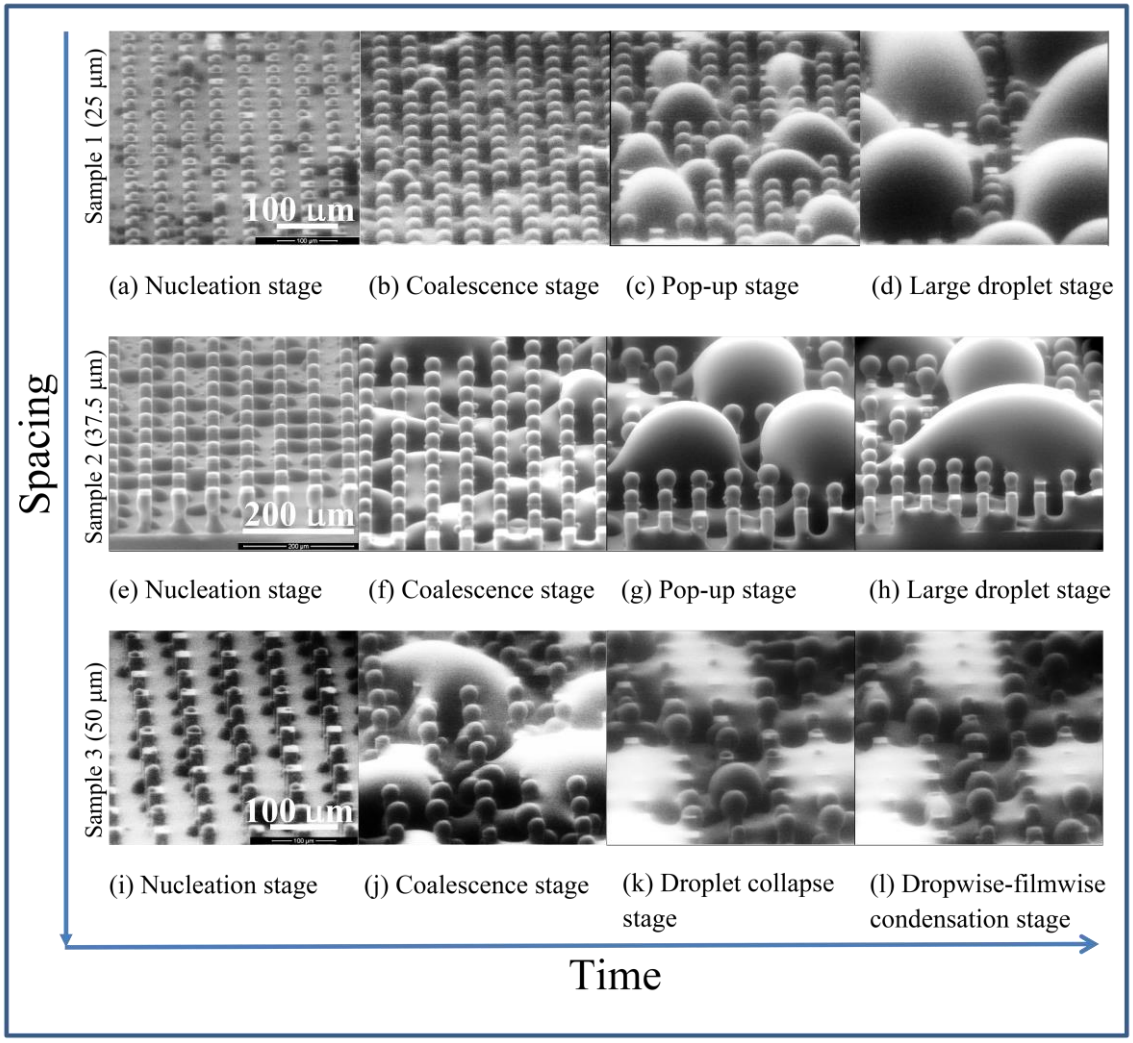

Figure 24. Environmental scanning electron microscopy (ESEM) time-sequence images of water droplets during the growing and coalescence stages on hybrid surfaces

In order to further evaluate the condensation wetting behavior using hybrid surfaces, a condensation cell and an optical microscope were used at ambient conditions. Figures 25 and 26 depict time-sequence images of surfaces supporting droplet condensation (top-view). The condensation experiments were conducted over an hour on all hybrid surfaces. For the 25 μm- and 37.5 μm-spacing hybrid surfaces, the wetting behavior corresponds fairly well with the dropwise condensation process observed using the ESEM. The surfaces depict an identifiable nucleation stage (Figure 25a), droplet growth stage (Figure 25b), coalescence stage (Figure 25c), and large droplet stage (Figure 25d). Similar condensation activity was observed on the hybrid surface when testing Sample 1 (25 μm spacing).

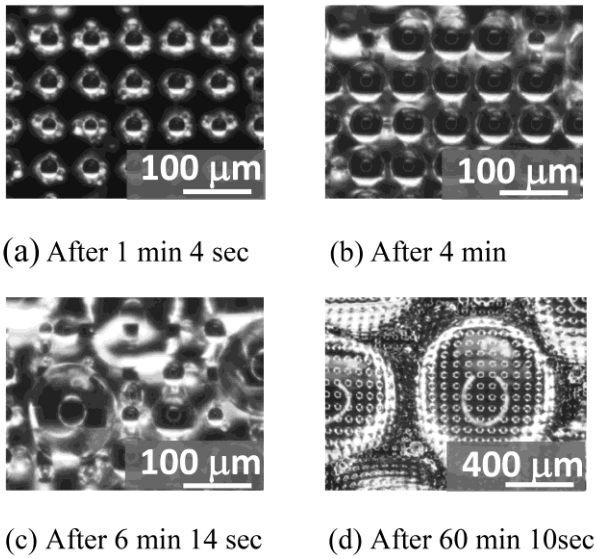

(a) After 1 min 4 sec (b) After 4 min

(c) After 6 min 14 sec (d) After 60 min 10sec

Figure 25. (a-d) Sequential micrographs of condensation process on 37.5 μm-spacing hybrid surface

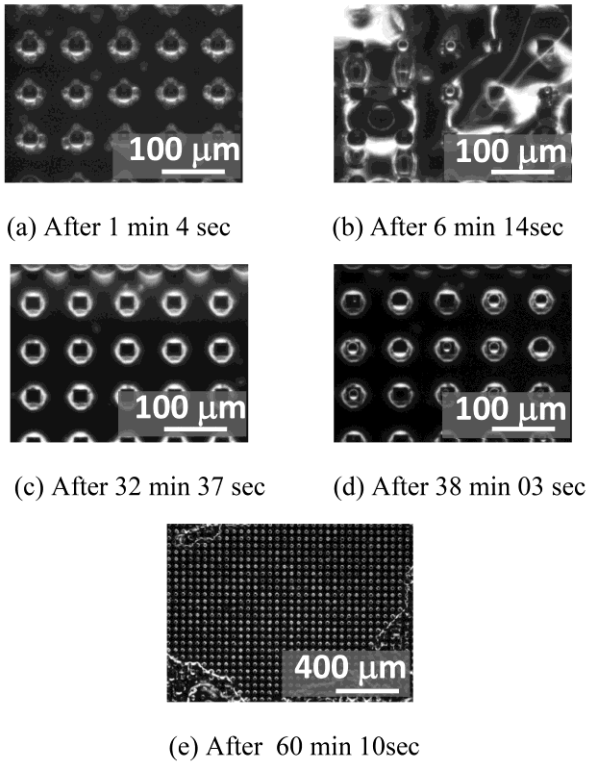

Figure 26. (a-e) Sequential micrographs of condensation process on the 50 μm-spacing hybrid surface

For the 50 μm-spacing hybrid surface, the condensation activity also compares fairly well with the dropwise and filmwise condensation processes observed using the ESEM. The surfaces depict several condensation stages (or phases), including the nucleation stage (Figure 26a), coalescence stage (Figure 26b), Droplet collapse stage (Figure 26c), and the dropwise-filmwise condensation stage (Figure 26d and 26e). Even though it is challenging to visualize the formation of a thin liquid film when viewing Figure 26c and 26d, Figure 24k and 24l clearly depict filmwise condensation behavior when using the 50 μm-spacing hybrid surface. Figure 26e shows a large portion of the thin liquid film demarcated by its own triple contact line (TCL). The condensation activity depicted in

Figure 24 and Figure 26 contributed directly to a continuous process of droplet coalescence, departure and renucleation.

The occurrence and wetting characteristics of dropwise and filmwise condensation observed on Sample 3 are similar to a proposed wetting behavior called *hemi-wicking* [93], which is the intermediate condition between spreading and imbibition as wetting mechanisms. In hemi-wicking [93], the liquid fully penetrates the texture of the engineered surface, leaving no droplets on the top side of the micropillars. Condensation surfaces exhibiting the hemi-wicking condition are characterized by hydrophilic spikes. However, in hybrid surfaces, the sides of the micropillars are hydrophobic in nature (Sample 3) but the droplets still collapse vertically around them and coalesce with other droplets resulting in a cleaning effect of the top hydrophilic site (Figure 26c).

As the spacing ratio *b/a* of the micropillars increases, hydrophobicity of hybrid surfaces also increases [81]. Sample 3 with a micropillar spacing of 50 μm can be regarded as a superhydrophobic surface since its contact angle is over 150°. However, during the condensation process, droplets fill the cavities while simultaneously sitting on top of the hydrophilic sites. This wetting behavior is not like the behavior of impinged droplets which conforms entirely to either to the Wenzel or Cassie-Baxter theories. The observed condensation behavior highlights the importance of the droplet surface-minimization phenomenon during the surface-wetting process.

5.3. Droplet Growth, Coalescence and Sliding Motion during Condensation on Engineered Surfaces

Several condensation experiments were performed to understand the effects of surface morphology and chemistry on condensation dynamics. The contact and sliding angles for all engineered surfaces used in the study are listed in Table 7. Dimensions of selected hybrid surfaces are listed in Table 8. During the condensation experiments using various engineered surfaces, tiny droplets were observed to nucleate and form on top of the surfaces during a period of time (~30 sec) as shown in Fig. 27. During the first 30 sec of the condensation process, droplets nucleated and grew without any of the droplets coalescencing with their neighboring droplets. Fig. 28 shows the percentage of surface area covered by condensed droplets as a function of time based on the images depicted in Fig. 27. The percentage of surface area covered by the condensed droplets is defined as follows:

$$Surface\ Coverage = \left(\frac{A_{projected}}{A_{total}} \right) \cdot 100\% \tag{27}$$

where $A_{projected}$ and A_{total} correspond to the total contact area between the droplets and the surface, and the total area of the surface under condensation conditions, respectively. The areas were calculated by the ImageJ software as explained above.

In general, the droplet surface coverage increases with time for all surfaces, but the condensation dynamics or condensation rates were slightly different for each surface. As it can be seen in Fig. 28, droplet surface coverage was the highest on the silicon surface at 30 sec, which can be attributed to the hydrophilic nature of the surface. For all the surfaces, the surface coverage increases monotonically with time. After 120 sec, the droplet surface coverage was large enough for droplets to frequently coalesce on all surfaces excluding the hybrid surfaces which are characterized by keeping droplets in place due to the strong pinning effect [81, 90]. That is, droplet coalescence has a significant influence on the percentage of area covered by the droplets. In the case of the silicon surface, the coverage reached higher values due to the lack of mobilization of the large merged droplets. For the PTFE and SAMs surfaces, the surface coverage increased and decreased slowly since droplets grew usually by coalescence with adjacent droplets. In the case of Hybrid Surfaces 1 and 2, tiny droplets grew to certain sizes on the micropillars without experiencing any significant coalescence due in part to the relatively large spacing that separated the hydrophilic sites. In summary, Fig. 28 shows how surface features affect the nucleation and growth process of droplets during condensation.

Table 7. Droplet contact angles for engineered surfaces

Sample	Static Contact Angles (˚)	Sliding Angles (˚)	Morphology
Superhydrophobic surface	166.7	< 2	Nano-textured
Hybrid Surface 1	148	27.1	Micro-textured
Hybrid Surface 2	151	23.5	Micro-textured
PTFE surface	117.7	18.1	Flat
SAMs surface	105.5	57.8	Flat
Silicon surface	36.6	65.2	Flat

Table 8. Various dimensions of hybrid surfaces

Sample	a (μm)	b (μm)	h (μm)	b/a
Hybrid Surface 1	23.2	38	75	1.64
Hybrid Surface 2	24.6	49	75	2.0

a: micropillar width, b: gap size, h: micropillar height

The condensation process on the nanoparticle-based hydrophobic surface is quite unique since it is characterized by the self-removal of droplets as shown in Fig. 29. In Fig.29, it is evident that merged droplets appeared to spontaneously depart from the surface through either the out-of-plane jumping motion (Fig. 29a, 29b) or through

random sweeping (Fig. 29c). This spontaneous self-removal of droplets is triggered by droplet coalescence, which takes place when the released surface energy is converted into kinetic energy [7, 11]. Boreyko and Chen et al. [7] developed a relatively simple model that can be used to estimate the velocity of jumping droplets based on the complete transformation of surface energy to kinetic. The model is as follows:

$$V \propto \sqrt{\frac{\sigma}{\rho \cdot r}} \tag{28}$$

where V is the velocity of droplet, σ is the surface tension, ρ is the density, and r is the radius of droplet.

From Fig. 28, it is evident that the nanoparticle-based hydrophobic surface maintained the lowest surface coverage after 120 sec, which can be explained by the self-removal droplet mechanism.

When estimating the surface coverage as a function of static contact angle at 240 sec, an almost linear relationship between the two parameters can be found as seen in Fig 30. In summary, the surface coverage decreases with an increase in static contact angle. The highest surface coverage value was found on the silicon surface which had the lowest static contact angle. The silicon surface also had the largest sliding angle as shown above in Table 7. That is, easily-wetted hydrophilic surfaces characterized by having poor droplet mobility results in the highest surface coverage. In contrast, the nanoparticle-

based hydrophobic surface depicts the highest static contact angle and rapid droplet motion which contribute to the lowest percentage of surface coverage.

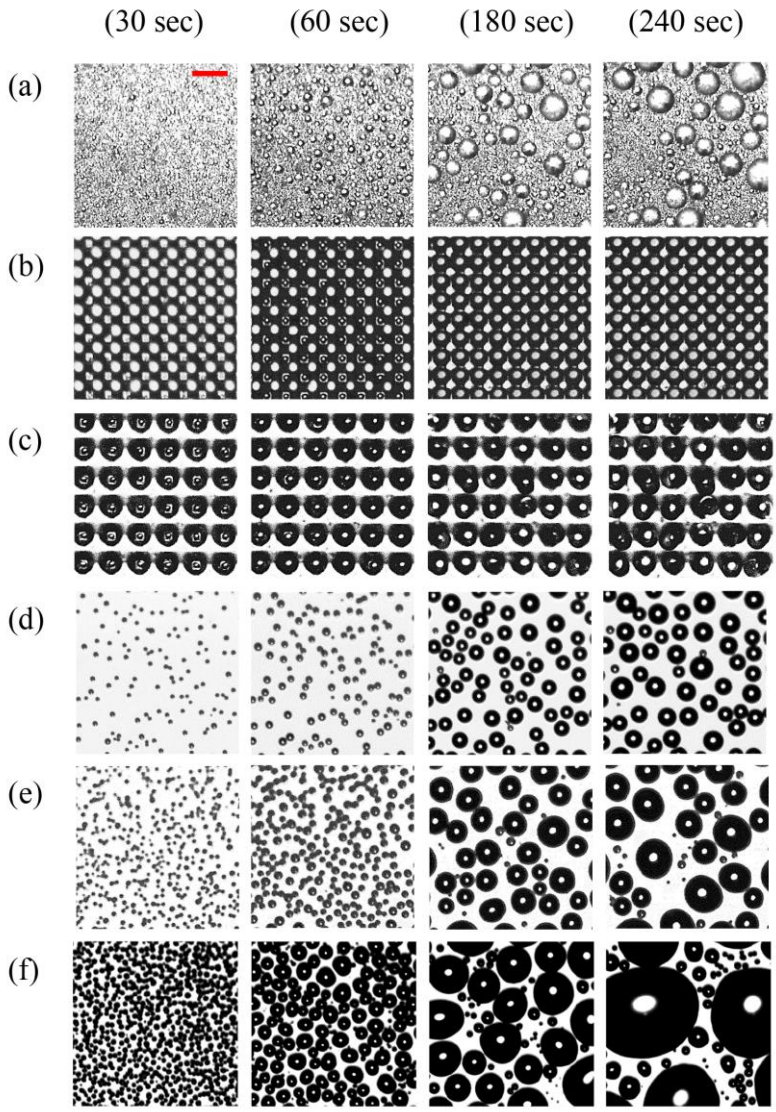

Figure 27. Time-sequenced condensation behavior of water on (a) nanoparticle-based hydrophobic surface, (b) hybrid Surface 1, (c) hybrid Surface 2, (d) PTFE surface, (e) SAMs surface and (f) silicon surface. The scale bar is 100 μm

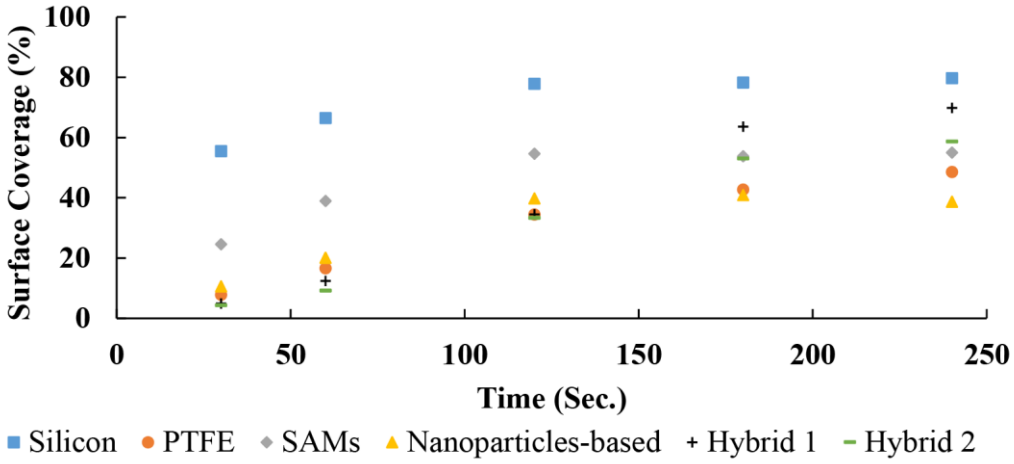

Figure 28. The experimentally measured surface coverage (%) as a function of time during condensation on engineered surfaces

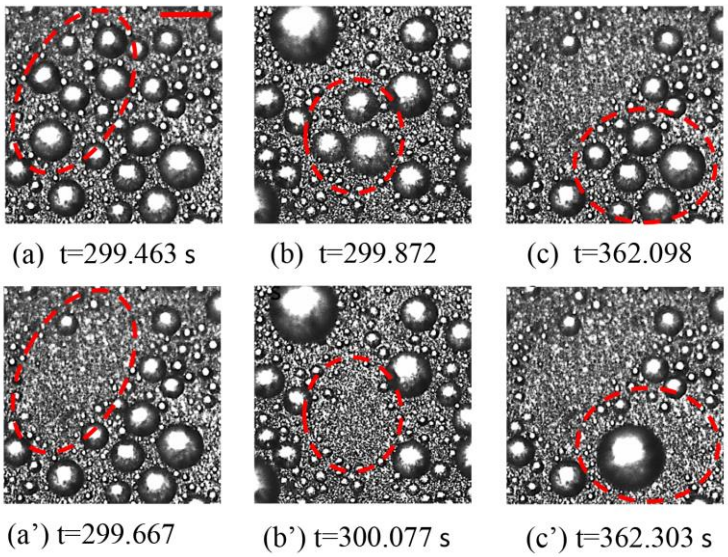

Figure 29. Time-lapse condensation images on the nanoparticles-based hydrophobic surface. The spontaneous motion of condensate droplets are observed when condensed droplets coalesce with neighboring droplets, which leads to either to out-of-plane jumping motion (a to a' and b to b') or a random sweeping motion (c to c'). The scale bar is 100 μm

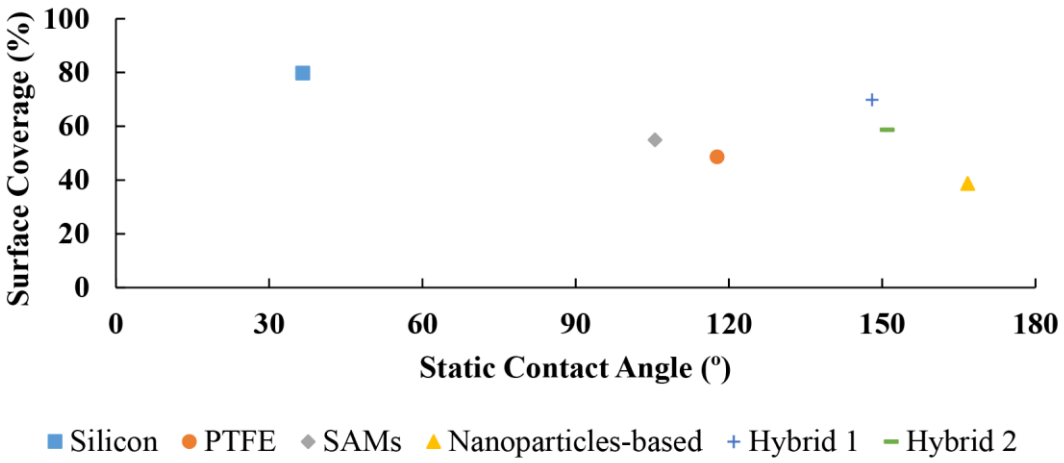

Figure 30. Surface coverage (%) as a function of the static contact angle during condensation on engineered surfaces at 240 sec

Fig. 31 shows the condensation pattern occurring on all test surfaces when they are vertically aligned. During a two hour experiment, gravity seems to be the main driving transport mechanisms in the removal of condensed droplets from the surfaces. In general, condensate droplets tend to grow to a large size (~2 mm) until they roll off the surface by gravity [10, 34]. Fig. 31a shows a good number of medium-sized droplets on the nanoparticle-based hydrophobic surface even though the surface is supposed to have the best droplet shedding mechanism among all the specimens. One possible explanation can be attributed to sideway droplet mobility and droplet coalescence which resulted in the formation of larger droplets. It is well known that relatively large droplets cannot fully experience out-of-plane jumping motion given their size [53, 94]. Furthermore, it appears that the droplets on that type of surface could not be shed due to gravity alone. For Hybrid Surface 1, a significant contact angle hysteresis effect has been reported, which is caused by the edge effect that arises from the hydrophobic

micropillars edges and hydrophilic tips [81], which leads to highly pinned droplets as shown in Fig. 31b. For Hybrid Surface 2, a combination of dropwise and filmwise condensation mechanisms which are similar to the hemi-wicking behavior [90] can be observed in Fig. 31c which leads to poor droplet removal. In the case of the PTFE surface, Fig. 31d shows that small sliding droplets swept and coalesced with other droplets along the rolling path. This can be attributed to the inherent low sliding angle of the droplets on that surface. For the SAMs surface and silicon surface, the droplets rolled off the surface driven mainly by gravity after they grew and coalesced to a certain size (Fig. 31e, 31f).

In summary, various engineered surfaces have been fabricated, and the effects of surface wettability on dew condensation have been investigated. Droplet wettability, and two different condensation behaviors on hybrid surfaces are also reported. In the early stages of condensation, the static contact angles and sliding angles have a markedly effect on droplet growth and coalescence on the surfaces. Also, the spontaneous motion of droplets on the nanoparticle-based hydrophobic surface leads to the lowest surface coverage. Furthermore, experimental results reveal that droplet sliding angles can have an important effect on droplet sliding motion. Specifically, the PTFE surface is characterized by having a low sliding angle which leads to frequent droplet roll off from the surface, which have the potential to enhance condensation.

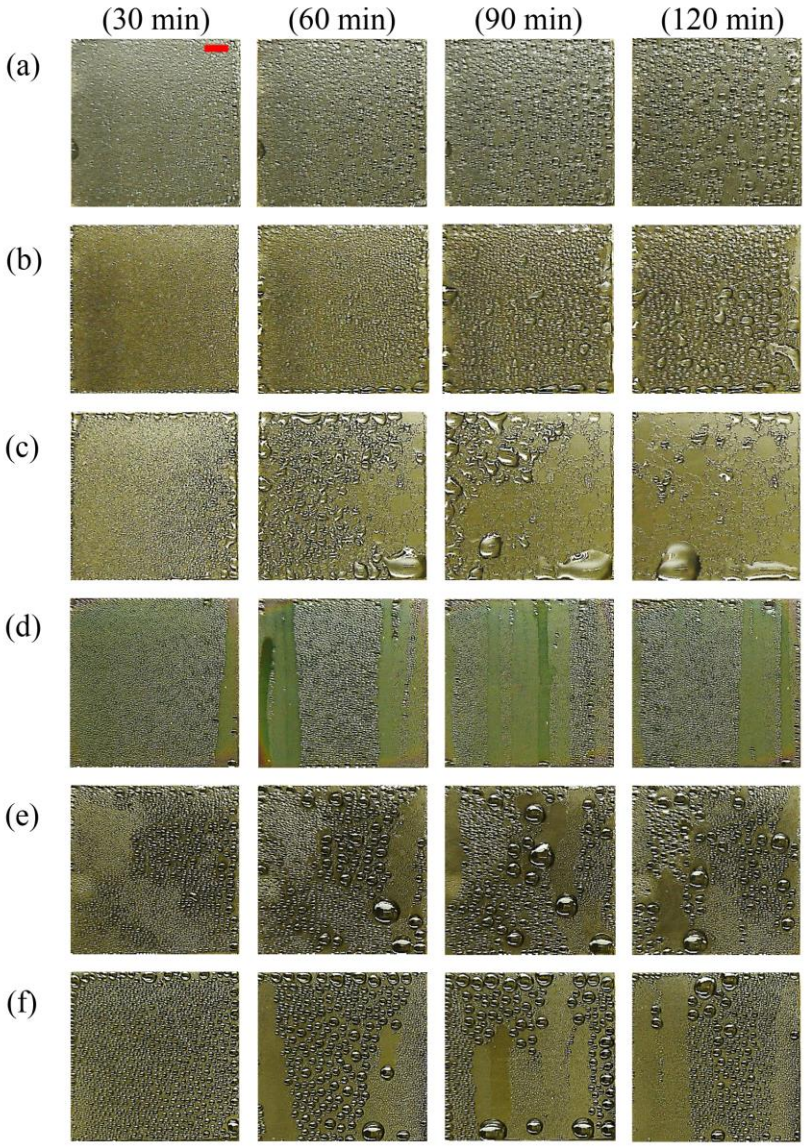

Figure 31. Time-sequenced condensation behavior of water on (a) nanoparticle-based hydrophobic surface, (b) hybrid Surface 1, (c) hybrid Surface 2, (d) PTFE surface, (e) SAMs surface and (f) silicon surface. The scale bar is 4 mm. All surfaces are vertically aligned

CHAPTER VI

DEW CONDENSATION HEAT TRANSFER EXPERIMENTS

The results presented in the previous chapter suggest that the combined effects of surface morphology and wetting properties have effects on the dynamics of condensation on engineered surfaces. In this chapter, the result of dew condensation experiments are presented to understand how condensation heat transfer is affected by surface properties under controlled conditions. The result indicate that heat transfer performance on engineered surfaces depended strongly on surface morphology and wetting properties. For the selected engineered surfaces, heat transfer coefficient correlations have been postulated and data fitted taking into account ambient temperature-to-surface (T_{amb}-T_s) difference and laminar flow conditions (300<Re<770). In addition, surface temperature data obtained using an advanced IR imaging system have been analyzed to determine the effects of the surface features on droplet growth dynamics, especially during the nucleation and droplet coalescence phases of dropwise condensation.

6.1. Heat Transfer Performance of Engineered Surfaces

Several heat transfer experiments were conducted to evaluate the effectiveness of all the surfaces during condensation. Heat transfer measurements were made by maintaining constant relative humidity of moist-air (ϕ=80%) at constant air velocity (V=0.3 m/s). The Reynolds number was set at 454 to ensure laminar airflow conditions. Data analysis in this work was based on the measurements obtained from a thin-film heat flux sensor integrated into the custom-made cooling cell. The average heat transfer coefficient, have was obtained as follows:

$$h_{ave} = \frac{q''}{(T_{air} - T_s)} \tag{29}$$

where T_{air} is the moist air temperature, T_s is the averaged surface temperature of substrate, and q" is the overall heat flux. The error table associated with the measurement of *h* can be found in the appendix B.

During the two hours experiments, the condensation heat transfer performance was significantly affected by the droplet sliding motion. From Figure 31 in Chapter V, it was found that droplet roll-off of small droplets occurred more frequently on the PTFE surface as compared to other engineered surfaces under identical conditions. This favorable sliding motion seen on PTFE surface correlates well with the superior condensation performance shown in Figure 32. Specifically, droplet sliding motion on the silicon surface via gravity was also observed as shown in Figure 31 (f). The silicon surface also exhibits fairly good condensation performance as shown in Figure 32. For the SAMs surface, larger droplets were observed to remain pinned on the surface. Furthermore, large droplets were characterized by having high thermal resistance values which led to lower heat transfer performance as seen in Figure 32. The nanoparticle-based (NP) surface exhibited out-of-plane droplet jumping motion but not for a long time, which led to the formation of larger droplets [53]. Therefore, the NP surface did not perform as expected because the larger droplets seen on the surface led to lower heat transfer.

The hybrid surfaces which are characterized by having heterogeneous properties did not result in better heat transfer performance due to the strong pinning effect associated with the hydrophobic edge of the surfaces. In addition, Hybrid Surface 2, which exhibited a combination of dropwise and filmwise condensation mechanisms [10] resulted in a lower heat transfer coefficient than Hybrid Surface 1. The low heat transfer coefficient values can be attributed to the change from dropwise to filmwise condensation mode. The formation of a condensate film increased the heat transfer resistances which inhibit heat transfer on Hybrid Surface 2.

In summary, experimental results revealed that droplet sliding does have an important effect on heat transfer performance. Specifically, the PTFE surface exhibited superior heat transfer performance since droplets could easily shed and did not grow as much as in the other engineered surfaces.

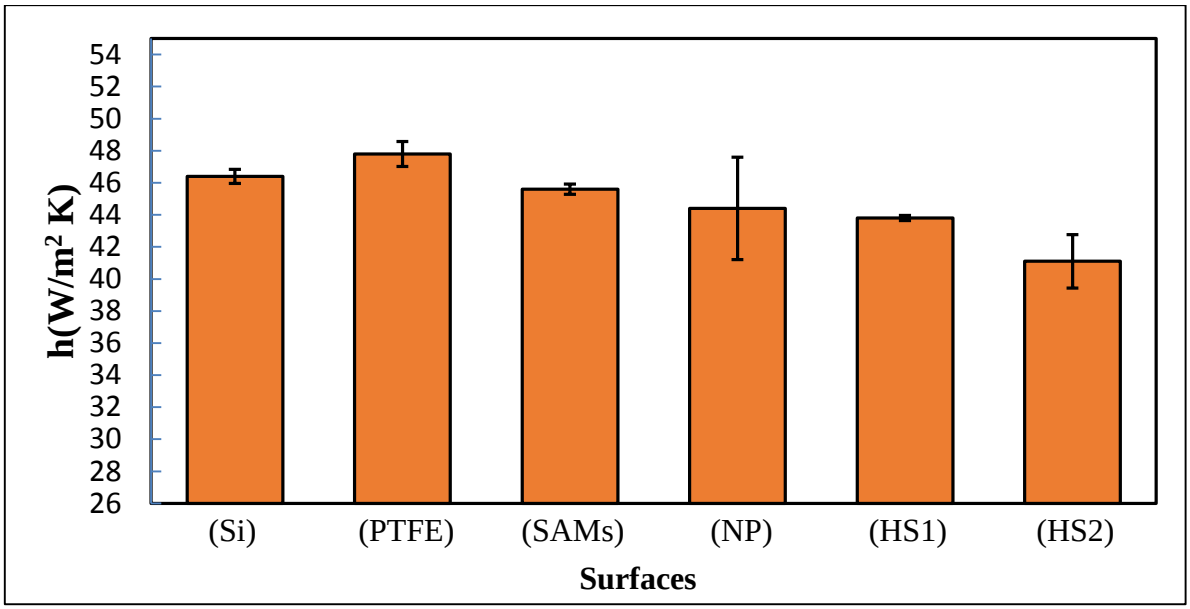

Figure 32. Condensation heat transfer performance of engineered surfaces: (a) silicon surface (Si), (b) PTFE, (c) SAMs, (d) nanoparticle-based (NP) surface, (e) hybrid surface 1 (HS1), (f) hybrid surface 2 (HS2). Error bars denote standard deviation of calculated *h* values

6.2. Dew Condensation Heat Transfer Empirical Correlations

In order to experimentally study the heat transfer process using engineered surfaces during dew condensation, heat transfer coefficient correlations as a function of independent factors such as condensing and air temperature difference and Reynolds number were postulated and fitted using experimental data. As discussed above, PTFE and silicon surface exhibited better heat transfer performance. Nanoparticle-based surface showed unique spontaneous droplet motion which could have an effect on heat transfer. Therefore, the three surfaces were selected in the development of empirical correlation. For all tests, environmental parameters such as air velocity and surface cooling temperature were control independently. During the first 30 minutes of each

experiment, heat transfer measurements were made considering four different air velocity values and four condensing and air temperature differences. For comparison purposes, experiments were also conducted under low relative humidity conditions.

The effects of both condensing and air temperature difference and air velocity on the heat transfer performance are shown in Fig. 33-35. It can be seen that the heat transfer coefficients for dew condensation was always greater than for the dry air cases. The difference in heat transfer coefficient is directly attributed to the condensation of droplets that provided significant latent heat transfer under dew condensation conditions. Fig. 33-35 also show that the heat transfer coefficient depends strongly on Reynolds number but slightly on the condensing and air temperature difference. The results were consistent with the similar trend observed by Nagai et al. [69] and Yoav et al. [73]. Although the temperature difference is the main driving force for condensation, dew condensation resulted in the production of small quantities of water given the limited temperature range used in the study.

The effects of air velocity (Reynolds number) on the heat transfer performance are shown in Fig. 36-38. As it can be seen, the heat transfer coefficients increases linearly with air velocity or higher Reynolds number. Furthermore, a larger mass of moisture flowed across the engineered surfaces when the air velocity was increased. As a Result, more water molecules approached surfaces which allowed fast nucleation and condensed droplet growth leading to higher latent heat transfer. Furthermore, as more droplets condensed along the engineered surfaces, those surfaces became rough and wavy due to the accumulation of droplets of varying sizes. This in turn favored the formation of

disturbances in the boundary layer which resulted in greater heat transfer over surfaces [95-97] .

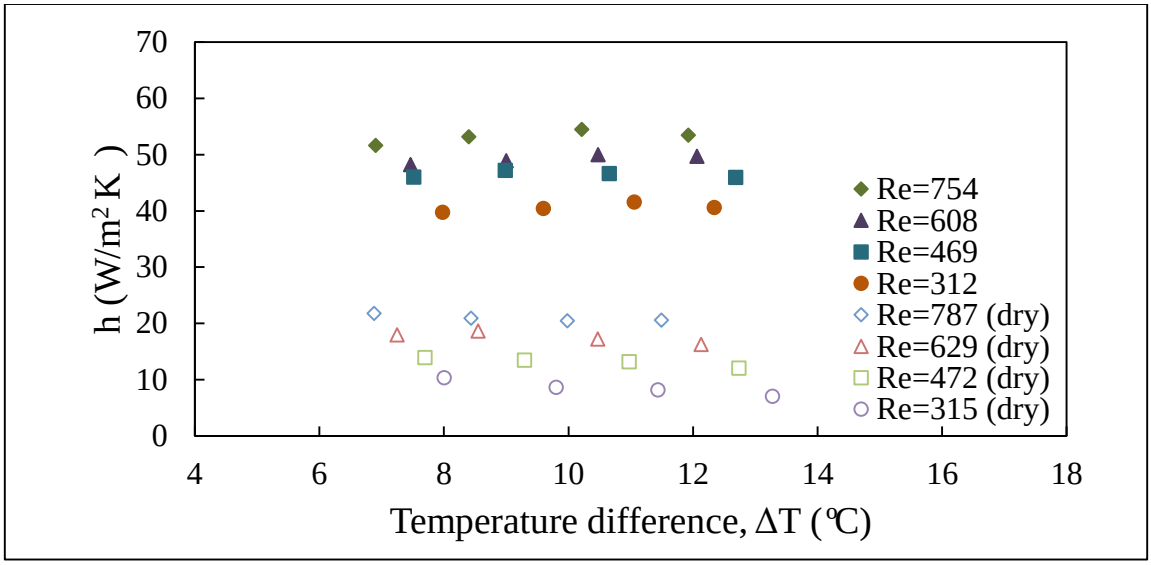

Figure 33. Heat transfer coefficient as function of ambient-surface temperature difference (ΔT) of silicon surface

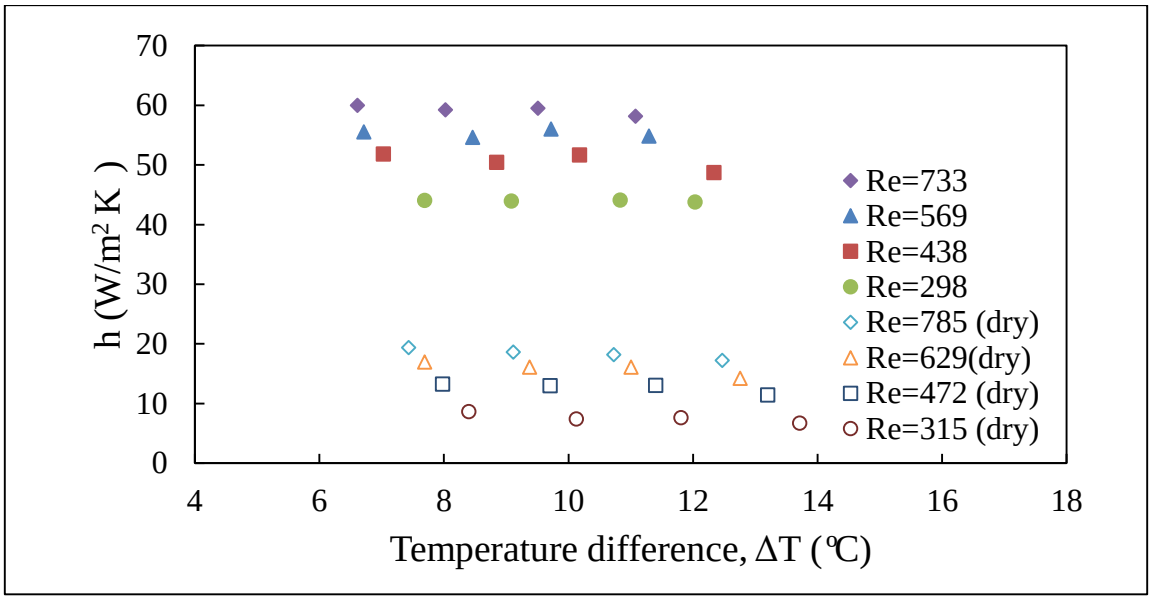

Figure 34. Heat transfer coefficient as function of ambient-surface temperature difference (ΔT) of PTFE surface

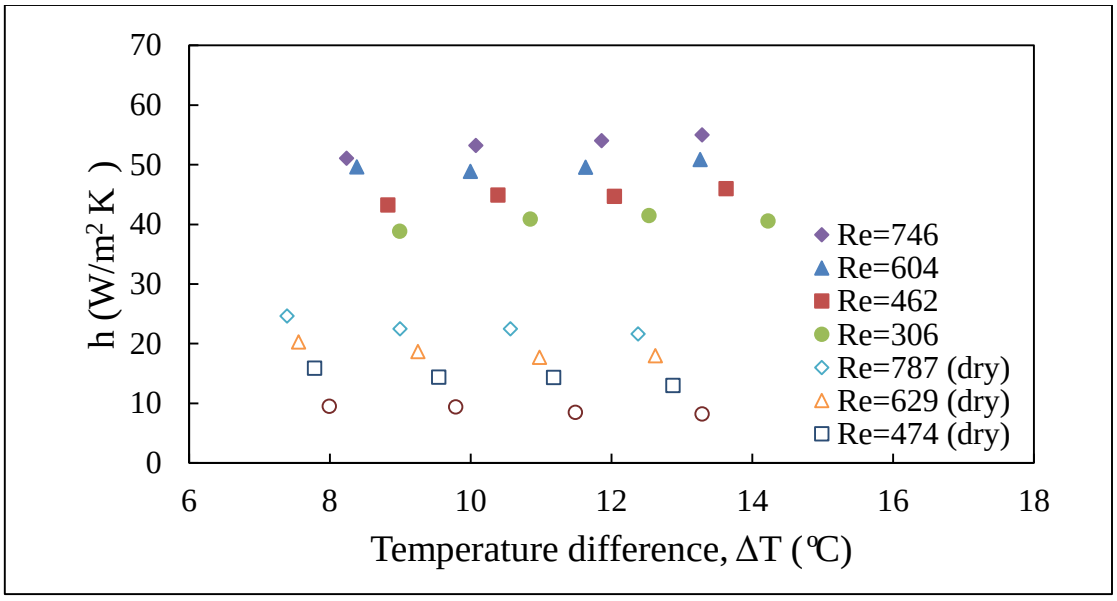

Figure 35. Heat transfer coefficient as function of ambient-surface temperature difference (ΔT) of nano-particle based surface

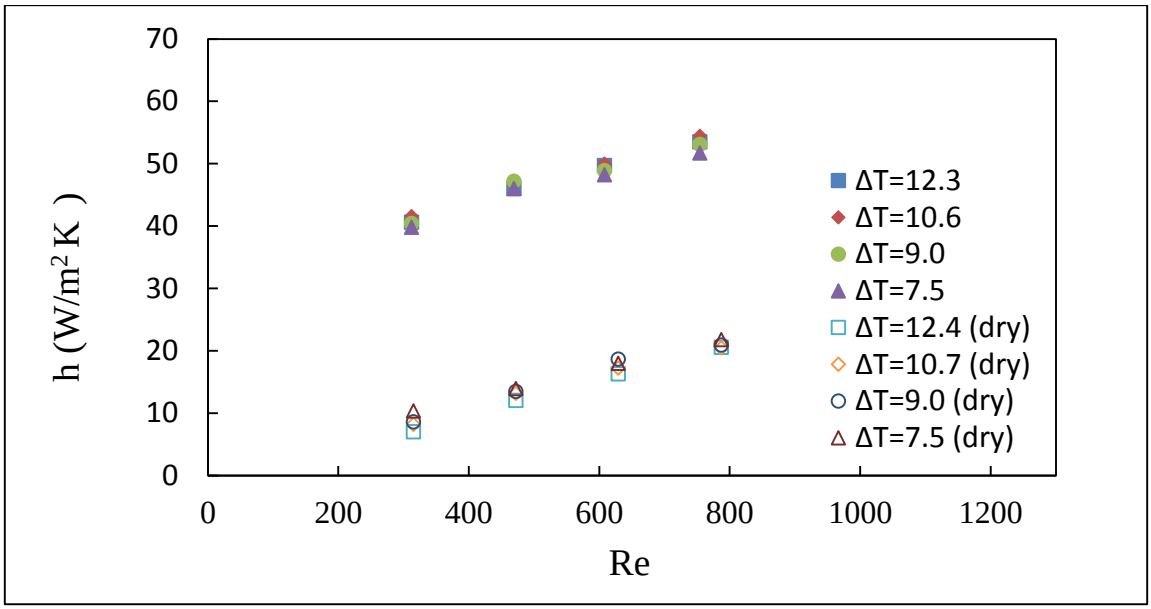

Figure 36. Heat transfer coefficient as function of Reynolds number of silicon surface

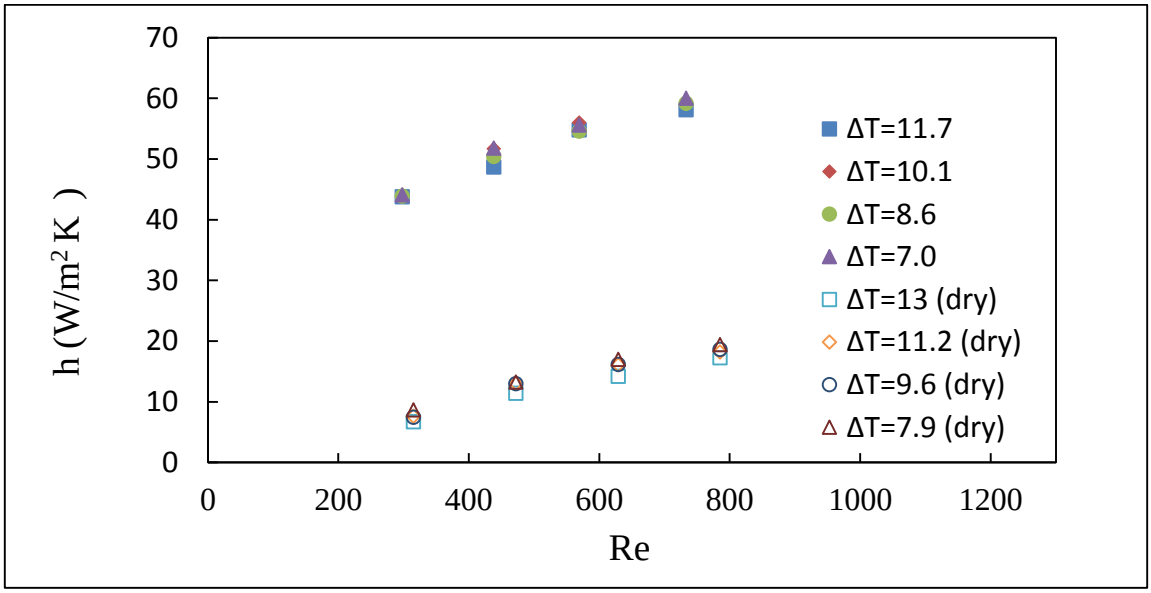

Figure 37. Heat transfer coefficient as function of Reynolds number of PTFE surface

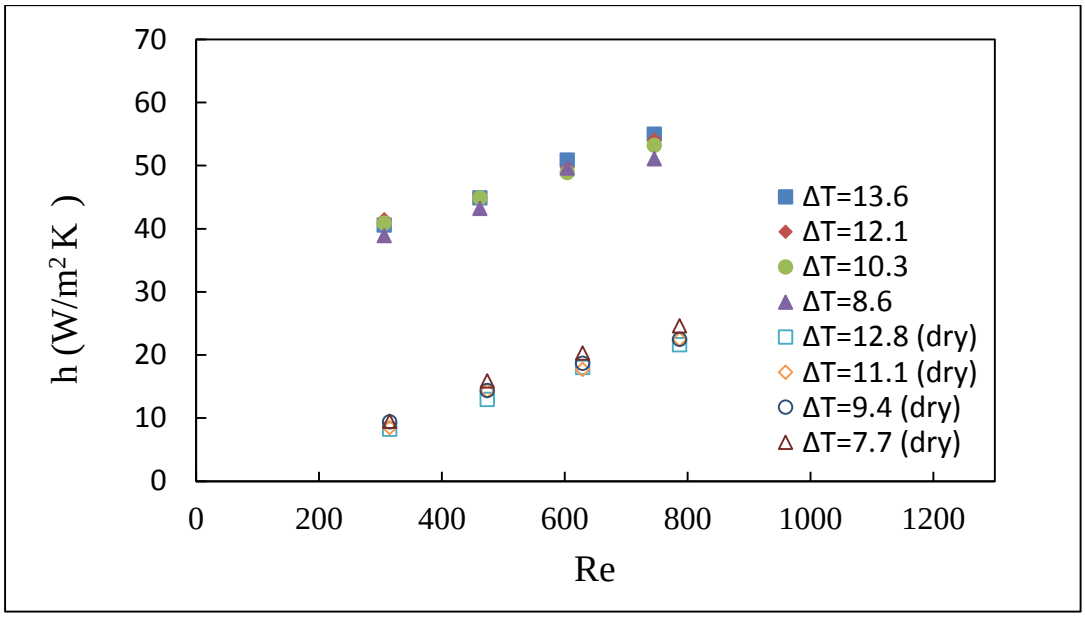

Figure 38. Heat transfer coefficient as function of Reynolds number of nano-particle based surface

Empirical heat transfer correlations were postulated and fitted using experimental data using condensing and air temperature difference and Reynolds number were as independent variables. The convection–condensation heat transfer coefficient correlation for dew condensation was postulated as follows:

$$h = a + (\mathrm{Re})^{b}(\phi_T)^{c} \tag{30}$$

where a, b, and c are determined using experimental data, Re is the Reynolds number, ϕ_T is the non-dimensional temperature difference [73] is defined as follows:

$$\phi_T = \frac{T_d - T_s}{T_{amb} - T_s} \tag{31}$$

where T_d is dew point temperature, T_s is substrate temperature, T_{amb} is ambient temperature .

The heat transfer empirical correlations were fitted using the experimental heat transfer data by the method of least squares. Table 9 shows the values of the empirical constants after fitting the data to the postulated model.

Table 9. Correlation coefficients of engineered surfaces

	a	*b*	*c*	R^2
Silicon surface (Si)	1.993	0.306	0.099	0.98
PTFE surface	1.902	0.328	-0.046	0.98
Nanoparticle-based (NP) surface	1.934	0.320	0.197	0.97

Regression analysis was carried out using 16 data points that included values of condensing and air temperature difference, and Reynolds number. The coefficients were found to fit the experimental results of engineered surfaces as shown in Table 9 above. Fig. 39-41 show the heat transfer coefficient values obtained using the empirical correlation and experimental data for each engineered surface. Table 9 shows all R^2 (coefficient of determination) were above 0.97 which indicates that the postulated

correlations are in excellent agreement with experimental data. The correlation deviated from experimental data by no more than 3.5% in all cases. By using the regression results of all engineered surfaces, it can be concluded that the effect of condensing and air temperature difference on heat transfer performance is much less significant than the effects of air velocity or Reynolds number.

From Table 9 and Equation (30), it can be seen that Reynolds number has a similar effect on heat transfer coefficient regardless of surface. Furthermore, it is evident from Table 9 that the temperature difference has an insignificant effect on heat transfer as illustrated in Fig. 33-35. From the empirical correlations, it is clear that increasing Reynolds number or moist-air velocity would have the greatest effect on heat transfer because it would results in greater availability of moist air flowing over the samples. Furthermore, the NP surface exhibits a stronger dependence on non-dimensional temperature difference when compared to the other two surfaces. This suggests that the off-the-plane jumping motion could be playing a role in terms of heat transfer rate at the surface.

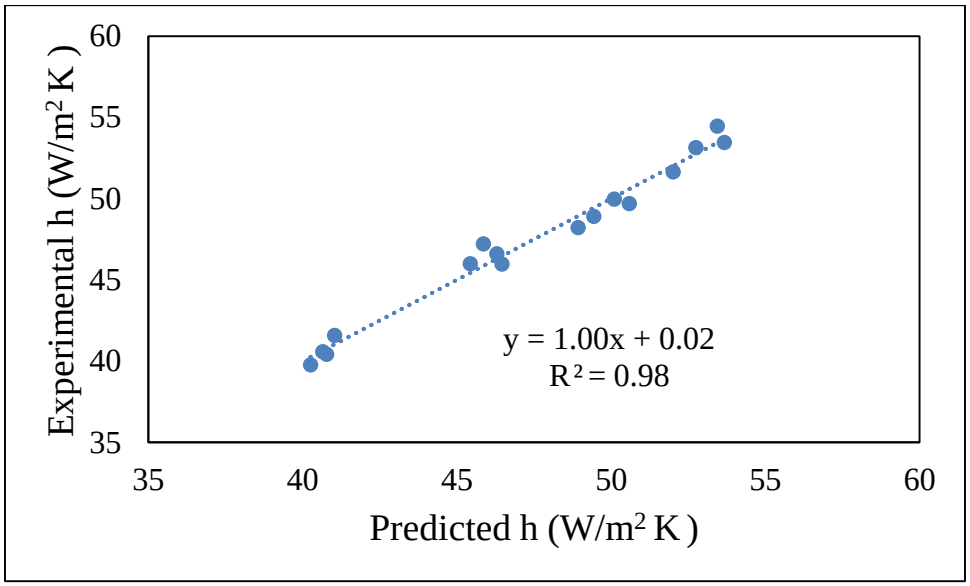

Figure 39. Comparison for an experimental and predicted condensation heat transfer coefficient on silicon surface

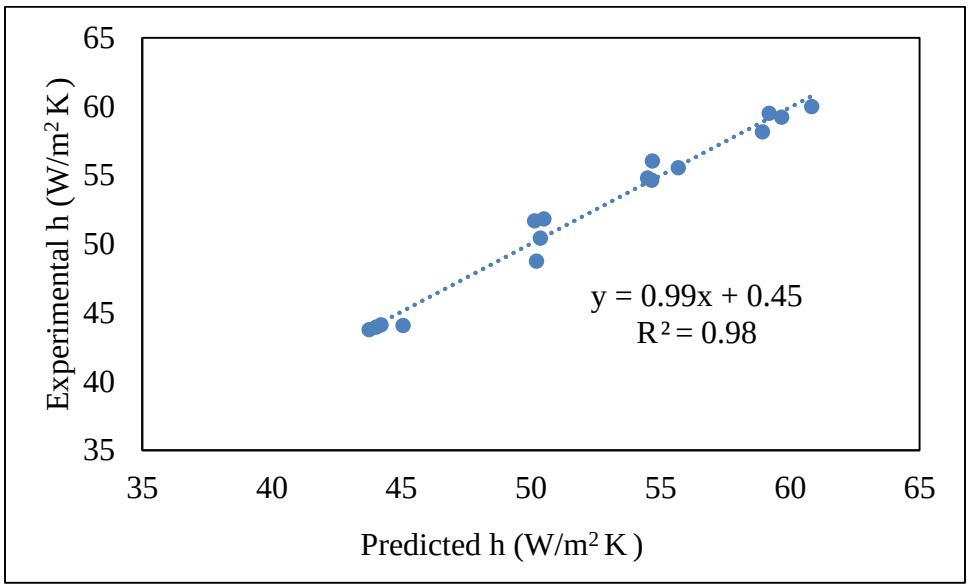

Figure 40. Comparison for an experimental and predicted condensation heat transfer coefficient on PTFE surface

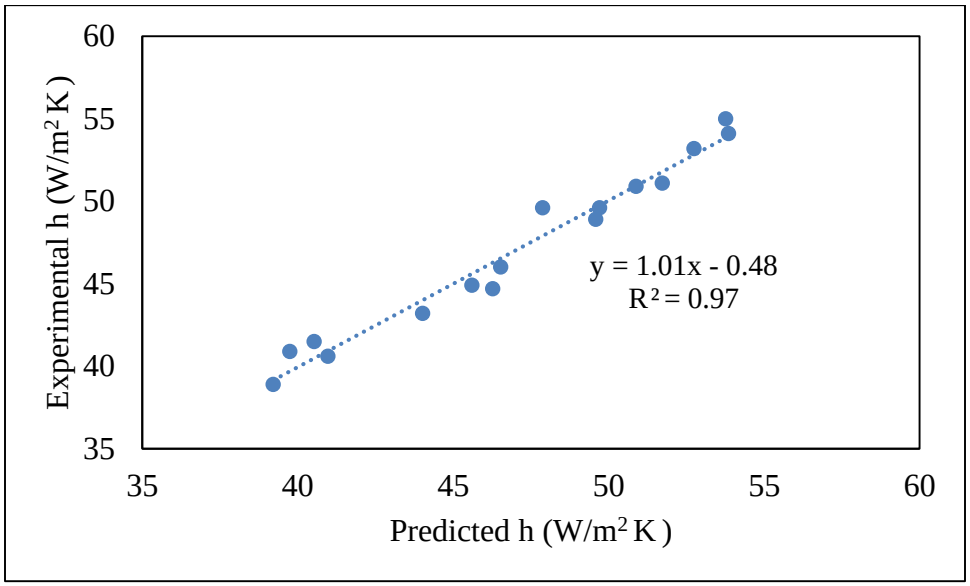

Figure 41. Comparison for an experimental and predicted condensation heat transfer coefficient on nanoparticle–based surface

6.3. IR Surface Temperature Measurement

Nonintrusive sensing of condensed droplets and substrate tepmeratures via IR imaging is advantageous when visualizing condensation on engineered surfaces, where the use of thermocouples on top side surface may not feasible. Nonintrusive thermal measurements of the condensation on engineered surfaces could also reveal important details about condensation dynamics. In this study, the IR image system (FLIR A325) was used to provide real time and continous temperature measurements of the top surface during the condensation process. The infrared camera was positioned above the engineered surfaces and it measured the temperature distribution during condensation experiments for the first ten minutes. The raw infrared data obtained for each experiment was converted from a FLIR proprietary format to a csv-format which was then read by

MATLAB. A custom MATLAB code was created to extract data each surface to calculate the mean temperature and standard deviation of surface temperature.

IR thermography was used to measure surface temperature during the condensation and detect the occurrence or onset of the coalescence dominant stage. The IR camera was focused on top of each surface to be able to measure surface temperature while droplets nucleated and coalesced with other droplets. It is important to note that water is opaque at IR wavelengths and the emissivity of water of 0.96 was used in this study. The initial substrate temperature was ~7 ℃, and all experiments were conducted at high relative humidity (RH 80% at room temperature). Figure 42 shows IR thermal images and highly contrasted IR images of condensation on each engineered surface after ten minutes. As it can be seen in the thermal images, cold water droplets are shown as blue dots clearly. The presence of condensed droplets results in a temperature distribution across each surface. In Figure 43, the effect of droplet location on surface temperature is quite evident. As the figure shows, dry spots on the surface are characterized by slightly higher temperatures. The figure also shows that when droplets grow, the surface temperature at the droplet location decreases substantially. Furthermore, the thermal data suggest that the temperature distribution below the condensate droplet is very uniform. This suggests that marangoni effects may be negligible with droplets of that size.

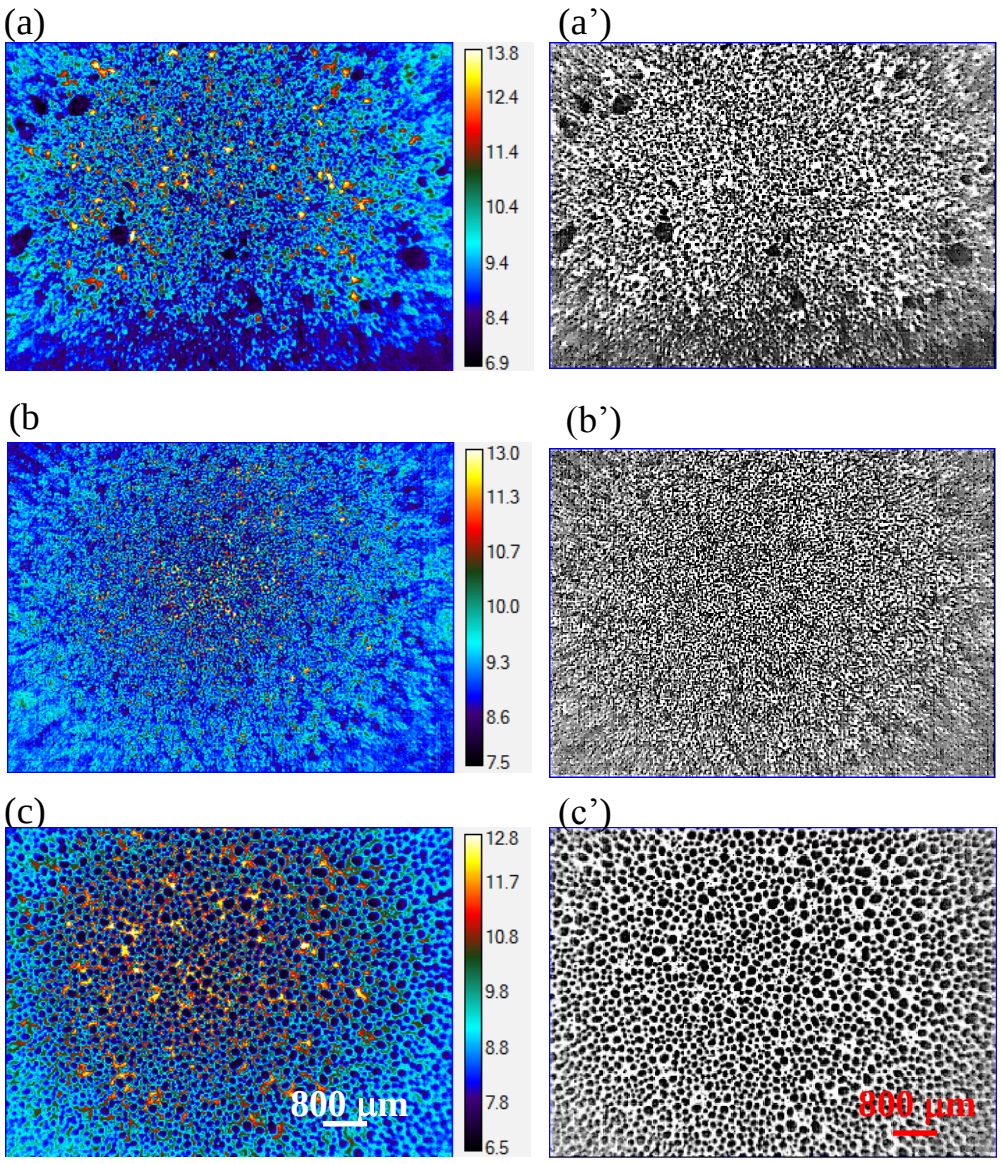

Figure 42. IR thermal images (left) and highly contrasted IR images (right) of droplet condensation on (a) nanoparticle-based surface (b) PTFE surface (c) Si surface

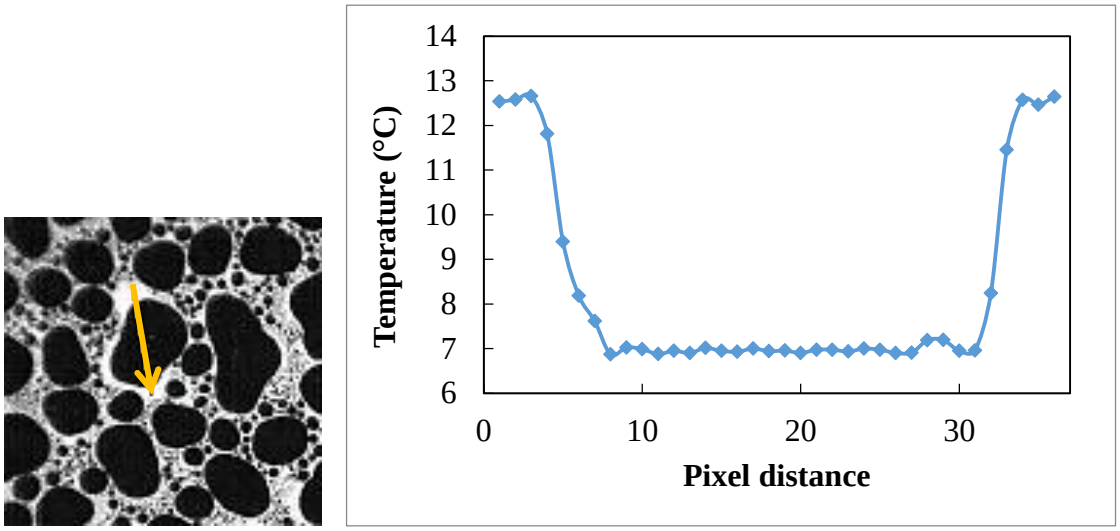

Figure 43. (a) Image of condensed water droplets on Si surface. (b) Temperature profile across a droplet between dry spots

The surface temperature measurements were also conducted using a thermocouple. As shown in Fig 44, the surface temperature reached steady state after two minutes. When using IR system with values of emissivity of water, it can be seen in Fig.45 that the surface temperature obtained using the IR system converges to the temperature values given by the thermocouple. This clearly suggests that both temperature technique are complementary and can be used to understand condensation phenomena at different time scales.

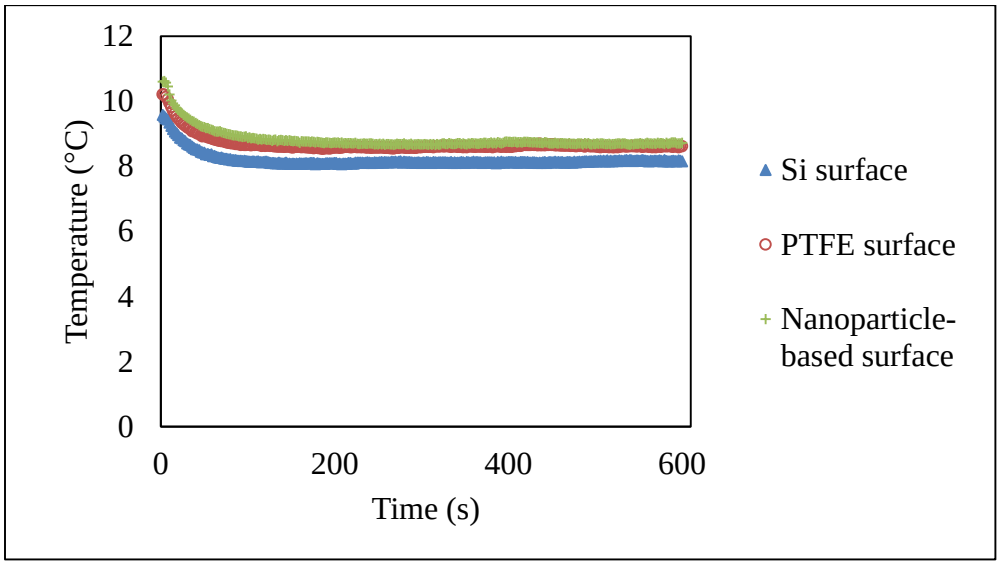

Figure 44. Surface temperature measurement via thermocouple during condensation

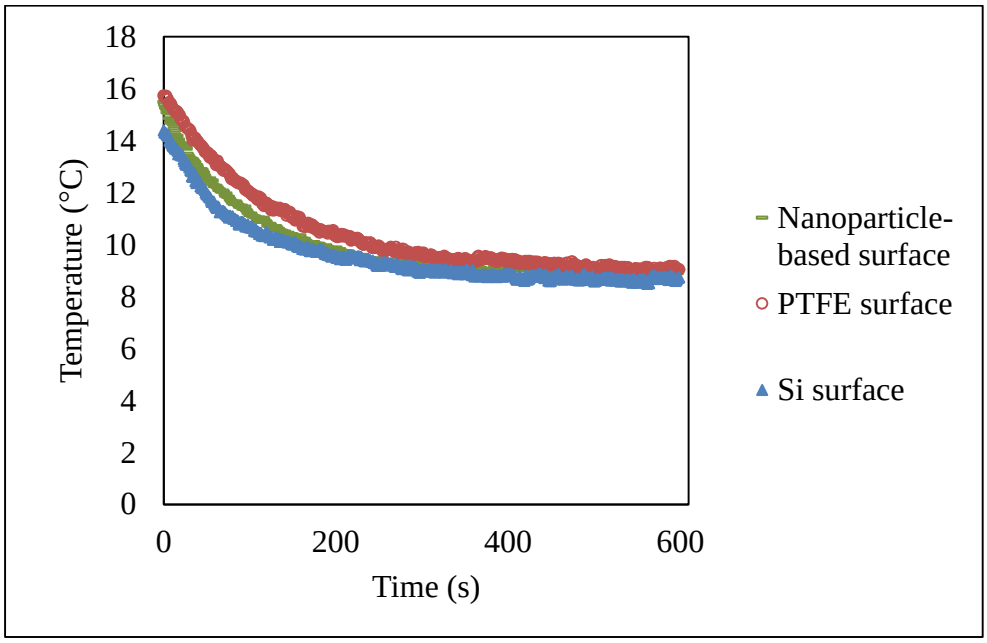

Figure 45. Surface temperature measurement via IR system during condensation

Fig. 46-48 show the standard deviation of surface temperature from each of the engineered surfaces. It can be seen that the standard deviation increases after few minutes of condensation. Fig. 46-48 also show highly contrasted IR images before and after the standard deviation curves reach their minimum values. The minimum standard deviation value can be interpreted as the surface reaching a relatively uniform surface temperature distribution after few minutes of cooling. This suggests the formation and development of a nucleation-dominated phase within the surface. Beyond the minimum standard deviation value, the standard deviation of surface temperature increases monotonically until droplet shedding takes place. Furthermore, once the standard deviation starts increasing, it can be suggested that the condensation phenomena is dominated by droplet coalescence even though nucleation of droplets still occurs. Moreover, experimental observations confirm that the coalescence-dominated stage is characterized by having large droplets, which are not distributed uniformly. Even though the nanoparticle-based surface showed spontaneous droplet motion for small droplets, a good number of larger sized droplets remained and coalesced on it which resulted in non-uniform temperature distribution. As can be seen in Fig. 47, the PTFE surface needed more time for droplets to grow and coalesce frequently due to its hydrophobic nature. On the other hand, the silicon surface exhibits a sharp rise of the standard deviation of surface temperature as it can be seen in Fig. 48. Furthermore, the silicon surface, which is hydrophilic in nature, depicts large coalesced droplets during condensation as it can be seen in Figure 31 as discussed in chapter V. Moreover, the coalescence dominant stage was earlier than other surfaces. It is important to note that

the resolution of camera is 25 μm. Therefore, fine or small temperature distribution due to small droplet movement may not be detectable. Therefore, the actual onset of coalesce dominant stage could happen earlier. In summary, the coalescence dominant stage is affected by surface wettability and condensation dynamics including droplet shedding. Also, the results shown below are useful and can be used to distinguish and compare coalescence dynamics of droplets on engineered surfaces. The results clearly indicate that surface morphology plays an important role in the onset of droplet coalescence and heat transfer behavior at the surface-fluid interface.

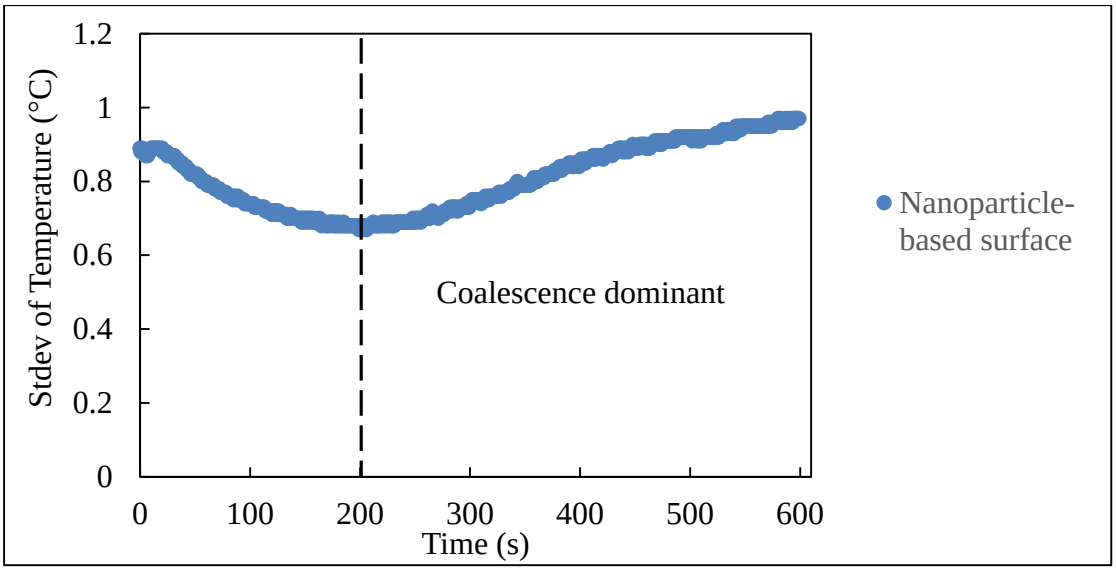

(a)

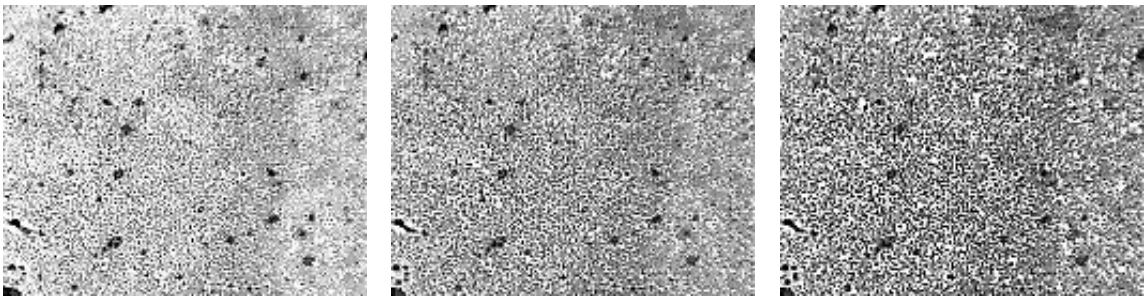

(c) (c) (d)

Figure 46. (a) Standard deviation of surface temperature on nanoparticle–based surface during condensation, highly contrasted IR images of condensed water droplets on nanoparticle–based surface at (b) 144 sec (c) 204 sec (onset) (d) 264 sec

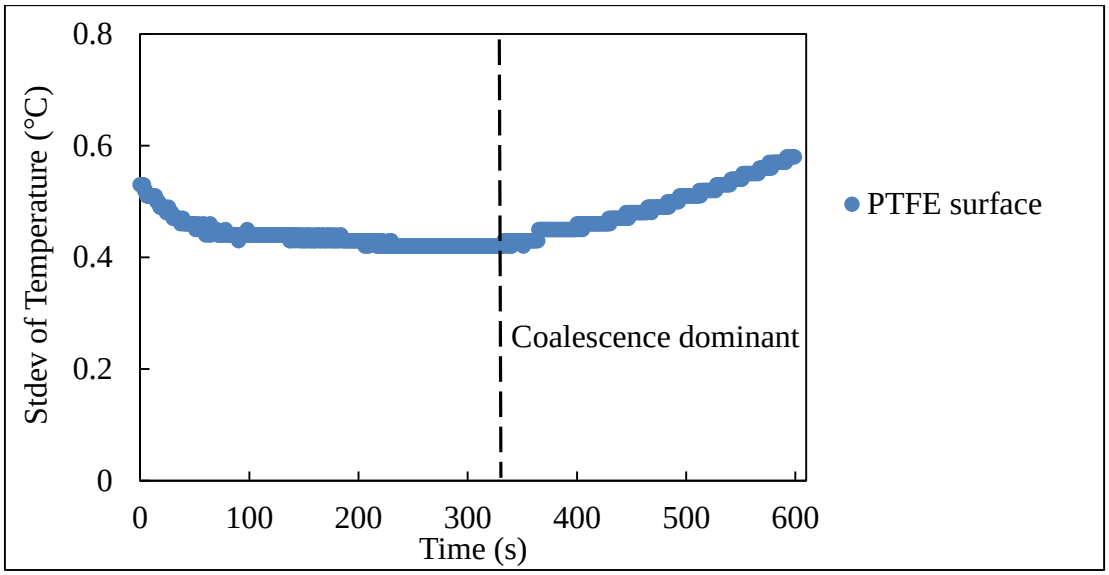

(a)

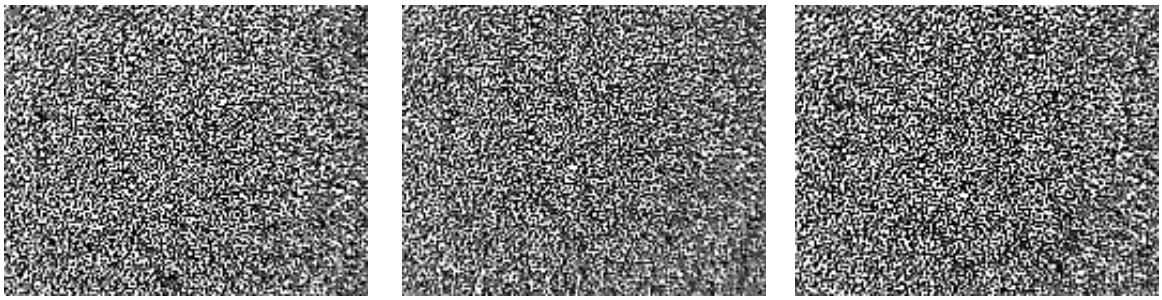

(b) (c) (d)

Figure 47. (a) Standard deviation of surface temperature on PTFE surface during condensation, highly contrasted IR images of condensed water droplets on PTFE surface at (b) 272 sec (c) 332 sec (onset) (d) 392 sec

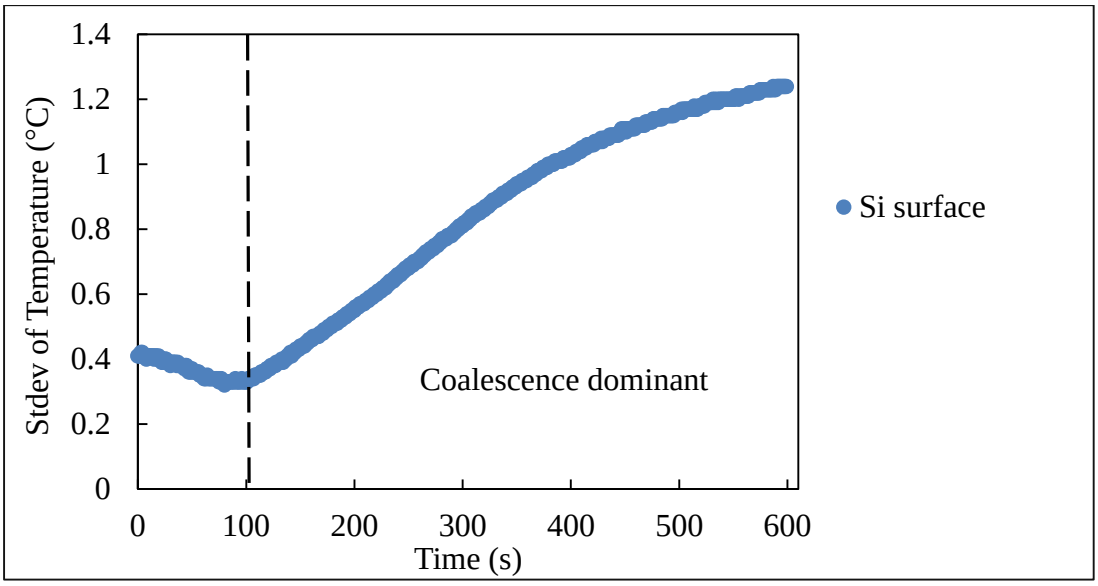

(a)

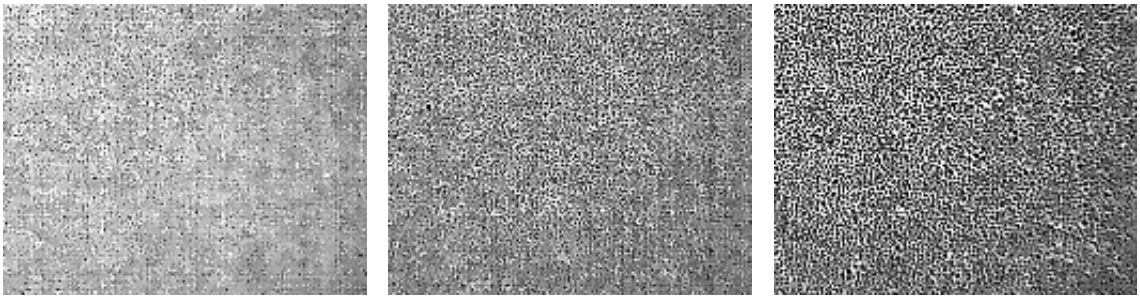

(b) (c) (d)

Figure 48. (a) Standard deviation of surface temperature on Si surface during condensation, highly contrasted IR images of condensed water droplets on Si surface at (b) 40 sec (c) 100 sec (onset) (d) 160 sec

CHAPTER VII

CONCLUSIONS AND RECOMMENDATIONS FOR FUTURE WORK

The primary objective of this study was to determine and characterize the condensation mechanisms responsible for enhanced heat transfer on engineered surfaces. To study the underlying condensation dynamics and enhanced heat transfer, a series of experiments have been conducted using engineered surfaces. The experiments were divided into three classes including wettability measurement, condensation dynamics analysis, and heat transfer measurement. These methodologies provided a proper way to study the heat transfer performance during condensation on engineered surfaces. A high resolution microscopy system was built to observe the condensation process in situ. IR images and temperature data were analyzed accordingly. Based on the results of this study, the effect of surface morphology and droplet growth dynamics on heat transfer during condensation were elucidated.

This study increased our knowledge of surfaces capable of achieving dropwise condensation in a rather controlled manner. Specifically, water harvesting systems, supercomputers, and air conditioners would be benefited by the expected enhanced dropwise condensation processes. Engineered surfaces should also be beneficial in the design and fabrication of heat exchangers commonly employed in heating and air conditioning systems. Enhancement in dropwise condensation should result in an increase in performance in HVAC and even electronic systems.

7.1. Conclusions

An energy-minimization-based model has been developed that is capable of predicting droplet contact angles on hybrid surfaces. In order to evaluate the effect of surface morphology on the wetting properties of hybrid surfaces, a set of hybrid surfaces were designed, fabricated and characterized to understand how surface properties and morphology affect enhanced droplet contact angles and droplet shedding. Results indicated that using hybrid surfaces for condensation purposes leads to a strong pinning effect that takes place between the condensing droplets and the hydrophobic-hydrophillic edge, leading to a significant contact angle hysteresis effect and poor heat transfer behavior.

Two different condensation wetting mechanisms of hybrid surfaces, namely dropwise and dropwise-filmwise, have been identified. A surface energy based model has been formulated that is capable of predicting the transition between droplet wetting states characteristic of dropwise and dropwise-filmwise condensation modes. The model can also be used to design hybrid surfaces with distinct droplet wetting characteristics in order to avoid or induce unfavorable or favorable wetting states during condensation. Experimental results reveal that surface morphology has a strong influence over the final wetting state of condensing droplets which can lead to the self-removal of droplets from the hydrophilic sites, which in turn should facilitate enhanced droplet renucleation and growth at the same patterned sites.

More types of engineered surfaces were fabricated including nanoparticle-based hydrophobic surface, polytetrafluoroethylene (PTFE) surface, and self-assembled

monolayers (SAMs) surface. The effects of surface wettability on dew condensation were investigated. It was found that the static contact angles and sliding angles have a significant influence on growth and coalescence process of droplets during condensation. Also, the condensation process on the nanoparticle-based hydrophobic surface is quite unique since it is characterized by the spontaneous motion of droplets which leads to the lowest surface coverage. Furthermore, experimental results reveal that droplet sliding angles have an important effect on droplet sliding motion.

Several heat transfer experiments were conducted to evaluate the effectiveness of all engineered surfaces during dew condensation. Heat transfer measurements were made by maintaining constant relative humidity of moist-air at constant air velocity. Experimental results reveal that the PTFE surface exhibits superior heat transfer performance since droplets could easily shed and did not grow as much as in other engineered surfaces.

Heat transfer characteristics during dew condensation on engineered surfaces was studied too. Heat transfer coefficient correlations as a function of independent factors such as condensing and air temperature difference and Reynolds number were postulated and fitted using experimental data with a good confidence level. Based on the experimental results, it can be concluded that that the effect of air velocity or Reynolds number on heat transfer performance is much more significant than the effects of condensing and air temperature difference.

Infrared thermography and high resolution photography were used to identify the main condensation mechanisms during the initial phases of condensation. The standard

deviation of surface temperature along with visual observation reveal that temperature distribution can be used to delineate the different condensation stages.

7.2. Recommendations

From the results of the study, the following recommendations for future work can be made:

The results indicate that using microstructured hybrid surfaces during condensation resulted in a significant contact angle hysteresis effect due to the edge effect cause by hydrophilic tips. There is certainly a trade-off between using high surface energy sites and having surfaces that minimize contact angle hysteresis to promote droplet shedding. Nanoparticles should be employed on hybrid surfaces to provide nanoscale roughness and enhance shedding ability. For example, an array of micro scale towers could be fabricated with hydrophilic tops and hydrophobic sides and valleys coated with nanoparticles to promote rapid condensation and droplet shedding.

Experiments also indicate that most engineered surfaces still need efficient droplet shedding properties during condensation. Several studies have investigated droplet deformation and movement induced by vibration. Therefore, the effects of vibration on droplet departure (shedding) during condensation should be studied. Vibrations could be induced using a loudspeaker coordinated by a wave function generator to control the period and amplitude of vibration. Condensation experiments could be conducted using a Peltier.

The self-propelled jumping mechanism offers an alternative method for condensed droplet shedding. However, the impact of lost jumping motion capability or viability

during long-term condensation remains to be studied. The droplet jumping process for a wide variety of superhydrophoic surfaces and condensation conditions should be investigated as well.

In order to get more accurate surface temperature during condensation, a new cooling method should be developed. Specifically, the use of substrate without cooling cell as the primary energy sink should be considered for improved IR thermal imaging from the solid surface side.

Although IR image system has certain limits in terms of spatial resolution at the micro scales, higher resloution infrared lenses should be used in the future to be able to image smaller condensed droplets and surface features at the micron scale. This will allow for precise measurement of temperature history of individual droplets during nucleation and coalescence events.

REFERENCES

[1] E. Schmidt, W. Schurig, and W. Sellschopp, Technische Mechanik und Thermodynamik **1**, 53 (1930).

[2] J. W. Rose, Chemical Engineering Research and Design **76**, 143 (1998).

[3] J. W. Rose, Proceedings of the Institution of Mechanical Engineers, Part A: Journal of Power and Energy **216**, 115 (2002).

[4] K. A. Wier and T. J. McCarthy, Langmuir **22**, 2433 (2006).

[5] R. D. Narhe and D. A. Beysens, Langmuir **23**, 6486 (2007).

[6] C.-H. Chen, Q. Cai, C. Tsai, C.-L. Chen, G. Xiong, Y. Yu, and Z. Ren, Applied Physics Letters **90**, 173108 (2007).

[7] J. B. Boreyko and C.-H. Chen, Physical Review Letters **103**, 184501 (2009).

[8] K. K. Varanasi, M. Hsu, N. Bhate, W. Yang, and T. Deng, Applied Physics Letters **95**, 094101 (2009).

[9] R. D. Narhe, W. González-Viñas, and D. A. Beysens, Applied Surface Science **256**, 4930 (2010).

[10] C. Dietz, K. Rykaczewski, A. G. Fedorov, and Y. Joshi, Applied Physics Letters **97**, 033104 (2010).

[11] X. Chen, J. Wu, R. Ma, M. Hua, N. Koratkar, S. Yao, and Z.Wang, Advanced Functional Materials **21**, 4617 (2011).

[12] R. D. Narhe and D. A. Beysens, Europhys. Lett. **75**, 98 (2006).

[13] C. Dorrer and J. Rühe, Langmuir **23**, 3820 (2007).

[14] N. Miljkovic, R. Enright, and E. N. Wang, ACS Nano **6**, 1776 (2012).

[15] R. D. Narhe and D. A. Beysens, EPL (Europhysics Letters) **75**, 98 (2006).

[16] B. He, N. A. Patankar, and J. Lee, Langmuir **19**, 4999 (2003).

[17] B. Bhushan and Y. Chae Jung, Ultramicroscopy **107**, 1033 (2007).

[18] W. Chen, A. Y. Fadeev, M. C. Hsieh, D. Ö ner, J. Youngblood, and T. J. McCarthy, Langmuir **15**, 3395 (1999).

[19] H. Yabu, M. Takebayashi, M. Tanaka, and M. Shimomura, Langmuir **21**, 3235 (2005).

[20] R. Fürstner, W. Barthlott, C. Neinhuis, and P. Walzel, Langmuir **21**, 956 (2005).

[21] B. Bhushan, Y. C. Jung, and K. Koch, Langmuir **25**, 3240 (2009).

[22] W. Barthlott and C. Neinhuis, Planta **202**, 1 (1997).

[23] B. Bhushan, Y. C. Jung, and K. Koch, Philos Transact A Math Phys Eng Sci **367**, 1631 (2009).

[24] N. Michael and B. Bhushan, Microelectronic Engineering **84**, 382 (2007).

[25] G. S. Watson, B. W. Cribb, and J. A. Watson, ACS Nano **4**, 129 (2010).

[26] X. Gao and L. Jiang, Nature **432**, 36 (2004).

[27] X.-Q. Feng, X. Gao, Z. Wu, L. Jiang, and Q.-S. Zheng, Langmuir **23**, 4892 (2007).

[28] T. Sun, L. Feng, X. Gao, and L. Jiang, Accounts of Chemical Research **38**, 644 (2005).

[29] X. Gao, X. Yan, X. Yao, L. Xu, K. Zhang, J. Zhang, B. Yang, and L. Jiang, Advanced Materials **19**, 2213 (2007).

[30] E. Bormashenko, Y. Bormashenko, T. Stein, G. Whyman, and E. Bormashenko, Journal of Colloid and Interface Science **311**, 212 (2007).

[31] M. H. Rausch, A. P. Fröba, and A. Leipertz, International Journal of Heat and Mass Transfer **51**, 1061 (2008).

[32] M. H. Rausch, A. Leipertz, and A. P. Fröba, International Journal of Heat and Mass Transfer **53**, 423 (2010).

[33] L. Zhong, M. Xuehu, W. Sifang, W. Mingzhe, and L. Xiaonan, Chemical Engineering Journal **156**, 546 (2010).

[34] P. Dimitrakopoulos and J. J. L. Higdon, Journal of Fluid Mechanics **395**, 181 (1999).

[35] L. R. Glicksman and A. W. Hunt Jr, International Journal of Heat and Mass Transfer **15**, 2251 (1972).

[36] S. Kim and K. J. Kim, Journal of Heat Transfer **133**, 081502 (2011).

[37] R. P. Garrod, L. G. Harris, W. C. E. Schofield, J. McGettrick, L. J. Ward, D. O. H. Teare, and J. P. S. Badyal, Langmuir **23**, 689 (2006).

[38] A. R. Parker and C. R. Lawrence, Nature **414**, 33 (2001).

[39] A. B. D. Cassie and S. Baxter, Transactions of the Faraday Society **40**, 546 (1944).

[40] R. N. Wenzel, Industrial & Engineering Chemistry **28**, 988 (1936).

[41] N. A. Patankar, Langmuir **20**, 7097 (2004).

[42] A. Tuteja, W. Choi, G. H. McKinley, R. E. Cohen, and M. F. Rubner, MRS Bulletin **33**, 752 (2008).

[43] H. E. Jeong, M. K. Kwak, C. I. Park, and K. Y. Suh, Journal of Colloid and Interface Science **339**, 202 (2009).

[44] Y. Kwon, N. Patankar, J. Choi, and J. Lee, Langmuir **25**, 6129 (2009).

[45] T. Liu, W. Sun, X. Sun, and H. Ai, Langmuir **26**, 14835 (2010).

[46] M. H. Rausch, A. Leipertz, and A. P. Fröba, Langmuir **26**, 5971 (2010).

[47] Q. Baojin, Experimental Thermal & Fluid Science **35**, 211 (2011).

[48] Q. Zhao and B. M. Burnside, Heat Recovery Systems and CHP **14**, 525 (1994).

[49] J. W. Rose, International Journal of Heat and Mass Transfer **24**, 191 (1981).

[50] A. Bani Kananeh, M. H. Rausch, A. P. Fröba, and A. Leipertz, International Journal of Heat and Mass Transfer **49**, 5018 (2006).

[51] S. Daniel, M. K. Chaudhury, and J. C. Chen, Science **291**, 633 (2001).

[52] K. Rykaczewski, Langmuir **28**, 7720 (2012).

[53] J. Cheng, A. Vandadi, and C.-L. Chen, Applied Physics Letters **101**, 131909 (2012).

[54] R. N. Leach, F. Stevens, S. C. Langford, and J. T. Dickinson, Langmuir **22**, 8864 (2006).

[55] B. S. Sikarwar, S. Khandekar, S. Agrawal, S. Kumar, and K. Muralidhar, Heat Transfer Engineering **33**, 301 (2012).

[56] R. D. Narhe and D. A. Beysens, Physical Review Letters **93**, 076103 (2004).

[57] J. Feng, Z. Qin, and S. Yao, Langmuir **28**, 6067 (2012).

[58] K. Rykaczewski, J. H. J. Scott, S. Rajauria, J. Chinn, A. M. Chinn, and W. Jones, Soft Matter **7**, 8749 (2011).

[59] W. Zhou, G. Henderson, and S. T. Revankar, International Journal of Heat and Mass Transfer **53**, 1146 (2010).

[60] M. Al-Sahali and H. M. Ettouney, Chemical Engineering Journal **143**, 257 (2008).

[61] A. Tiwari, A. Kondjoyan, and J.-P. Fontaine, Appl Biochem Biotechnol **167**, 1132 (2012).

[62] M. H. M. Grooten and C. W. M. van der Geld, International Journal of Thermal Sciences **54**, 220 (2012).

[63] A. P. Colburn and O. A. Hougen, Industrial & Engineering Chemistry **26**, 1178 (1934).

[64] D. W. Tanner, C. J. Potter, D. Pope, and D. West, International Journal of Heat and Mass Transfer **8**, 419 (1965).

[65] W. J. Minkowycz and E. M. Sparrow, International Journal of Heat and Mass Transfer **9**, 1125 (1966).

[66] G. Caruso and D. Vitale Di Maio, International Journal of Heat and Mass Transfer **68**, 401 (2014).

[67] P. D. Lebedev, A. M. Baklastov, and Z. F. Sergazin, International Journal of Heat and Mass Transfer **12**, 833 (1969).

[68] M. A. Yaghoubi, H. Kazeminejad, and A. Farshidiyanfar, Journal of Heat Transfer **115**, 785 (1993).

[69] N. Nagai, M. Takeuchi, O. Kura, and T. Masuda, (ASME, 2005).

[70] D. Che, Y. Da, and Z. Zhuang, Heat and Mass Transfer **41**, 250 (2005).

[71] Y. Liang, D. Che, and Y. Kang, Heat and Mass Transfer **43**, 677 (2007).

[72] B. Nabovati, M. Yaghoubi, and A. Avara, Heat Transfer—Asian Research **41**, 565 (2012).

[73] A. V. Thomas, N. Koratkar, and Y. Peles, International Journal of Heat and Mass Transfer **55**, 7858 (2012).

[74] P. Götze, C. Philipp, and U. Gross, in *Journal of Physics: Conference Series* (IOP Publishing, 2012), p. 012129.

[75] V. P. Caery, 2nd ed. (Taylor and Francis, New York, 2008), p. 417.

[76] J. Drelich, J. L. Wilbur, J. D. Miller, and G. M. Whitesides, Langmuir **12**, 1913 (1996).

[77] M. Morita, T. Koga, H. Otsuka, and A. Takahara, Langmuir **21**, 911 (2005).

[78] A. A. Saha and S. K. Mitra, Journal of Fluids Engineering **131**, 061202 (2009).

[79] M. Nakamura, Thin Solid Films **496**, 131 (2006).

[80] L. R. White, Journal of the Chemical Society, Faraday Transactions 1: Physical Chemistry in Condensed Phases **73**, 390 (1977).

[81] C. W. Yao, T. P. Garvin, J. L. Alvarado, A. M. Jacobi, B. G. Jones, and C. P. Marsh, Applied Physics Letters **101**, 111605 (2012).

[82] Y.-C. Lo, D. Li, Z. Sun, S. Shaik, and X. Cheng, Journal of Vacuum Science & Technology B: Microelectronics and Nanometer Structures **30**, 06FB04 (2012).

[83] F. P. Incropera, A. S. Lavine, and D. P. DeWitt, *Fundamentals of heat and mass transfer* (John Wiley & Sons, 2011).

[84] W. Li and A. Amirfazli, Journal of Colloid and Interface Science **292**, 195 (2005).

[85] H. Y. Erbil and C. E. Cansoy, Langmuir **25**, 14135 (2009).

[86] C. E. Cansoy, H. Y. Erbil, O. Akar, and T. Akin, Colloids and Surfaces A: Physicochemical and Engineering Aspects **386**, 116 (2011).

[87] E. L. Decker, B. Frank, Y. Suo, and S. Garoff, Colloids and Surfaces A: Physicochemical and Engineering Aspects **156**, 177 (1999).

[88] B. Bhushan, M. Nosonovsky, and Y. Chae Jung, Journal of The Royal Society Interface **4**, 643 (2007).

[89] C. W. Extrand, Langmuir **19**, 3793 (2003).

[90] C.-W. Yao, J. L. Alvarado, C. P. Marsh, B. G. Jones, and M. K. Collins, Applied Surface Science **290**, 59 (2014).

[91] M. Sbragaglia, A. M. Peters, C. Pirat, B. M. Borkent, R. G. H. Lammertink, M. Wessling, and D. Lohse, Physical Review Letters **99**, 156001 (2007).

[92] Q. S. Zheng, Y. Yu, and Z. H. Zhao, Langmuir **21**, 12207 (2005).

[93] J. Bico, Colloids & Surfaces A: Phys. Eng. Asp. **206**, 41 (2002).

[94] N. Miljkovic, R. Enright, Y. Nam, K. Lopez, N. Dou, J. Sack, and E. N. Wang, Nano Letters (2012).

[95] R. Norris, Augmentation of Convective Heat and Mass Transfer, 66 (1970).

[96] N. K. Maheshwari, D. Saha, R. K. Sinha, and M. Aritomi, Nuclear Engineering and Design **227**, 219 (2004).

[97] C. Chantana and S. Kumar, Applied Thermal Engineering **54**, 399 (2013).

APPENDIX A

Table A-1 Condensation data for condensation heat transfer performance of engineered surfaces

Surface type	Test number	*h* (W/m^2k)	q" (W/m^2)	T_{air} (℃)	$T_{surface}$ (℃)
Si	1	46.7	555.6	21.8	9.9
	2	46.1	537.6	21	9.4
PTFE	1	48.4	548.2	21.3	10
	2	47.3	552	21.5	9.8
SAMs	1	45.8	525.6	21.1	9.6
	2	45.3	541.2	21.7	9.7
Nanoparticle-based	1	42.5	491.8	21	9.4
	2	46.3	548.6	21.5	9.7
Hybrid surface 1 (HS1)	1	43.7	518.4	21.3	9.5
	2	43.9	503.2	21.2	9.7
Hybrid surface 2 (HS2)	1	42.3	470.6	20.9	9.7
	2	39.9	472.1	21	9.2

Table A-2 Condensation data for condensation heat transfer performance of Si surface, Reynolds number = 312, RH = 80%

h (W/m^2k)	q" (W/m^2)	T_{air} (℃)	$T_{surface}$ (℃)
41	503.6	20.7	8.4
40.2	498.2	20.8	8.4
40.9	449.5	21.2	10.2
42.2	470	21.3	10.2
40	382.8	21.3	11.7
40.9	393	21.3	11.7
38.7	309.4	21.2	13.2
40.9	325	21.2	13.3

Table A-3 Condensation data for condensation heat transfer performance of Si surface, Reynolds number = 469, RH = 80%

h (W/m^2k)	q" (W/m^2)	T_{air} (℃)	$T_{surface}$ (℃)
45.4	576.6	21.5	8.8
46.6	589.5	21.5	8.9
45.7	487.3	20.9	10.3
47.5	506.1	21	10.3
47.1	422.3	20.9	11.9
47.4	426.3	20.8	11.8
45.8	343.6	20.9	13.4
46.2	347.5	20.8	13.3

Table A-4 Condensation data for condensation heat transfer performance of Si surface, Reynolds number = 608, RH = 80%

h (W/m^2k)	q" (W/m^2)	T_{air} (℃)	$T_{surface}$ (℃)
51.3	613.8	20.8	8.9
48.2	585.4	21	8.8
50.4	526.3	21	10.5
49.5	520.5	20.9	10.4
48.7	439	21	12
49.2	441.8	20.9	12
48.3	360.9	21	13.5
48.2	358.9	20.9	13.5

Table A-5 Condensation data for condensation heat transfer performance of Si surface, Reynolds number = 754, RH = 80%

h (W/m^2k)	q" (W/m^2)	T_{air} (℃)	$T_{surface}$ (℃)
53.7	634.7	20.9	9.1
53.2	640.4	20.2	8.2
55.5	563.9	20.9	10.7
53.5	548.6	20.9	10.6
54.1	454.1	20.4	12
52.2	438.4	20.3	11.9
52.8	363.7	20.4	13.5
50.6	349.4	20.3	13.4

Table A-6 Condensation data for condensation heat transfer performance of Si surface, Reynolds number = 315, RH = 32%

h (W/m^2k)	q" (W/m^2)	T_{air} (℃)	$T_{surface}$ (℃)
7	92.8	20.6	7.3
7.1	93.9	20.6	7.3
8.1	92.4	20.6	9.2
8.3	94.8	20.6	9.1
8.8	86.1	20.7	10.9
8.5	83	20.7	10.9
10.4	83.3	20.8	12.7
10.3	82.1	20.8	12.8

Table A-7 Condensation data for condensation heat transfer performance of Si surface, Reynolds number = 472, RH = 32%

h (W/m^2k)	q" (W/m^2)	T_{air} (℃)	$T_{surface}$ (℃)
12.1	153.8	20.4	7.7
12.1	153.5	20.4	7.7
13.3	145.7	20.5	9.5
13.1	143.2	20.1	9.5
13.5	125.1	20.5	11.2
13.4	125.1	20.5	11.1
13.9	107.1	20.5	12.8
13.9	107.1	20.5	12.8

Table A-8 Condensation data for condensation heat transfer performance of Si surface, Reynolds number = 629, RH = 32%

h (W/m^2k)	q" (W/m^2)	T_{air} (℃)	$T_{surface}$ (℃)
16.3	198.9	20.2	8
16.2	196.3	20.2	8.1
17.2	179.7	20.2	9.8
17.3	181.4	20.3	9.8
17.9	156.6	20.3	11.4
19.5	160.2	20.3	12.1
17.8	129.3	20.3	13.1
18.1	131.4	20.3	13.1

Table A-9 Condensation data for condensation heat transfer performance of Si surface, Reynolds number = 787, RH = 32%

h (W/m^2k)	q" (W/m^2)	T_{air} (℃)	$T_{surface}$ (℃)
20.9	239.4	19.7	8.3
20.3	233.4	19.7	8.2
20.5	204.8	19.9	10
20.4	203.8	19.9	9.9
21.1	178.3	20	11.5
20.7	174.3	20	11.5
21.9	150.8	20	13.1
21.7	148.9	20	13.2

Table A-10 Condensation data for condensation heat transfer performance of PTFE surface, Reynolds number = 298, RH = 80%

h (W/m^2k)	q" (W/m^2)	T_{air} (℃)	$T_{surface}$ (℃)
43.7	528.4	20.7	8.6
43.9	525.1	20.5	8.5
44.3	471.5	20.9	10.2
44	484.1	21.3	10.3
43.7	399.3	21	11.8
43.2	399.1	20.8	11.8
44	341.8	21.2	13.4
44.2	336.1	21	13.4

Table A-11 Condensation data for condensation heat transfer performance of PTFE surface, Reynolds number = 438, RH = 80%

h (W/m^2k)	q" (W/m^2)	T_{air} (℃)	$T_{surface}$ (℃)
51.1	612.4	21.1	9.1
46.4	588.6	20.5	7.8
51.5	535	21	10.6
51.8	516.8	20.4	10.5
50.6	460.9	21.4	12.3
50.2	431.4	20.5	11.9
51.6	370.6	20.8	13.6
52	357.5	20.4	13.5

Table A-12 Condensation data for condensation heat transfer performance of PTFE surface, Reynolds number = 569, RH = 80%

h (W/m^2k)	q" (W/m^2)	T_{air} (℃)	$T_{surface}$ (℃)
55.2	625.9	20.4	9.1
54.4	512.3	20.3	9
57	551.2	20.4	10.7
55.1	538.2	20.4	10.7
53.7	452.1	20.7	12.3
55.6	472.5	20.8	12.3
56.8	384.1	20.5	13.7
54.4	368.8	20.3	13.6

Table A-13 Condensation data for condensation heat transfer performance of PTFE surface, Reynolds number = 733, RH = 80%

h (W/m^2k)	q" (W/m^2)	T_{air} (℃)	$T_{surface}$ (℃)
58.5	640.4	20.2	9.3
57.8	647.5	20.6	9.4
60.1	566.3	20.4	11
58.9	565.3	20.7	11
59.5	485.4	20.5	12.4
59	465	20.2	12.3
59.8	398.8	20.5	13.9
60.1	394.5	20.5	13.9

Table A-14 Condensation data for condensation heat transfer performance of PTFE surface, Reynolds number = 315, RH = 32%

h (W/m^2k)	q" (W/m^2)	T_{air} (℃)	$T_{surface}$ (℃)
6.6	90.9	21	7.3
6.8	92.9	21	7.2
7.6	89.7	21	9.2
7.6	90.1	21	9.1
7.2	72.7	21	10.8
7.7	77.7	21	10.9
8.8	73.7	21	12.6
8.6	72.1	21	12.6

Table A-15 Condensation data for condensation heat transfer performance of PTFE surface, Reynolds number = 472, RH = 32%

h (W/m^2k)	q" (W/m^2)	T_{air} (℃)	$T_{surface}$ (℃)
11.4	150.4	20.9	7.7
11.5	151.2	20.9	7.7
13	148.5	20.9	9.5
13.1	149.2	20.9	9.5
13	126	20.9	11.2
13	126.3	20.9	11.2
13.6	108.6	20.9	12.9
12.9	102.9	20.9	12.9

Table A-16 Condensation data for condensation heat transfer performance of PTFE surface, Reynolds number = 629, RH = 32%

h (W/m^2k)	q" (W/m^2)	T_{air} (℃)	$T_{surface}$ (℃)
14.2	181.3	20.8	8.1
14.2	181.5	20.8	8.1
16.1	177	20.8	9.8
16.1	177.7	20.8	9.8
16.1	151	20.8	11.5
16.1	151.4	20.8	11.4
16.9	130	20.8	13.1
17	131.2	20.8	13.1

Table A-17 Condensation data for condensation heat transfer performance of PTFE surface, Reynolds number = 785, RH = 32%

h (W/m^2k)	q" (W/m^2)	T_{air} (℃)	$T_{surface}$ (℃)
17.3	215.6	20.7	8.3
17.2	214.3	20.7	8.2
18.1	194.5	20.7	10
18.3	195.6	20.8	10
18.5	168.6	20.7	11.6
18.7	171.1	20.7	11.6
19.5	145.4	20.7	13.3
19.2	143	20.7	13.3

Table A-18 Condensation data for condensation heat transfer performance of nanoparticle-based surface, Reynolds number = 306, RH = 80%

h (W/m^2k)	q" (W/m^2)	T_{air} (℃)	$T_{surface}$ (℃)
40.4	572.5	21.3	7.2
40.8	582	21.5	7.2
40.4	501.4	21.3	8.9
42.6	539.3	21.7	9
40.3	435	21.4	10.6
41.5	452	21.5	10.7
38.8	339.1	21	12.3
38.9	359.7	21.5	12.3

Table A-19 Condensation data for condensation heat transfer performance of nanoparticle-based surface, Reynolds number = 462, RH = 80%

h (W/m^2k)	q" (W/m^2)	T_{air} (℃)	$T_{surface}$ (℃)
44.8	626.4	21.5	7.5
47.2	626.5	20.8	7.5
46	556.3	21.2	9.1
43.4	520.8	20.9	8.9
45.6	474.5	21.2	10.8
44.1	458	21.1	10.7
43.1	380	21.2	12.4
43.4	382.8	21.2	12.4

Table A-20 Condensation data for condensation heat transfer performance of nanoparticle-based surface, Reynolds number = 604, RH = 80%

h (W/m^2k)	q" (W/m^2)	T_{air} (℃)	$T_{surface}$ (℃)
50.2	667.6	20.8	7.5
51.5	680.1	20.8	7.6
50.7	593.6	21	9.3
48.4	559.9	20.7	9.2
47.6	482.6	21.1	10.9
50.1	494.5	20.7	10.9
49	408.2	20.9	12.5
50.3	423.6	21	12.6

Table A-21 Condensation data for condensation heat transfer performance of nanoparticle-based surface, Reynolds number = 746, RH = 80%

h (W/m^2k)	q" (W/m^2)	T_{air} (℃)	$T_{surface}$ (℃)
55.7	744.9	21.3	7.9
54.2	715.8	21.1	7.9
54.6	645.3	21.3	9.5
53.5	636.7	21.3	9.4
54	554.4	21.4	11.1
52.4	518.2	20.8	10.9
51.5	416.1	20.6	12.6
50.7	425.5	20.9	12.5

Table A-22 Condensation data for condensation heat transfer performance of nanoparticle-based surface, Reynolds number = 315, RH = 32%

h (W/m^2k)	q" (W/m^2)	T_{air} (℃)	$T_{surface}$ (℃)
8.1	107.7	20.7	7.4
8.4	111	20.7	7.4
8.4	96.9	20.7	9.2
8.6	98.3	20.7	9.2
9.4	92.1	20.7	11
9.4	91.7	20.7	11
9.3	74.5	20.7	12.8
9.7	77.6	20.7	12.7

Table A-23 Condensation data for condensation heat transfer performance of nanoparticle-based surface, Reynolds number = 474, RH = 32%

h (W/m^2k)	q" (W/m^2)	T_{air} (℃)	$T_{surface}$ (℃)
13.1	170.8	20.8	7.8
12.8	163.2	20.4	7.7
14.3	159	20.8	9.7
14.4	161	20.8	9.6
14.4	137.4	20.8	11.3
14.4	167.5	20.8	11.3
15.9	123.3	20.8	13
16	124.3	20.8	13

Table A-24 Condensation data for condensation heat transfer performance of nanoparticle-based surface, Reynolds number = 629, RH = 32%

h (W/m^2k)	q" (W/m^2)	T_{air} (℃)	$T_{surface}$ (℃)
18	226.7	20.9	8.2
18.1	227.7	20.9	8.3
17.9	195.9	20.9	9.9
17.5	193	20.9	9.9
18.6	171.6	20.9	11.6
18.8	174.4	20.9	11.6
20.1	152.2	20.9	13.3
20.5	154.4	20.9	13.3

Table A-25 Condensation data for condensation heat transfer performance of nanoparticle-based surface, Reynolds number = 787, RH = 32%

h (W/m^2k)	q" (W/m^2)	T_{air} (℃)	$T_{surface}$ (℃)
21.6	268	20.9	8.5
21.7	268	20.9	8.5
22.5	236.9	20.9	10.3
22.5	238.3	20.9	10.3
22.5	201.6	20.9	11.9
22.5	203.2	20.9	11.9
24.5	180.9	20.9	13.5
24.7	182.9	20.9	13.5

APPENDIX B

Uncertainties in condensation heat transfer coefficients were found using the following equation:

$$W_h = \sqrt{(\frac{\partial h}{\partial q''} W_{q''})^2 + (\frac{\partial h}{\partial T} W_{T_{surface}})^2 + (\frac{\partial h}{\partial T} W_{T_{air}})^2}$$

Uncertainties for condensation heat transfer performance of engineered surfaces in Fig. 32 were found as following:

W_h (Si)	1.10 ($W/m^2 K$)
W_h (SAMs)	1.12 ($W/m^2 K$)
W_h (PTFE)	1.28 ($W/m^2 K$)
W_h (Nano)	1.08 ($W/m^2 K$)
W_h (HF1)	0.96 ($W/m^2 K$)
W_h (HF2)	1.19 ($W/m^2 K$)

APPENDIX C

Anemometer and RH sensor

Brand: TSI

Model: AVM440

Anemometer Specifications and Operating Performance Ranges

Velocity Range: 0 to 30 m/s (0 to 6,000 ft/min)

Accuracy: ±3% of reading or ±0.015 m/s (±3 ft/min)

Resolution: 0.01 m/s (1 ft/min)

RH Sensor Specifications and Operating Performance Ranges

Relative Humidity Range: 0 to 95% RH

Accuracy: ±3% RH

Resolution: 0.1% RH

Humidity Controller

Brand: Omega

Model: CNiTH-i8dv22-5

Accuracy: ±2% RH

Hysteresis: ±1% RH

Response Time: 8 seconds

Thin Film Heat Flux Sensor

Brand: Omega

Model: HFS-4

Sensitivity: 2 μV to 1 W/m^2

Resp. Time: 0.6 (sec)

Thermal Capacitance: 0.113 W per m^2 k

Thermal Resistance: 0.00176 K- m^2 per W

Nominal Thickness: 0.18 mm